Fermilab FERMILAB-THESIS-1999-12

Abstract

Title of Dissertation: Extraction of the Width of the W Boson from a Measurement of the Ratio of the W and Z Cross Sections.

Gervasio Gómez, Doctor of Philosophy, 1999

Dissertation directed by: Assistant Professor Sarah C. Eno
Department of Physics

This dissertation reports on measurements of inclusive cross sections times branching fractions into electrons for W and Z bosons produced in $p\overline{p}$ collisions at $\sqrt{s}$ = 1.8 TeV. From an integrated luminosity of 84.5 pb^{-1} recorded in 1994–1995 by the DØ detector at the Fermilab Tevatron, the cross sections are measured to be $\sigma(p\overline{p} \to W + X) \cdot B(W \to e\nu)$= 2310 ± 10 (stat) ± 50 (syst) ± 100 (lum) pb and $\sigma(p\overline{p} \to Z + X) \cdot B(Z \to ee)$= 221 ± 3 (stat) ± 4 (syst) ± 10 (lum) pb. The cross section ratio $\mathcal{R}$ is determined to be $\sigma(p\overline{p} \to W+X)\cdot B(W \to e\nu)/\sigma(p\overline{p} \to Z + X) \cdot B(Z \to ee)$ = 10.43 ± 0.15 (stat) ± 0.20 (syst) ± 0.10 (NLO), and $\mathcal{R}$ is used to determine $B(W \to e\nu)$ = 0.1044 ± 0.0015 (stat) ± 0.0020 (syst) ± 0.0017 (theory) ± 0.0010 (NLO), and , $_W$ = 2.169 ± 0.031 (stat) ± 0.042 (syst) ± 0.041 (theory) ± 0.022 (NLO) GeV. The latter is used to set a 95% confidence level upper limit on the partial decay width of the W boson into non-standard model final states, , $^{inv}_{W}$, of 0.213 GeV.

Extraction of the Width of the W Boson from a Measurement of the Ratio of the W and Z Cross Sections

by

Gervasio Gómez

Dissertation submitted to the Faculty of the Graduate School of the
University of Maryland at College Park in partial fulfillment
of the requirements for the degree of
Doctor of Philosophy
1999

Advisory Committee:

Assistant Professor Sarah C. Eno, Chairman/Advisor
Professor Albohassan Jawahery
Associate Professor Xiangdong Ji
Assistant Professor Douglas A. Roberts
Professor Lawrence C. Washington.

© Copyright by

Gervasio Gómez

1999

Dedication

To my parents, my brother, and my sister:

Raúl Eduardo Gómez

María Esmeralda Gramuglio

Emiliano Gómez

María Leticia Gómez

Acknowledgements

As with all physics analysis carried out in the DØ Collaboration, there are many people who contributed to this work directly and indirectly. This includes all the people who participated in the design, construction, and running of the detector, from the electronics to the software. To mention them all would take way too much space, and I have therefore included the current DØ author list in Appendix C. Instead, I will single out those who participated directly in the present analysis. I would like to thank the members of my Editorial Board (EB066_01) and the members of the electroweak physics group who read several versions of the analysis at different stages and gave invaluable comments and advice: EB chair Bob McCarthy, Harry Melanson, Mark Strovink, John Ellison, and Hugh Montgomery. Darien Woods deserves a special mention for sharing his expertise, providing some calculations, and being always right. I

thank Eric Flattum and Ian Adam for writing the fast Monte Carlo used in this analysis. Dylan Casey helped in organizing the data into Ntuples and provided calculations of transverse momentum and rapidity distributions used in the Monte Carlo model. I also thank Dave Toback for reading several drafts of the final analysis and providing very helpful comments and suggestions.

This analysis started with the hard work of two people: Jamal Tarazi and Joey Thompson. They left all the machinery necessary for me to finish it. They were my first mentors at Fermilab, and I will never forget their quality as physicists and as friends. I am particularly thankful to my advisor, Sarah Eno. She has guided my work from the very beginning with infinite patience, has always participated closely in all aspects of my research, and has kept in touch almost daily during four years. She has helped directly in this analysis since the start, and her physics insight and programming skills have been invaluable. Besides her impact on my academic development, she has always been kind and nice to work with. I feel very lucky to have worked with her.

From the theory world, I thank Ulrich Baur for helpful discussions and calculations concerning electroweak radiative corrections and diffractive weak boson production. I also thank John Collins, James Stirling and Willy van Neerven for discussions about diffractive W and Z production. I also thank Tim Tait, who was always there to answer any physics question I had, and who reviewed my theory chapter.

I thank the University of Maryland group at Fermilab: Bill Cobau, Adam Lyon, Peter Tamburello, Joey Thompson, Suishi Kunori, Nick Hadley, Drew Baden, Dave Toback and Sarah Eno. I also thank the members of my dissertation committee: Sarah Eno, Albohassan Jawahery, Xiangdong Ji, Douglas Roberts, and Lawrence Washington.

In addition to the people who participated in my work, there are those who participated in my social and academic life and whose friendship and support helped a great deal. There are many friends at Fermilab who made my life there enjoyable. Rather than mentioning all of them, which would take too long, I would like to thank them all, and give special mention to: Tim, Simona, Miguel, Clarisa, Daniel, Cecilia, Sebastian, Veronica, Freedy, Jamal, Joey, Aurelio, Irene, Dana, Ivan, Germano, Lara, David and Rosa. My experience at Fermilab would certainly not have been the same without you guys. Thanks for being there. From the University of Maryland, special thanks for their friendship go to Alejandro, Luis, and Úrsula. Visits to Maryland are never dull with you guys around, especially at lunch time.

I also thank my family, and in particular my brother Emiliano, my sister María Leticia, my mother María Esmeralda, and my father Raúl Eduardo. Your love and support has been the most important gift of my life. Nothing I say here can possibly express how deeply I feel about you, so I dedicate to you this work, which I consider my best academic achievement.

Finally, I thank Rocío Vilar for her love and support. Even though she works for the experiment across the ring, we have always helped each other. She led me by example to work harder, and more importantly, she makes my life a happy one. Meeting her is the best thing that has ever happened to me, and I am very proud and very lucky to share the rest of my life with her.

Table of Contents

List of Tables **x**

List of Figures **xii**

1 Introduction and Theory **1**
1.1 Introduction . . . 1
1.2 Motivation . . . 8
1.3 The Standard Model . . . 9
1.4 W and Z Boson Production . . . 17
1.4.1 W and Z Boson Cross Section . . . 17
1.4.2 W and Z Boson Mass . . . 19
1.4.3 W and Z Boson Rapidity and Transverse Momentum . . . 20
1.4.4 W and Z Boson Polarization . . . 22
1.5 W and Z Boson Decay . . . 24
1.6 The W Width . . . 24
1.6.1 Direct Measurement of , $_W$ . . . 25
1.6.2 Indirect Measurement of , $_W$ . . . 27
1.7 Previous Measurements . . . 27
1.8 Units and Conventions . . . 28
1.9 Outline . . . 29

2 The Tevatron and the DØ Detector **30**
2.1 The Tevatron Collider . . . 30
2.2 The DØ Detector . . . 34
2.3 DØ Coordinate System . . . 35
2.4 Central Tracking System . . . 37
2.5 Calorimeter . . . 40
2.6 The Muon Spectrometer . . . 44
2.7 Trigger and Data Acquisition . . . 45

2.7.1 Level-Ø . . . 46
2.7.2 Level-1 . . . 47
2.7.3 Level-2 . . . 48

3 Data Event Selection **49**
3.1 Event Reconstruction . . . 50
3.2 Electron Identification . . . 50
3.2.1 Electromagnetic Energy Fraction . . . 51
3.2.2 Shower Shape Analysis . . . 53
3.2.3 Shower Isolation . . . 56
3.2.4 Track Matching . . . 57
3.3 Neutrino Identification . . . 59
3.4 Electron Vertex Finding . . . 61
3.5 Offline Electron Selection . . . 65
3.6 $W \to e\nu$ Selection . . . 67
3.6.1 $W \to e\nu$ Trigger Requirements . . . 67
3.6.2 $W \to e\nu$ Offline Selection . . . 69
3.7 $Z \to ee$ Event Selection . . . 70
3.7.1 $Z \to ee$ Trigger Requirements . . . 71
3.7.2 $Z \to ee$ Offline Selection . . . 72

4 Acceptance **75**
4.1 The CMS Monte Carlo . . . 75
4.1.1 Event Generation . . . 76
4.1.2 Detector Response . . . 81
4.2 Geometric and Kinematic Acceptance . . . 96
4.3 NLO Electroweak Radiative Corrections . . . 99

5 Efficiencies **100**
5.1 Electron Identification Efficiencies . . . 100
5.1.1 Background Subtraction . . . 102
5.1.2 Single Electron Efficiencies . . . 104
5.1.3 Efficiency Correlations . . . 105
5.2 Trigger Efficiencies . . . 114
5.2.1 Level-Ø Efficiency . . . 114
5.2.2 Level-2 $\not{E}_T$ Trigger Efficiency . . . 115
5.3 Overall $W \to e\nu$ Selection Efficiency . . . 115
5.4 Overall $Z \to ee$ Selection Efficiency . . . 116
5.5 Efficiency Ratio . . . 117
5.6 Diffractive Production of Weak Bosons . . . 118

6 Backgrounds **120**
6.1 Backgrounds in the $W \to e\nu$ Sample 121
6.1.1 Backgrounds from multi-jet, b-quark, and direct photon sources 121
6.1.2 $W \to \tau\nu$ Background 127
6.1.3 $Z \to ee$ and $Z \to \tau\tau$ Backgrounds 129
6.2 Backgrounds in the $Z \to ee$ Sample 130
6.2.1 Backgrounds from multi-jet, b-quark, and direct photon sources 131
6.2.2 Drell-Yan and Z/γ^* Interference 131
6.2.3 $Z \to \tau\tau$ 133

7 Luminosity **135**

8 Results and Conclusions **139**
8.1 Cross Section Measurements 139
8.2 Indirect Measurements 142
8.3 Consistency Checks 148
8.3.1 Cross Sections from the Individual Cryostats 148
8.3.2 Dependence on Instantaneous Luminosity 150

9 Conclusions and Future Prospects **155**

A Rapidity and Pseudorapidity **158**

B Cancelation of Tracking Efficiency Correlations in $\mathcal{R}$ **161**

C DØ Author List **163**

List of Tables

1.1 Elementary particles of the standard model 3

1.2 Gauge Bosons of the standard model 5

3.1 Summary of the $W \to e\nu$ signal event sample and topological breakdown. 70

3.2 Summary of the $Z \to ee$ signal event sample and topological breakdown. 73

4.1 Acceptances, their ratio, and their systematic uncertainties for W and Z boson events. 97

5.1 Summary of the background subtraction methods used in estimating electron selection efficiencies. 104

5.2 Number of (background subtracted) central (CC) and forward (EC) electrons contained in the $Z \to ee$ signal window for various offline cuts and background subtraction methods. 106

5.3 Central electron relative identification efficiencies. 106

5.4 Forward electron relative identification efficiencies. 106

6.1 QCD background fractions for different parent/child samples in the CC $W \to e\nu$ sample. 126

6.2 QCD background fractions for different parent/child samples in the EC $W \to e\nu$ sample. 127

7.1 Values used in the $\sigma_{L\emptyset}$ calculation; SD, DD and ND refer to single diffractive, double diffractive, and non diffractive, respectively. . 137

8.1 Values used in the $W \to e\nu$ cross section measurement. 141

8.2 Values used in the $Z \to ee$ cross section measurement. 142

8.3 Values used in the Ratio Measurement. 145

8.4 Comparison of the current run 1b (1994–1995) measurement to the run 1a (1992–1993) measurement. 146

8.5 Results. 148

List of Figures

1.1 Lowest order diagrams for W^+ and Z boson production. 17

1.2 Initial state gluon radiation and Compton scattering in W^+ production. 20

1.3 Initial state gluon radiation and Compton scattering in Z production. 21

1.4 Leading order diagrams for $W \to e\nu$ and $Z \to ee$ decays. 24

2.1 Fermilab Tevatron Collider complex. 31

2.2 Isometric view of the DØ detector. 36

2.3 Side view of the DØ central tracking detectors. 38

2.4 Layout of the FDC. 39

2.5 Isometric view of the DØ calorimeter system. 43

2.6 Side view of the calorimeter towers 44

3.1 EM fraction distribution for probe electron candidates from $Z \to ee$ data and electron candidates from multijet triggered data. 52

3.2 H-matrix $\chi^2_{\rm hm}$ distribution for test beam electrons, test beam pions, and electrons from $W \to e\nu$ events. 55

3.3 H-matrix $\chi^2_{\rm hm}$ distribution for probe electron candidates from $Z \to ee$ data and electron candidates from multijet triggered data. . . 56
3.4 Isolation distribution for probe electron candidates from $Z \to ee$ data and electron candidates from multijet triggered data. 57
3.5 Definition of track match significance in terms of the cluster centroid in EM3 and the projection of the track to the radius of EM3. 59
3.6 Track match significance distribution for electron candidates from $Z \to ee$ data and electron candidates from multijet triggered data. 60
3.7 Cluster vertex determination. 62
3.8 Distribution of $(z_1 - z_2)$ in $Z \to ee$ events (cm). 63
3.9 (a) Frequency at which the standard vertex is mismeasured as a function of instantaneous luminosity. (b) Invariant mass distribution for $Z \to ee$ events using the two vertexing algorithms. 65
3.10 The transverse mass distribution of the $W \to e\nu$ candidate event sample (GeV). 71
3.11 The invariant mass distribution of the $Z \to ee$ candidate event sample (GeV). 74

4.1 Invariant mass distributions for W and Z bosons from PYTHIA. . 78
4.2 Vector boson transverse momentum for data and Monte Carlo . . 80
4.3 Electron θ for W and Z from data and from Monte Carlo. 81
4.4 Event vertex z position for $Z \to ee$ data and Monte Carlo 82
4.5 Invariant mass distribution for CC-CC $Z \to ee$ events fit to a Breit-Wigner convoluted with a gaussian. 85
4.6 Determination of the CC energy resolution constant term 86
4.7 Definition of the η–ξ coordinate system in a $Z \to ee$ event. 88

4.8 The η-imbalance, $(p_T^{\rm rec})_\eta + (p_T^{\rm ee})_\eta$, versus $(p_T^{ee})_\eta$ from the $Z \to ee$ sample. 89
4.9 Determination of the hadronic scale α_H. 90
4.10 η-balance distribution for data and Monte Carlo. 92
4.11 Determination of the minimum bias scale factor. 93
4.12 The electron η_D distribution for $Z \to ee$ candidates and for Monte Carlo. 94
4.13 The electron E_T distribution for $Z \to ee$ candidates and for Monte Carlo. 95

5.1 Illustration of the background subtraction methods used in the determination of electron identification efficiencies. 103
5.2 Illustration of sample sets used to measure the electron identification efficiencies. 108

6.1 The $\not{E}_T$ distribution for a particular choice of parent and child inclusive electron samples, and for Monte Carlo $W \to e\nu$ and $W \to \tau\nu \to e\nu\overline{\nu}\nu$ events. 124
6.2 Electron E_T distribution for $W \to \tau\nu \to e\nu\nu\nu$ events. 128
6.3 Fit of the $Z \to ee$ invariant mass distribution to a linear combination of Monte Carlo signal and direct-photon background. . . . 132

7.1 Distribution in luminosity for $W \to e\nu$ or $Z \to ee$ candidates. The mean and RMS values of the distributions are consistent with each other. 138

8.1 Comparison between measured and predicted cross sections, $\sigma(p\overline{p} \rightarrow W + X) \cdot B(W \rightarrow e\nu)$ and $\sigma(p\overline{p} \rightarrow Z + X) \cdot B(Z \rightarrow ee)$. 143

8.2 Run 1a and 1b results for the W and Z cross sections times electronic branching fractions. 144

8.3 Comparison of , $_W$ measurements. 147

8.4 The $W \rightarrow e\nu$ cross section versus instantaneous luminosity. . . . 152

8.5 The $Z \rightarrow ee$ cross section versus instantaneous luminosity. 153

8.6 The ratio $\mathcal{R}$ versus instantaneous luminosity. 154

Extraction of the Width of the W Boson from a Measurement of the Ratio of the W and Z Cross Sections

Gervasio Gómez

September 2, 1999

This comment page is not part of the dissertation.

Typeset by LaTeX using the `dissertation` class by Pablo A. Straub, University of Maryland.

Chapter 1

Introduction and Theory

1.1 Introduction

This dissertation presents an indirect measurement of the width of the W boson. Indirect because what is really measured is the ratio of the W and Z production cross sections times electronic branching fraction. This suggests several questions: what is a W and a Z boson? What is the width of a particle? What is a cross section? How is the W width related to the ratio of W and Z cross sections times electronic branching fractions?

One of the main goals of particle physics is to understand what matter is made of, and which are the forces in nature through which these matter particles interact. Our understanding of the composition of matter has evolved greatly with time. We learned that molecules are made up of atoms, and atoms are made up of sub-atomic constituents called protons, neutrons and electrons. We know today that the neutron and the proton are in turn made up of smaller constituents called *quarks*. A theory called the *standard model* exists today which describes most sub-atomic phenomena. Although it is not believed to be

a complete theory for several reasons (gravity is not incorporated, forces are not unified, masses are arbitrarily put in by hand, it doesn't explain the number of particle families observed, among others) it nevertheless has been very successful in making highly accurate predictions of nearly all phenomena observed to date, and it is clear that any new, more complete theory will have to be similar to the standard model in the ranges of energy probed so far in laboratories. In quantum field theories like the standard model, particles are characterized by a set of intrinsic properties called *quantum numbers*, such as electrical charge, spin, color, etc. An interesting prediction of quantum field theory is the existence of "antimatter": for any particle, there is a corresponding antiparticle which has the same mass but has all other quantum numbers reversed. For example, the antiproton is the antiparticle of the proton. Today it is believed that all matter in the universe is made up of *quarks* and *leptons*. These are indivisible particles which are arranged into three similar groups, or generations, of increasing mass but which have similar properties. Each family has a quark of electrical charge $+2/3$, one quark of charge $-1/3$, one lepton of charge -1, and one neutral lepton called *neutrino*, which in the standard model is massless. The first generation consists of the up quark, the down quark, the electron and the electron neutrino, and it accounts for essentially all ordinary matter. Table 1.1 lists the elementary particles of the three generations.

In quantum theory, energy is carried by discrete quanta, which are the particles which transmit the forces. The standard model predicts the properties of these additional particles which mediate interactions between the matter particles. They are called *gauge bosons* or *vector bosons*. A boson is a particle whose intrinsic angular momentum, or spin, is an integer, while fermions are particles

Table 1.1: Elementary particles of the standard model

	Generation 1	Generation 2	Generation 3
Quarks	up (u)	charm (c)	top (t)
	down (d)	strange (s)	bottom (b)
Leptons	electron (e)	muon (μ)	tau (τ)
	electron neutrino (ν_e)	muon neutrino (ν_μ)	tau neutrino (ν_τ)

with half-integral spin. All quarks and leptons are fermions. The term "gauge boson" arises from the fact that the standard model is a gauge theory, in which interactions are described by an invariance under "gauge" transformations, as will be explained later. These gauge bosons are the carriers of the known forces of nature. The most familiar force, the force of gravity, is responsible for the attraction between any two massive objects. It is the weakest and least understood of all forces, and the standard model makes no attempt to incorporate it. The electromagnetic force is also very familiar. Like the force of gravity, it has infinite range, and it is responsible for the repulsion of like charges, the attraction of opposite charges, the chemical properties of atoms and molecules, and all magnetic and electric phenomena. The gauge boson that carries the electromagnetic force is called the photon; it has no charge and no mass. The human eye is a very good photon detector: visible light consists of photons of a certain range of energy. The remaining two forces of nature are less familiar, owing to the fact that they act only at very short distances, of the order of the size of a nucleus or smaller. In order to overcome the large electrostatic repulsion

which arises from confining positive charges inside such a tiny nucleus, protons must be bound together by a powerful force. This force is called the *strong*, or *color* force, and it is carried by eight massless gauge bosons called *gluons*. The word color here refers to an intrinsic property of all quarks and gluons, and not to any actual color. The theory which describes the strong interactions between quarks and gluons is called *Quantum Chromodynamics*, or QCD. Finally, there is the *weak* force, which is responsible for the observed beta decay of the neutron: $n \to p + e + \bar{\nu}_e$. It is mediated by three massive gauge bosons called W^+, W^- and Z. It is called "weak" because, at low energies (of the order of the muon or electron rest mass energy), its strength is approximately four orders of magnitude smaller than the strength of the electromagnetic force, which in turn has a strength approximately two orders of magnitude smaller than the strong force. It should be noted, however, that the strengths of these forces depend both on the coupling strengths of the gauge bosons to the fermions, and on the masses of the gauge bosons. At low energies, the high mass of the weak bosons reduces the effective strength of the weak force, but at high energies where on-shell weak bosons can be exchanged, the weak force is actually stronger than the electromagnetic force. Table 1.2 lists the gauge bosons of the standard model and the interactions which they mediate, as well as the range of the force and the mass of the bosons. So the answer to the first question is: the W and Z bosons are massive particles which mediate the weak interactions between quarks and leptons.

Classical theories are deterministic, in the sense that the evolution of a system can be determined exactly if one knows the initial conditions and the forces acting on it. Quantum theory, on the other hand, is probabilistic: it does not

Table 1.2: Gauge Bosons of the standard model

Gauge boson	Interaction	Range	Mass
γ (photon)	electromagnetism	∞	massless
Z	neutral weak currents	≈ 0.1 fm	91.19 GeV
W^+, W^-	charged weak currents	≈ 0.1 fm	80.4 GeV
g (gluon)	strong	≈ 1 fm	massless

predict a single, determined outcome, but rather the probability for different outcomes given an initial set of conditions. The W production cross sections times electronic branching fraction is basically the probability for the process

$$p\bar{p} \rightarrow W + \text{anything} \rightarrow \text{e}\nu + \text{anything}$$

to occur. This cross section depends on the energy of the $p\overline{p}$ collision. The higher the energy, the easier it becomes to produce a heavy particle. It also depends on the internal composition of the proton and antiproton, in particular on the fractional momentum carried by each of their constituent particles, which can be valence quarks, virtual "sea" quarks and gluons. In this analysis, protons and antiprotons collide head on at nearly the speed of light, with a center-of-mass energy of 1.8 TeV. How this is achieved will be explained in Chapter 2. The electronic branching fraction is simply the probability that a W, when it decays, decays to an electron and a neutrino. This branching fraction depends on the decay channels which are allowed for each particle. Similarly, the Z cross section

times electronic branching fraction is basically the probability for the process

$$p\bar{p} \rightarrow Z + \text{anything} \rightarrow \text{ee} + \text{anything}$$

to occur. Measuring these cross sections is nothing more than a sophisticated counting experiment. Using a given data set, we count the number of $W \rightarrow e\nu$ or $Z \rightarrow ee$ events, and divide by the total number of $p\overline{p}$ interactions. We start by making a $W \rightarrow e\nu$ or $Z \rightarrow ee$ event selection, and count the number of events N which pass the selection criteria. This number is not the number of $W \rightarrow e\nu$ or $Z \rightarrow ee$ events for two reasons: there might be "background" events in the final samples which do not come from W or Z decays, and these must therefore be estimated and subtracted; also, a fraction of the real $W \rightarrow e\nu$ and $Z \rightarrow ee$ events produced escape detection because they do not pass the geometric, kinematic, or electron identification requirements imposed in the event selection. The number of observed events must be corrected to account for this. The cross section times branching fraction is calculated as

$$\sigma \cdot Br = \frac{N - B}{\epsilon A \mathcal{L}} \tag{1.1}$$

where N is the number of events which pass the selection criteria, B is the total number of background events, ϵ is the electron identification efficiency, A is the geometric and kinematic acceptance, and $\mathcal{L}$ is the integrated luminosity of the data sample used, a measure of the amount of data and of the number of $p\overline{p}$ interactions in the data sample. This dissertation contains a separate chapter to describe each of the components of Equation 1.1.

In order to make a precise measurement of the ratio of these two cross sections, we need to understand the nature of W and Z boson production and decay. The standard model gives a strikingly accurate description of these phenomena,

and a brief review of the theory is given later in this chapter. We can roughly estimate what the ratio $\mathcal{R}$ should be without making any fancy calculations. There are two W bosons (W^+ and W^-) and only one Z boson, so from this fact alone $\mathcal{R}$ gets a "contribution" of 2. In addition, the W and Z branching fractions to electrons have been measured to be $B(W \to e\nu) \approx 11\%$ and $B(Z \to ee) \approx 3\%$. The Z has a smaller branching fraction to electrons than the W because it can decay into neutrino-antineutrino pairs, which make up for $\approx 20\%$ of the total decay width. Therefore $\mathcal{R}$ gets an additional "contribution" of 11/3. In addition, the W boson is slightly lighter than the Z boson, and therefore it is easier to produce a W than a Z boson at a given center-of-mass energy. This would give $\mathcal{R}$ and additional phase space "contribution" which is hard to estimate, but which should be of order 1, since the ratio of the W and Z masses is of that order. So one would expect $\mathcal{R}$ to be slightly larger than $2 \times (11/3) \approx 7$.

Quantum theories have yet another striking property (called the uncertainty principle): there is an intrinsic, irreducible uncertainty in the simultaneous measurement of certain pairs of physical observables. Energy and time is one such pair. Quantum theory predicts that the product of the uncertainties in life time and energy of a particle is always greater than some small number $\hbar$, called the reduced Plank constant, which has a value of 1.05×10^{-34} J·s, or 6.58×10^{-25} GeV·s. As a consequence, any unstable particle which lives for only a finite amount of time has an intrinsic uncertainty in its mass or rest energy (recall $E = mc^2$). The width of a particle can be thought of as its intrinsic spread in mass, or in its rest energy. If we had a large sample of W bosons decaying at rest and we reconstruct the mass of the W from the decay products, we would not have a delta function distribution. Rather, we would have a distribution which

peaks around 80 GeV and which has a width of about 2 GeV. The position of the peak can be determined very accurately if one has a large number of events, but the distribution would always have an intrinsic width , $_W$. An alternative way to think of the width of a particle is as the inverse of the lifetime. From the uncertainty principle, a particle of width , can live for a time $\Delta t \leq \hbar/,$. Therefore short lived particles have a large width, while more stable particles have a narrow width. For a W boson of , $\approx$ 2 GeV, the lifetime is about $\hbar/, = 6.58 \times 10^{-25}$ GeV $\cdot$ s/2 GeV $= 3.29 \times 10^{-25}$ s. Therefore the W lives for only a very short time; even if it could travel close to the speed of light, it would only travel about 0.1 fm before decaying. Since this particle carries the weak force, one sees why this force has such a short range. The relationship between the W width and the ratio of W and Z boson cross sections times electronic branching fraction will be explained later in this chapter, but first, why is it interesting to measure the W width?

1.2 Motivation

The prediction of the existence of the W and Z bosons by the standard model was confirmed in 1983 [1] when W and Z events were observed by the UA1 and UA2 experiments at CERN (a European high energy physics laboratory). Since their discovery, the comparison of the properties of W and Z bosons to predictions of the standard model has been a subject of intense study [2, 3, 4, 5, 6, 7]. One such property is the W width. Within the standard model, the W boson decays into quark or lepton electroweak doublets. The partial decay width of the W

boson into massless fermions $f\bar{f}'$ can be written as

$$, (W \to f\bar{f}') = |V_{f\bar{f}'}|^2 N_C (G_F/\sqrt{2})(M_W^3/6\pi) \tag{1.2}$$

where $V_{f\bar{f}'}$ is the Kobayashi-Maskawa matrix element for decays into quarks, and 1 for decays into leptons. The term N_C accounts for color and is $3(1 + \alpha_s(M_W)/\pi + \ldots)$ for decays into quarks and 1 for leptonic decays. Within the standard model, the total width of the W is the sum of the partial widths over three generations of lepton doublets and two generations of quark doublets (decays of the W to the third-generation quark doublet is forbidden by energy conservation because the top quark is considerably heavier than the W). If additional non-standard model particles exist, which are lighter than and couple to the W, then the width would have an additional contribution. An example of this are supersymmetric models where the W can decay to the lightest super-partner of the charged gauge bosons and the lightest super-partner of the neutral gauge bosons, with a width that depends on the mass of the super-particles [8]. Thus, the W width is of interest as a test of the standard model, and also as a probe for new physics.

1.3 The Standard Model

Electroweak interactions in the standard model are mediated by the γ, W, and Z bosons, which are quanta of local gauge fields. We will describe the theory for the case of the first-generation leptons (e and ν_e), since generalizing to the quarks and the other generations is straight forward. A more complete description of the standard model at an introductory level is given in Ref. [9]. The starting point is the construction of a Lagrangian density for a free (no interactions),

massless fermion field $\psi(x)$:

$$\mathcal{L} = \bar{\psi} i \gamma^\mu \partial_\mu \psi \tag{1.3}$$

where μ is the space-time index which runs from 0 to 3, γ^μ are the 4×4 Dirac matrices, $\bar{\psi} \equiv \psi^\dagger \gamma^0$ and $\partial_\mu = \partial / \partial x^\mu = (\partial_0; \nabla)$.

Experimentally, no right handed neutrinos are observed[1] (i.e., neutrinos always have their spin pointing in the direction opposite to their momentum), so one writes the electron and neutrino fields as a left handed doublet and a right handed singlet:

$$R_e = (e_R) \tag{1.4}$$

$$L_e = \begin{pmatrix} \nu_e \\ e_L \end{pmatrix} \tag{1.5}$$

where the left and right handed components of a field ψ are defined by

$$\psi_L = P_L \psi = \frac{1 - \gamma^5}{2} \psi \tag{1.6}$$

$$\psi_R = P_R \psi = \frac{1 + \gamma^5}{2} \psi \tag{1.7}$$

The free lagrangian for massless leptons is then

$$\mathcal{L} = \bar{L}_e i \gamma^\mu \partial_\mu L_e + \bar{R}_e i \gamma^\mu \partial_\mu R_e \tag{1.8}$$

Two quantum numbers (internal degrees of freedom) are postulated: weak isospin T and hypercharge Y. The doublet has $T = 1/2$ and the singlet $T = 0$. The upper component of the doublet has third component of weak isospin $T_3 =$

[1] Recently, the SuperKamiokande experiment in Japan has indirectly observed possible neutrino oscillations which would imply a non-zero neutrino mass and therefore the existence of right handed neutrinos. If this is confirmed, the standard model will have to be modified.

1/2 and the lower component has $T_3 = -1/2$. The hypercharge is given by the relation

$$Q = T_3 + Y/2 \tag{1.9}$$

where Q is the electrical charge of the particle. The way particles behave under electroweak $SU(2)$ transformations is familiar because spin also transforms under a (different) $SU(2)$ group. From quantum mechanics we know that particles with spin zero are singlets, particles with spin 1/2 ($J = 1/2$) form doublets with $J_3 = +1/2, -1/2$, particles with spin 1 for triplets with $J_3 = -1, 0, 1$. All known quarks and leptons are experimentally observed to be either electroweak singlets or doublets. The theory is required to be invariant under $SU(2)$ phase transformations in the space describing the internal isospin degrees of freedom. Since $T = 0$ for the singlet, the $SU(2)$ group acts non-trivially only on the doublet. The lagrangian must then be invariant under $SU(2)$ transformations of the form

$$L_e \to e^{i\vec{\alpha}\cdot\vec{\tau}/2} L_e \tag{1.10}$$

where $\vec{\alpha}$ are three parameters which specify the rotation and $\vec{\tau}$ are the Pauli matrices, the generators of the isospin $SU(2)$ group:

$$\tau^1 = \begin{pmatrix} 0 & 1 \\ 1 & 0 \end{pmatrix} \qquad \tau^2 = \begin{pmatrix} 0 & -i \\ i & 0 \end{pmatrix} \qquad \tau^3 = \begin{pmatrix} 1 & 0 \\ 0 & -1 \end{pmatrix} \tag{1.11}$$

The fact that these matrices do not commute implies that the transformation is non-Abelian, which means that the order of transformations matters.

In a similar way, the theory is required to be invariant under $U(1)_Y$ transformations of the form

$$\psi \to e^{i\alpha Y}\psi \Rightarrow \begin{cases} L_e \to e^{-i\alpha} L_e \\ R_e \to e^{-2i\alpha} R_e \end{cases} \tag{1.12}$$

where α specifies the transformation and hypercharge Y is the generator of the $U(1)_Y$ group. Electroweak singlets have $Y = Y_R = -2$ while doublets have $Y = Y_L = -1$.

Asking the gauge symmetries to hold locally corresponds to allowing the coefficients α and $\vec{\alpha}$ to be functions of space-time. In order for the lagrangian to remain invariant under local $U(1)_Y$ transformations, one must to introduce a gauge field B_μ which transform as a four-vector, and to replace the derivatives by gauge-covariant derivatives. Invariance under local $SU(2)$ transformations requires the introduction of three vector fields W^a_μ, $a = 1, 2, 3$. The covariant derivative is given by

$$D_\mu = \partial_\mu - ig_1 \frac{Y}{2} B_\mu - ig_2 \frac{\tau^a}{2} W^a_\mu \tag{1.13}$$

which has the property that $D_\mu \psi$ transforms in the same way as ψ. One then defines the field strength tensors

$$F_{\mu\nu} \equiv \partial_\mu B_\nu - \partial_\nu B_\mu \tag{1.14}$$

$$F^a_{\mu\nu} \equiv \partial_\mu W^a_\nu - \partial_\nu W^a_\mu + g_2 \varepsilon^{abc} W^b_\mu W^c_\nu \tag{1.15}$$

where $\varepsilon^{abc} = +1(-1)$ if abc are a cyclic (anticyclic) permutation of 1 2 3 and $\varepsilon^{abc} = 0$ otherwise. The electroweak lagrangian becomes

$$\mathcal{L} = \bar{L}_e i\gamma^\mu D_\mu L_e + \bar{R}_e i\gamma^\mu D_\mu R_e + \frac{1}{4} F_{\mu\nu} F^{\mu\nu} + \frac{1}{4} \vec{F}_{\mu\nu} \vec{F}^{\mu\nu} \tag{1.16}$$

which is invariant under the local $U(1)_Y$ and $SU(2)$ transformations

$$\left.\begin{aligned} L_e &\to e^{-i\alpha(x)} L_e \\ R_e &\to e^{-2i\alpha(x)} R_e \\ B_\mu &\to B_\mu + \tfrac{2}{g_1} \partial_\mu \alpha(x) \end{aligned}\right\} \tag{1.17}$$

$$\left.\begin{array}{l} L_e \to e^{i\vec{\alpha}(x)\cdot\vec{\tau}/2} L_e \\ W^a_\mu \to W^a_\mu + \frac{1}{g_2}\partial_\mu \alpha^a(x) + \varepsilon^{abc}\alpha^b(x) W^c_\mu \end{array}\right\} \tag{1.18}$$

This lagrangian describes massless leptons interacting with four massless vector gauge fields. Generalizing to the first generation fermions corresponds to adding the first generation quarks, which are arranged in right handed singlets and left handed doublets:

$$Q_L = \begin{pmatrix} u_L \\ d_L \end{pmatrix} \qquad u_R \qquad d_R \tag{1.19}$$

If one defines

$$\begin{aligned} W^+ &= (-W^1 + iW^2)/\sqrt{2} \\ W^- &= (-W^1 - iW^2)/\sqrt{2} \\ W^0 &= W^3 \end{aligned} \tag{1.20}$$

and

$$A_\mu = \frac{g_2 B_\mu - g_1 Y_L W^0_\mu}{\sqrt{g_2^2 + g_1^2 Y_L^2}} \tag{1.21}$$

$$Z_\mu = \frac{g_1 Y_L B_\mu + g_2 W^0_\mu}{\sqrt{g_2^2 + g_1^2 Y_L^2}} \tag{1.22}$$

$$e = \frac{g_1 g_2}{\sqrt{g_1^2 + g_2^2}} \tag{1.23}$$

$$\sin\theta_w = s_w = \frac{g_1}{g_1^2 + g_2^2} \tag{1.24}$$

$$\cos\theta_w = c_w = \frac{g_2}{g_1^2 + g_2^2} \tag{1.25}$$

it is possible to show, after a lot of straight-forward algebra, that the $U(1)_Y$ and $SU(2)_T$ parts of the lagrangian (i.e., dropping the field strength terms in Eq. 1.16 and the ∂_μ term in Eq. 1.13) become:

$$
\begin{aligned}
\mathcal{L}_{SU(2)\times SU(1)} &= \sum_{f=\nu_e,e,u,d} eQ_f(\bar{f}\gamma^\mu f)A_\mu \\
&+ \frac{g_2}{c_w}\sum_{f=\nu_e,e,u,d}[\bar{f}_L\gamma^\mu f_L(T_f^3 - Q_f s_w^2) + \bar{f}_R\gamma^\mu f_R(-Q_f s_w^2)]Z_\mu \\
&+ \frac{g_2}{\sqrt{2}}[(\bar{u}_L\gamma^\mu d_L + \bar{\nu}_{eL}\gamma^\mu e_L)W_\mu^+ + \text{h.c.}] \qquad (1.26)
\end{aligned}
$$

where Q_f and T_f^3 are the electromagnetic charge and third component of isospin, respectively, for each fermion f, and "h.c" denotes the hermitian conjugate. From Equations 1.20 the h.c. of W^+ is W^-. The fields A_μ, Z_μ, W_μ^+ and W_μ^- are then identified with the γ, Z, W^+ and W^- fields, respectively. Notice how all fermions which have electric charge interact with the electromagnetic field A_μ, regardless of their isospin, with a strength proportional to the charge. The neutrino, having $Q_\nu = 0$, interacts only with the Z and $W^\pm$ fields. Notice also that only left handed fermions interact with the $W^\pm$ fields. This is due to the fact that right handed fermions are $SU(2)$ singlets with $T = 0$.

So far we have dealt with massless particles. In the standard model, the fermions and gauge bosons acquire mass through the *Higgs* mechanism. We introduce a doublet of complex scalar Higgs fields with $T = 1/2$ and $Y = 1$

$$
\phi = \begin{pmatrix} \phi^+ \\ \phi^0 \end{pmatrix} = \begin{pmatrix} \frac{\phi_1 + i\phi_2}{\sqrt{2}} \\ \frac{\phi_3 + i\phi_4}{\sqrt{2}} \end{pmatrix} \qquad (1.27)
$$

and additional terms in the lagrangian which arise from self interactions of the scalar field:

$$
\mathcal{L}_H = (D_\mu\phi)^\dagger(D_\mu\phi) + \mu^2\phi^\dagger\phi - \lambda(\phi^\dagger\phi)^2 \qquad (1.28)
$$

The potential $\mu^2\phi^\dagger\phi - \lambda(\phi^\dagger\phi)^2$ has a minimum at

$$
|\phi^\dagger\phi| = \frac{\mu^2}{2\lambda} \equiv \frac{v}{\sqrt{2}} \qquad (1.29)
$$

Quantization must therefore start from a ground state, called the *vacuum*, which has a non-zero expectation value. This phenomenon is called spontaneous symmetry breaking: the lagrangian exhibits a symmetry, but the behavior of the system is determined by fluctuations of the field around a ground state which does not have the full symmetry of the lagrangian, and the observable physical system will have a broken symmetry, meaning that the full symmetry of the lagrangian will not be manifest. One usually makes the particular choice of vacuum, ϕ_0,

$$\phi_0 = \frac{1}{\sqrt{2}} \begin{pmatrix} 0 \\ v \end{pmatrix} \tag{1.30}$$

which corresponds to setting $\phi_3 = v$ and $\phi_1 = \phi_2 = \phi_4 = 0$. The coupling of the Higgs field with the gauge bosons is then given by the covariant derivative term in Equation 1.28:

$$\phi^\dagger \left(ig_1 \frac{Y}{2} B_\mu + ig_2 \frac{\vec{\tau}}{2} \vec{W}_\mu \right)^\dagger \left(ig_1 \frac{Y}{2} B^\mu + ig_2 \frac{\vec{\tau}}{2} \vec{W}^\mu \right) \phi \tag{1.31}$$

Putting $Y = 1$, writing the Pauli matrices explicitly, putting $\phi = \phi_0$ and using the definitions for $W_\mu^\pm$, A_μ and Z_μ gives, after some simple algebra, the following terms in the lagrangian:

$$\frac{g_2^2 v^2}{4} W_\mu^+ W^{-\mu} + \frac{g_2^2 v^2}{8 c_w^2} Z_\mu Z^\mu \tag{1.32}$$

Since the expected mass term for a charged boson is $m^2 W^+ W^-$, we see that the W has acquired a mass $M_W = vg/2$. For the neutral vector fields the expected mass terms in the lagrangian are[2] $(M_Z^2 Z_\mu Z^\mu)/2$ and $(M_\gamma^2 A_\mu A^\mu)/2$. Since there

[2]The relative factor of 1/2 in the mass terms between a charged vector field and a neutral one has to do with the fact that charged fields are complex, and therefore two real fields are needed to describe them. See Equations 1.20

are no $A_\mu A^\mu$ terms, we see that the photon remains massless, while $M_Z = vg/2c_w$. The standard model therefore predicts $M_W/M_Z = c_w$, which has been verified experimentally.

The fermions also acquire mass by interacting with the Higgs field. One adds to the lagrangian terms of the form

$$-g_e(\bar{L}\phi e_R + \bar{e}_R\phi^\dagger L) \tag{1.33}$$

This term corresponds to the first generation leptons, but all fermions have similar terms. The couplings g_f are arbitrary, and the fermion masses are given by

$$m_f = \frac{g_f v}{\sqrt{2}} \tag{1.34}$$

The quarks are organized into generations on the basis of mass. Terms such as Equation 1.33 are not required, but rather allowed by gauge invariance. Gauge invariance also allows similar terms which connect, for example, a left handed up quark with a right handed strange quark. In other words, gauge invariance allows terms connecting left and right handed fermions of different families, so that the resulting lagrangian is not diagonal in flavor space. For the quarks, this means the physical or mass eigenstates do not coincide with the weak interaction eigenstates. This is manifested through a mixing between the generations. By convention this mixing is assigned entirely to the $T = -1/2$ quarks:

$$\begin{pmatrix} d' \\ s' \\ b' \end{pmatrix} = \begin{pmatrix} V_{ud} & V_{cd} & V_{td} \\ V_{us} & V_{cs} & V_{ts} \\ V_{ub} & V_{cb} & V_{tb} \end{pmatrix} \begin{pmatrix} d \\ s \\ b \end{pmatrix} \tag{1.35}$$

where the matrix $V_{qq'}$ is a unitary matrix called the CKM matrix after Cabibbo, Kobayashi and Maskawa. The leptons do not mix because there are no right handed neutrinos in the standard model.

1.4 W and Z Boson Production

In $p\overline{p}$ collisions at $\sqrt{s} = 1.8$ TeV, W and Z bosons are produced predominantly through quark-antiquark annihilation. Lowest order diagrams for W^+ and Z boson production are shown in Fig. 1.1. The processes $d\bar{d} \to Z$ and $\bar{u}d \to W^-$ are similar to the ones shown. Though these diagrams are inadequate to

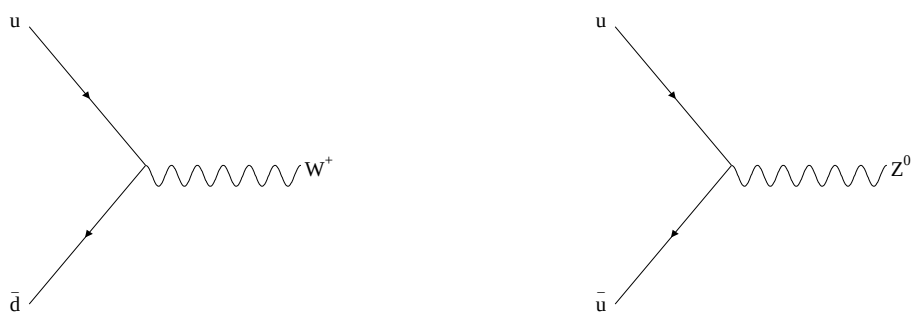

Figure 1.1: Lowest order diagrams for W^+ and Z boson production.

describe inclusive gauge boson production in detail, they are useful for deriving a qualitative picture of the physics and some approximate results. The following sections describe several aspects of W and Z boson production.

1.4.1 W and Z Boson Cross Section

From the electroweak lagrangian it is possible to calculate the matrix elements $\mathcal{M}$ which give the transition probabilities per unit time from an initial state to a final state. The amplitude for the process $u\bar{d} \to W^+$ is given by

$$\mathcal{M} = -iV_{ud}\frac{g_2}{\sqrt{2}}\epsilon_\mu \bar{d}\gamma^\mu P_L u \ , \tag{1.36}$$

where ϵ_μ is the polarization wave function of the W, and all other terms are defined in Section 1.3. The amplitude for the process $q\bar{q} \to Z$ is given by

$$\mathcal{M} = -i\frac{g_2\epsilon_\mu}{c_w}[\bar{q}_L\gamma^\mu q_L(T_f^3 - Q_f s_w^2) + \bar{q}_R\gamma^\mu q_R(T_f^3 - Q_f s_w^2)] \ . \tag{1.37}$$

Calculating the production cross sections from these amplitudes involves averaging $|\mathcal{M}|^2$ over boson polarizations, summing over fermion spins, averaging over quark color, and integrating over phase space. These calculations are outside the scope of this dissertation, and the interested reader should consult Reference [10]. The *partonic* cross sections are

$$\hat{\sigma}(q\bar{q}' \to W^+) = 2\pi|V_{qq'}|^2\frac{G_F}{\sqrt{2}}M_W^2\delta(\hat{s} - M_W^2) \tag{1.38}$$

$$\hat{\sigma}(q\bar{q} \to Z) = 8\pi\frac{G_F}{\sqrt{2}}(g_V^2 + g_A^2)M_Z^2\delta(\hat{s} - M_Z^2) \tag{1.39}$$

where $G_F = g_2^2\sqrt{2}/8M_W^2$ is the Fermi constant, $\sqrt{\hat{s}}$ is the energy of the collision in the center-of-mass frame, $g_V = T_f^3/2 - Q_f s_w^2$ and $g_A = -T_f^3/2$. The total cross sections for the process $p\overline{p} \to V$ (V stands for either the W or the Z vector boson) is then given by the convolution of the partonic cross sections with the quark densities in the proton and antiproton:

$$\sigma(p\bar{p} \to V) = \frac{K}{3}\int_0^1 dx_a \int_0^1 dx_b \sum_{i,j} f_i(x_a, Q^2)\bar{f}_j(x_b, Q^2)\hat{\sigma}(ij) \tag{1.40}$$

where the indices i and j run over the contributing quark flavors, x_a (x_b) is the fraction of the proton (antiproton) momentum carried by q_i ($\bar{q}_j$), $Q^2 = \hat{s} = M_V^2$ is the energy scale of the collision, $f_i(x_a, Q^2)$ and $\bar{f}_j(x_b, Q^2)$ are the *parton distribution functions*, or pdf's, which give the probability that any given quark carries a fraction x of the proton or antiproton momentum, and the K-factor includes higher order QCD corrections.

1.4.2 W and Z Boson Mass

A large part of this analysis involves the modeling of W and Z boson production and decay using a fast Monte Carlo in order to calculate the detector's geometric and kinematic acceptance. The mass distribution is a crucial part of this model. As discussed in Section 1.3, the W and Z bosons acquire a finite mass through the Higgs mechanism. These masses have been measured experimentally, and the current world averages are

$$M_W = 80.375 \pm 0.065 \text{ GeV} \tag{1.41}$$

$$M_Z = 91.187 \pm 0.007 \text{ GeV} \tag{1.42}$$

The W and Z bosons are both spin 1 Breit-Wigner resonances which, at lowest order, are produced from two spin 1/2 quarks. The distribution of the boson mass is therefore proportional to a relativistic, s-dependent Breit-Wigner resonance:

$$\frac{d\hat{\sigma}(q\bar{q}' \to V)}{dm} \propto \frac{m^2, {}^2/M^2}{(m^2 - M^2)^2 + m^4, {}^2/M^2} \ , \tag{1.43}$$

where M and , are the vector boson mass and width, and $s = m^2$ is the usual Mandelstam variable. The observed mass spectrum for $p\overline{p}$ interactions is obtained in the usual way:

$$\frac{d\sigma(q\bar{q}' \to V)}{dm} = \frac{K}{3} \sum_{i,j} \int dx_1 dx_2 f_i(x_1, Q^2) \bar{f}_j(x_2, Q^2) \frac{d\hat{\sigma}(ij)}{dm} \ , \tag{1.44}$$

where i and j range over the contributing flavors, f_i is the pdf for parton i in the proton and f_j is the pdf for parton j in the antiproton, and $d\hat{\sigma}(ij)/dm$ is the cross section for the process $ij \to V$, which has the form of Equation 1.43.

1.4.3 W and Z Boson Rapidity and Transverse Momentum

To lowest order in QCD, W and Z boson production in $p\overline{p}$ collisions occurs through quark antiquark annihilation, as shown in Figure 1.1. Since the initial state quarks have negligible momenta transverse to the beam direction, momentum conservation dictates that the vector boson is produced with no transverse momentum. However, higher order processes such as initial state gluon radiation or Compton scattering, shown in Figures 1.2 and 1.3, allow final states in which hadrons may recoil against the boson. In this case the boson can be produced with a significant transverse momentum p_T.

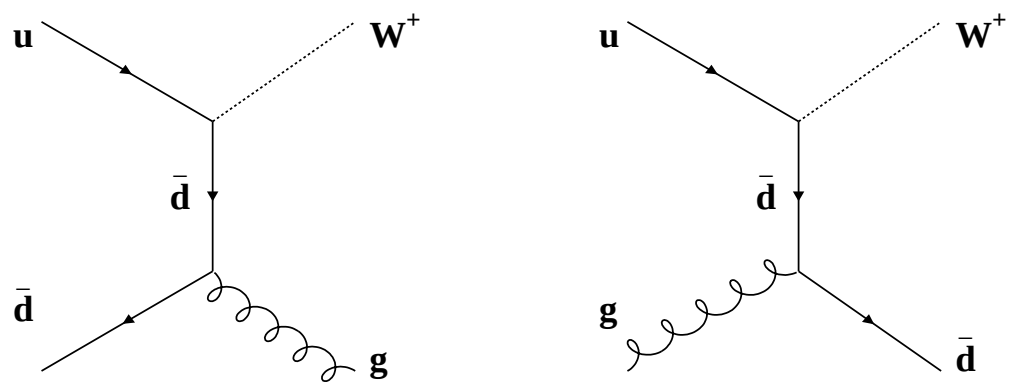

Figure 1.2: Initial state gluon radiation and Compton scattering in W^+ production.

The leptons that decay from a high p_T boson tend to be boosted in the direction of the boson momentum. A theoretical model of the boson p_T distribution is therefore essential to calculate the acceptance, the fraction of $W \to e\nu$ and $Z \to ee$ events which passes the geometric and kinematic cuts imposed in the $W \to e\nu$ and $Z \to ee$ event selection. If one attempts to calculate the p_T spec-

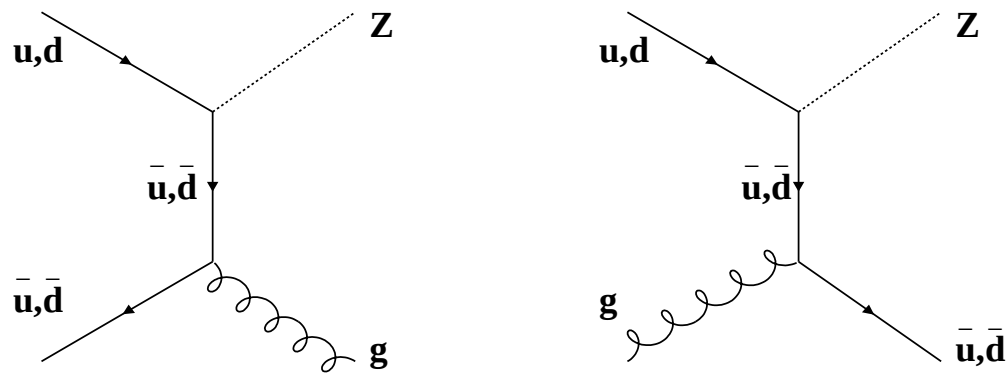

Figure 1.3: Initial state gluon radiation and Compton scattering in Z production.

trum as a perturbative QCD series, the results are approximately correct at high p_T ($p_T \approx M_V$), but the calculation diverges at low p_T. The calculational difficulty at low p_T is due to terms of the form $\alpha_s^n(\ln Q^2/p_T^2)^m$ in the perturbation series, where α_s is the strong coupling constant (which couples the gluon fields to the color-charged quarks) and Q^2 is of the order of M_V^2. Therefore, in the high-p_T regime ($p_T > 50$ GeV) we use a second order perturbative calculation by Arnold and Reno [11], while for the low-p_T regime ($p_T < 50$ GeV), the *resummed* calculation of Ladinsky and Yuan [12] is used. *Resummation* [13] is the theoretical framework which involves rearranging the divergent logarithms that appear in the perturbation series, and summing them into an exponential factor. The resummed double differential cross section for vector boson production is written as:

$$\frac{d^2\sigma}{dp_T^2 dy} \propto \int \frac{d^2b}{(2\pi)^2} e^{i\vec{b}\cdot\vec{p_T}} W(b_\star) e^{-S_{NP}(b)} \ , \tag{1.45}$$

where b, the impact parameter in the transverse plane, is the conjugate variable to p_T: small values of b correspond to large p_T and vice versa, $b_\star$ is a function of

b which handles the divergence at high-b values by incorporating a cutoff b_{max}:

$$b_\star = \frac{b}{\sqrt{1 + b^2/b_{max}^2}} \ , \tag{1.46}$$

and $W(b_\star)$ is a complicated but well defined function calculated in perturbation theory [11], while the function $S_{NP}(b)$ incorporates the non-perturbative effects at high-b values obtained from the resummation. Ladinsky and Yuan use the following parameterization for S_{NP}:

$$S_{NP} = g_1 b^2 + g_2 b^2 \ln\left(\frac{Q}{2Q_\circ}\right) + g_1 g_3 b \ln(100 x_A x_B) \ , \tag{1.47}$$

with $Q_\circ$ an arbitrary momentum scale, Q the mass of the vector boson, and x_A, x_B the momentum fractions of the incoming quarks. The parameters g_1, g_2, and g_3 are determined by Ladinsky and Yuan. They fit their hypothesis to the available Drell-Yan and Z production data [12] and obtain the values:

$$g_1 = 0.11^{+0.04}_{-0.03}\,\mathrm{GeV}^2 \qquad g_2 = 0.58^{+0.1}_{-0.2}\,\mathrm{GeV}^2 \qquad g_3 = -1.5^{+0.1}_{-0.1}\,\mathrm{GeV}^{-1} \ , \tag{1.48}$$

where $Q_\circ = 1.6$ GeV, and $b_{max} = 0.5$ GeV^{-1} are chosen. A study of the relative contributions of each of the three terms [14, chap. 3], shows that g_2 is the dominant parameter at DØ, and that the nominal values computed by Ladinsky and Yuan agree very well with the DØ data. Notice that Equation 1.45 is well behaved over the entire p_T range. At high p_T, $W(b^*)$ is finite, $b \to 0$, and $S_{NP} \to 0 \Rightarrow e^{S_{NP}} \to 1$, while at low p_T, $W(b^*)$ diverges but $b \to \infty$ so that $S_{NP} \to \infty$ and the exponential term cancels the divergence.

1.4.4 W and Z Boson Polarization

From the amplitude for the leading order process $u\bar{d} \to W^+$ given in Equation 1.36, and from the fact that $P_L P_R = 0$, we see that only the left handed

component of the u field and the right handed component of the $\bar{d}$ field contribute to W^+ production. Similar arguments hold for W^- production. The z axis is defined by the proton direction. If the u comes from the proton, then the $\bar{d}$ must come from the antiproton, and in order to conserve angular momentum the W^+ must be produced with spin -1, i.e., the W^+ spin is along the $-z$ direction. If the u comes from the antiproton and the $\bar{d}$ from the proton, the situation is reversed and the W^+ is produced with spin $+1$, along the $+z$ direction. We denote the probability of finding a valence quark of type q in X by V_X^q and the probability of finding a sea quark of type q in X by S_X^q. The probability of the interaction coming from a u in p and a $\bar{d}$ in $\bar{p}$ is then $(V_p^u + S_p^u)(V_{\bar{p}}^{\bar{d}} + S_{\bar{p}}^{\bar{d}})$, and the probability for the reverse case is $(S_{\bar{p}}^u)(S_p^{\bar{d}})$. Using $S_p^{\bar{d}} = S_{\bar{p}}^{\bar{d}}$ and $S_p^u = S_{\bar{p}}^u$ we obtain the W^+ polarization as -1 for valence-valence and valence-sea interactions, while for sea-sea interactions the polarization is $+1$ 50% of the time and -1 the other 50%. For the W^-, the polarization is opposite to the W^+ case.

In higher order processes such as initial state gluon radiation or compton scattering, the W is produced with a finite p_T and the polarization is no longer along the proton direction. As will be seen in the next section, the polarization of the W affects the angular distribution of the decay electron, and therefore one needs to model the W polarization in order to calculate the acceptance. We model the W polarization to leading order only, since the next to leading order QCD corrections are small due to a large angular acceptance and to the fact that most of the W cross section is at low p_T.

Because DØ has no central magnetic field, electrons and positrons are indistinguishable, and the polarization of the Z boson is irrelevant to this analysis.

1.5 W and Z Boson Decay

In this dissertation we study the decays of the W and Z bosons to the first generation leptons. The leading order diagrams for these decays are shown in Figure 1.4. The amplitude for the process $W^- \to e\bar{\nu}_e$ is given by

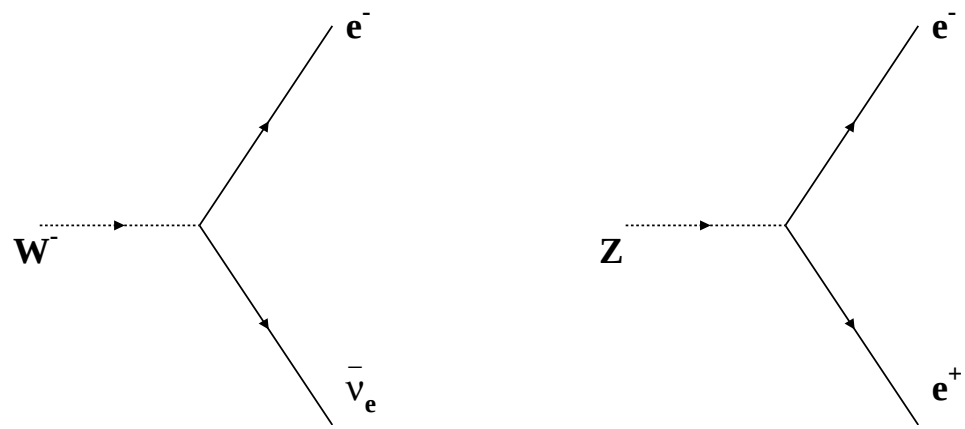

Figure 1.4: Leading order diagrams for $W \to e\nu$ and $Z \to ee$ decays.

$$\mathcal{M} = -i\frac{g_2}{\sqrt{2}}\epsilon_\mu \bar{e}\gamma^\mu P_L \nu \ , \tag{1.49}$$

where ϵ_μ is the polarization wave function of the W, and all other terms are defined in Section 1.3. The amplitude for the process $Z \to e^+e^-$ is given by

$$\mathcal{M} = -i\frac{g_2\epsilon_\mu}{c_w}[\bar{e}_L\gamma^\mu e_L(T_f^3 - Q_f s_w^2) + \bar{e}_R\gamma^\mu e_R(T_f^3 - Q_f s_w^2)] \ . \tag{1.50}$$

Here $T^3 = -1/2$ (0) for left (right) handed electrons, and $Q_f = Q_e = -1$.

1.6 The W Width

From the transition amplitude in Equation 1.49 it is possible to derive an expression for the partial width of the W boson decaying to first generation leptons.

The calculation involves averaging $|\mathcal{M}|^2$ over W polarizations, summing over fermion spins, and integrating over phase space. In the massless e, ν approximation the result is [10]

$$, (W \to e\bar{\nu}_e) = \frac{1}{48\pi} g_2^2 M_W = \frac{G_F}{\sqrt{2}} \frac{M_W^3}{6\pi} \equiv , ^0_W \ . \tag{1.51}$$

In the approximation that all fermion masses are negligible compared to M_W, all lepton and quark decays are related by

$$, (W \to e\bar{\nu}_e) = , (W \to \mu\bar{\nu}_\mu) \ = \ , (W \to \tau\bar{\nu}_\tau) = , ^0_W \tag{1.52}$$

$$, (W \to q\bar{q}') \ = \ 3|V_{qq'}|^2 , ^0_W \tag{1.53}$$

where V is the CKM matrix and the factor of 3 comes from summing over 3 quark colors. Of course, this approximation breaks down for the third generation quarks, since the top quark mass has been measured to be around 175 GeV, even heavier than the W boson, so the decay $W^+ \to t\bar{b}$ is not allowed. Of the hadronic modes, the decays $W^- \to \bar{u}d$ and $W^- \to \bar{c}s$ give the dominant contribution to the total W width, since $|V_{ud}| \approx |V_{cs}| \approx 1$, while the off-diagonal CKM matrix elements are small.

1.6.1 Direct Measurement of Γ_W

In $p\bar{p}$ collisions, the W width can be measured directly following two possible approaches. A full reconstruction of the W decay can be achieved in the hadronic channels, which account for $\approx 68\%$ of the decays. This allows the reconstruction of the W invariant mass distribution, which is a narrow Breit-Wigner resonance. However, the production of jets through QCD processes has a cross section several orders of magnitude higher than the cross section for $p\bar{p} \to W \to$ jets,

making it is impossible to distinguish hadronic W decays from the overwhelming QCD background.

In contrast, the leptonic decays of the W have a high p_T lepton in the final state, a rather unique signature in $p\overline{p}$ collisions. However, the presence of a neutrino in the final state spoils the reconstruction of the W invariant mass distribution. This is because the four-momentum of the neutrino is inferred from apparent energy imbalance in the calorimeter, and since one does not know how much energy is lost down the beam pipe in each collision, the longitudinal momentum of the neutrino cannot be reconstructed. One can therefore only construct the transverse mass of the W, defined by

$$m_T^2 \equiv \left(|\vec{p}_T^{\,e}| + |\vec{p}_T^{\,\nu}|\right)^2 - \left(\vec{p}_T^{\,e} + \vec{p}_T^{\,\nu}\right)^2 , \tag{1.54}$$

which is generally in the range $0 \leq m_T \leq M_W$ (except for a small fraction of events with $m_T > M_W$ arising from the intrinsic width of the W).

The transverse mass distribution for a W produced with zero p_T in a $q\bar{q}'$ collision with center-of-mass energy squared $\hat{s}$ is [10]

$$\frac{d\hat{\sigma}}{dm_T^2} = \frac{|V_{qq'}|^2}{4\pi}\left(\frac{G_F M_W^2}{\sqrt{2}}\right)^2 \frac{1}{(\hat{s} - M_W^2)^2 + (,\ {}_W M_W)^2} \frac{2 - m_T^2/\hat{s}}{\sqrt{1 - m_T^2/\hat{s}}} . \tag{1.55}$$

The divergence at $\hat{s} = m_T^2$ is known as the Jacobian edge of the distribution. Many of the events are produced with $m_T \approx M_W$, where the distribution is most sensitive to the W mass and width. However, experimental energy resolutions cause a significant smearing of the Jacobian edge, and the resulting effective width has large contributions from experimental resolutions. Therefore, it is convenient to measure the W width using events in the region $m_T > M_W$, where experimental resolutions are less important than the natural width of the W in determining the shape of the distribution. However, this region suffers from

very low statistics, and a very large sample of $W \to e\nu$ events are needed to achieve good precision. Direct measurements of the W width with the currently available data have large statistical uncertainties.

1.6.2 Indirect Measurement of Γ_W

The W width can also be determined from a measurement of $\mathcal{R}$,

$$\mathcal{R} \equiv \frac{\sigma(p\overline{p} \to W + X) \cdot B(W \to e\nu)}{\sigma(p\overline{p} \to Z + X) \cdot B(Z \to ee)}, \tag{1.56}$$

using the relationship

$$\mathcal{R} = \frac{\sigma(W)}{\sigma(Z)} \cdot \frac{,\ (Z)}{,\ (Z \to ll)} \cdot \frac{,\ (W \to l\nu)}{,\ (W)}. \tag{1.57}$$

Both $\frac{\sigma(W)}{\sigma(Z)}$ and $,\ (W \to l\nu)$ can be calculated theoretically to high precision [15], and depend only on the pdf's and the couplings of the W and Z bosons to the lepton and quark doublets, and the ratio $,\ (Z)/,\ (Z \to ll)$ has been measured precisely by experiments at LEP [16]. A precise measurement of $\mathcal{R}$ therefore yields a precise measurement of $,_W$. This ratio method has the advantage of yielding the most precise measurements of $,_W$ to date, and the disadvantage that it depends crucially on the assumption that the standard model correctly describes the couplings between the gauge bosons and the fermions.

1.7 Previous Measurements

The W width has been measured indirectly by the UA1 [3], UA2 [4], CDF [5], and DØ [6] collaborations. The most recent results are $,_W = 2.044 \pm 0.093$ GeV from DØ and $,_W = 2.064 \pm 0.084$ GeV from CDF. Both used a method which is based on measuring the ratio $\mathcal{R}$ of the $W \to e\nu$ and $Z \to ee$ cross sections.

The W width has also been measured directly by the LEP experiments [7] by looking at the W pair cross section as a function of the center-of-mass energy, and by CDF [17] by looking at the high-mass tail of the transverse mass spectrum. Their current results are , $_W = 1.74 \pm 0.91$ GeV and , $_W = 2.11 \pm 0.32$ GeV, respectively.

1.8 Units and Conventions

We use units in which

$$\hbar = c = 1,$$

and therefore the following dimensional relationships hold:

$$[\text{time}] = [\text{length}] = [\text{energy}]^{-1} = [\text{momentum}]^{-1} = [\text{mass}]^{-1}.$$

Mass and momentum are given in units of energy, GeV, instead of GeV/c^2 and GeV/c. Throughout this dissertation, the following conventions are used:

- W refers to either W^+ or W^-.
- e refers to either e^+ or e^-, and the term "electron" refers to either electron or positron.
- ν refers to either ν_e, ν_μ, ν_τ, $\bar{\nu}_e$, $\bar{\nu}_\mu$, or $\bar{\nu}_\tau$, and the lepton flavor is assumed to be understood from the context.

Therefore $Z \to ee$ means that the Z boson decays to an e^+e^- pair and $W \to e\nu$ means either $W^+ \to e^+\nu_e$ or $W^- \to e^-\bar{\nu}_e$.

1.9 Outline

This dissertation is organized as follows. Chapter 2 describes the DØ detector, emphasizing the components important for this analysis. Chapter 3 describes the criteria used to select the $W \to e\nu$ and $Z \to ee$ data samples. Chapter 4 describes the calculation of the kinematic and geometric acceptance for the selection criteria. Chapter 5 presents the measurement of the event selection efficiencies. Chapter 6 presents an estimate of the backgrounds in the data samples. Chapter 7 describes the luminosity measurement at DØ. The results and their implications are discussed in Chapter 8. Finally, the conclusions and future prospects are discussed in Chapter 9.

Chapter 2

The Tevatron and the DØ Detector

This chapter gives a brief description of the experimental apparatus that was used. The Tevatron Collider provides a beam of very high energy protons and antiprotons which go around the accelerator ring in opposite directions and are made to collide near the center of the DØ detector. A more detailed description of the Tevatron is provided in Ref. [18], and a complete description of the DØ detector can be found in Ref. [19]. Since the accelerator and detector have been described in all previous DØ thesis, this chapter benefits and draws heavily from the work of other students, and in particular, from Ref. [44].

2.1 The Tevatron Collider

The Fermilab Tevatron [20] at Fermi National Accelerator Laboratory (FNAL), is currently the highest energy particle accelerator in the world, where protons and antiprotons collide head on with a center of mass energy of 1.8 TeV. The Tevatron, shown in Figure 2.1, is the last of a chain of accelerators. The beam starts with protons taken from hydrogen gas atoms which are then boosted to higher and higher energies in a series of accelerators until they eventually reach

an energy of 900 GeV. All accelerators use electric fields to give charged particles a boost. *Linear* accelerators consist of a series of gaps inmersed in an electric field arranged in a linear configuration. Every time a charged particle crosses such a gap, it gets a "kick" from the field. Alternatively, a single gap can be used several times by containing the particles in a closed orbit, making use of magnetic fields to bend the particle trajectories. Each time a particle goes through the electric field gap, its energy is increased, and the magnetic field is increased in a synchronized fashion so that the particle remains in a stable orbit. This type of accelerator is called a *synchrotron*, of which the Tevatron is an example.

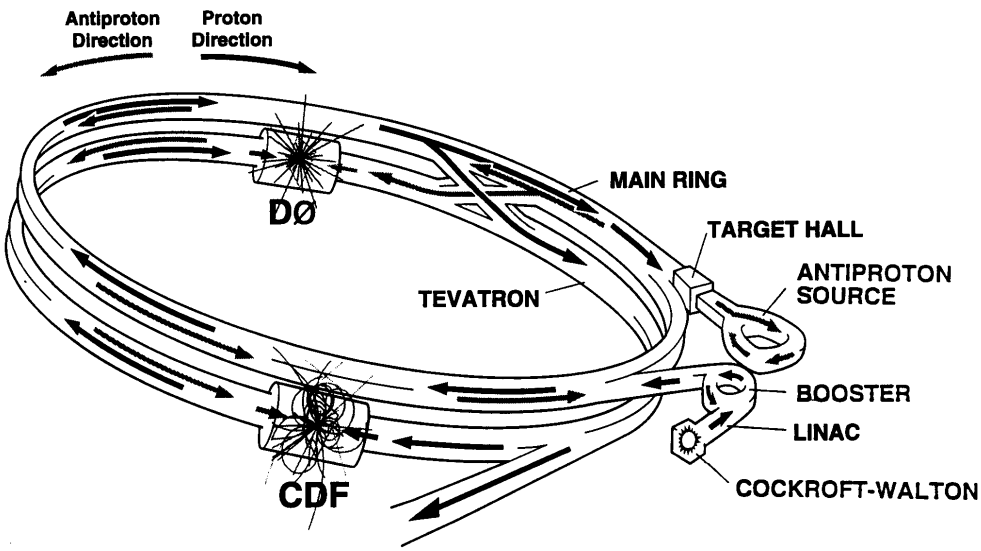

Figure 2.1: Fermilab Tevatron Collider complex.

The Fermilab accelerator is composed of the following parts:

1. The Preaccelerator

2. The Linac

3. The Booster

4. The Main Ring

5. The Antiproton Source

6. The Tevatron

The origin of the beam is a bottle of pressurized hydrogen gas. The hydrogen atoms are ionized by the addition of electrons, thus forming H^- ions. These H^- ions are accelerated to an energy of 750 KeV by an electrostatic Cockroft-Walton accelerator. Once at 750 KeV, the ions are injected into the Linac. The Linac is a 150 m linear accelerator, which raises the energy of the ions to 400 MeV. Once the ions emerge from the Linac, they are passed through a carbon foil which strips off the electrons, thus creating protons. The protons are then steered into the Booster, a synchrotron of diameter 151 m, which increases the energy of the protons to 8 GeV. The protons are then injected into the Main Ring, a synchrotron 1 Km in radius, composed of 1000 conventional magnets. Once in the Main Ring, the protons are accelerated to 120 GeV, and compressed into short bunches (with $\sim 2 \cdot 10^{12}$ protons per bunch). Some of the bunches are accelerated further to an energy of 150 GeV for subsequent injection into the Tevatron. The remaining bunches (still at an energy of 120 GeV) are directed towards the Antiproton Source.

Antiprotons are produced by directing the 120 GeV proton bunches into a nickel/copper target (in the Target Hall). Among the resultant debris of the collisions, antiprotons are produced at a rate of about 20 antiprotons for every million protons sent to the Target Hall. This process is called *pbar stacking*. These antiprotons have a wide angular and energy spread, so they are first focused using a lithium lens, and then a magnetic field is applied to select 8

GeV antiprotons that are transported to the Debuncher, a storage ring which equalizes all antiproton energies. This process runs continuously until the next bunch of antiprotons arrives, about 2.4 s later. At this point, the monochromatic antiproton beam with $\sim 2 \cdot 10^6$ antiprotons is transfered to a second antiproton storage ring, known as the Accumulator. When about $4 \cdot 10^{11}$ antiprotons are stored (which typically takes 8 to 12 hours), they are transfered into the Main Ring, where their energy is increased to 150 GeV, and are injected into the Tevatron in the direction opposite to that of the proton beam.

The Tevatron is located in the same tunnel as the Main Ring and 1 m below it, except at two intersection regions where detectors are located: the B0 intersection region for the CDF detector and the D0 intersection region for the DØ detector. The Tevatron is a synchrotron composed of super-conducting magnets which operate at a temperature of 4.6 K and can produce fields of approximately 3 Tesla, thus allowing higher energy protons and antiprotons to remain in orbit. In the final acceleration phase, six bunches of protons (with $\sim 10^{11}$ protons/bunch) and six bunches of antiprotons (with $\sim 5 \cdot 10^{10}$ antiprotons/bunch) are ramped to the maximum energy of 900 GeV. Once at this energy (called *flattop*), the beams are strongly focussed and made to collide at the B0 and D0 experimental areas. The proton and antiproton beams are kept from colliding at other points by the use of electrostatic separators. Over time, interactions of the beam with residual beam pipe gases cause a decrease in the size and density of the proton and antiproton bunches. The beam lifetime (also called *store length*) was typically 12 to 18 hours. Production of antiprotons is continuous during collisions in order to refill the Tevatron with new bunches as quickly as possible: typical down-time between any two stores was on the order of 2 hours. The

interaction rate of the $p\overline{p}$ collisions is given by

$$R = \sigma L \tag{2.1}$$

where σ is the cross section for the beam-beam interaction, and L is the *instantaneous luminosity* (L has dimensions of Area^{-2}time^{-1}). The instantaneous luminosity is a measure of the intensity of the beam, and therefore it is proportional to the number of particles in each bunch (N_1 and N_2), to the number of bunches in each beam (n), and to the revolution frequency of each bunch (f), and it is inversely proportional to the cross sectional area of the beams (A):

$$L = fn\frac{N_1 N_2}{A} \tag{2.2}$$

At the begining of a store, when the size and density of the bunches are higher, the instantaneous luminosity is higher. At high instantaneous luminosities there can be more than one $p\overline{p}$ interaction per beam crossing (this is called *multiple interactions*), an issue which is discussed further in Chapter 7.

2.2 The DØ Detector

The DØ detector, described in detail elsewhere [19], is a general purpose detector for the study of high energy $p\overline{p}$ collisions. It weighs 5500 tons, and measures 13 m (height) $\times$ 11 m (width) $\times$ 17 m (length). It provides very good identification of electrons and muons, and good measurement of high p_T jets and missing transverse energy. The detector consists of four major components:

1. A non-magnetic central tracking system for measuring the trajectories of charged particles.

2. Hermetic central and forward uranium/liquid-argon sampling calorimeters for measuring the energies of electrons, photons, and hadrons.

3. A muon spectrometer outside of the calorimeter used for measuring the momenta of muons.

4. A trigger and data acquisition system which selects physics processes of interest.

The following sections will describe each of these components. Figure 2.2 shows an isometric, cut away view of the DØ detector. Going from the beam pipe outwards, the figure shows the central tracking detectors, the electro-magnetic and hadronic calorimeters, and the muon spectrometer, which consists of three layers of proportional drift tube chambers (PDTs) with an iron toroid between the first two PDT layers. The figure also shows the Main Ring pipe, which passes through the hadronic calorimeter.

2.3 DØ Coordinate System

In DØ we use a right-handed coordinate system where the positive z-axis points in the direction of the proton beam, the positive y-axis points straight up, and the x-axis is therefore in the horizontal plane, perpendicular to the beam pipe. The angular coordinates θ and ϕ are the polar and azimuthal angles, respectively, relative to the proton beam direction $\hat{z}$, and are defined such that $\theta = 0$ along the $\hat{z}$ direction and $\phi = 0$ along the $\hat{x}$ direction. The radial distance ρ is the perpendicular distance from the beam line. For reasons which are explained in

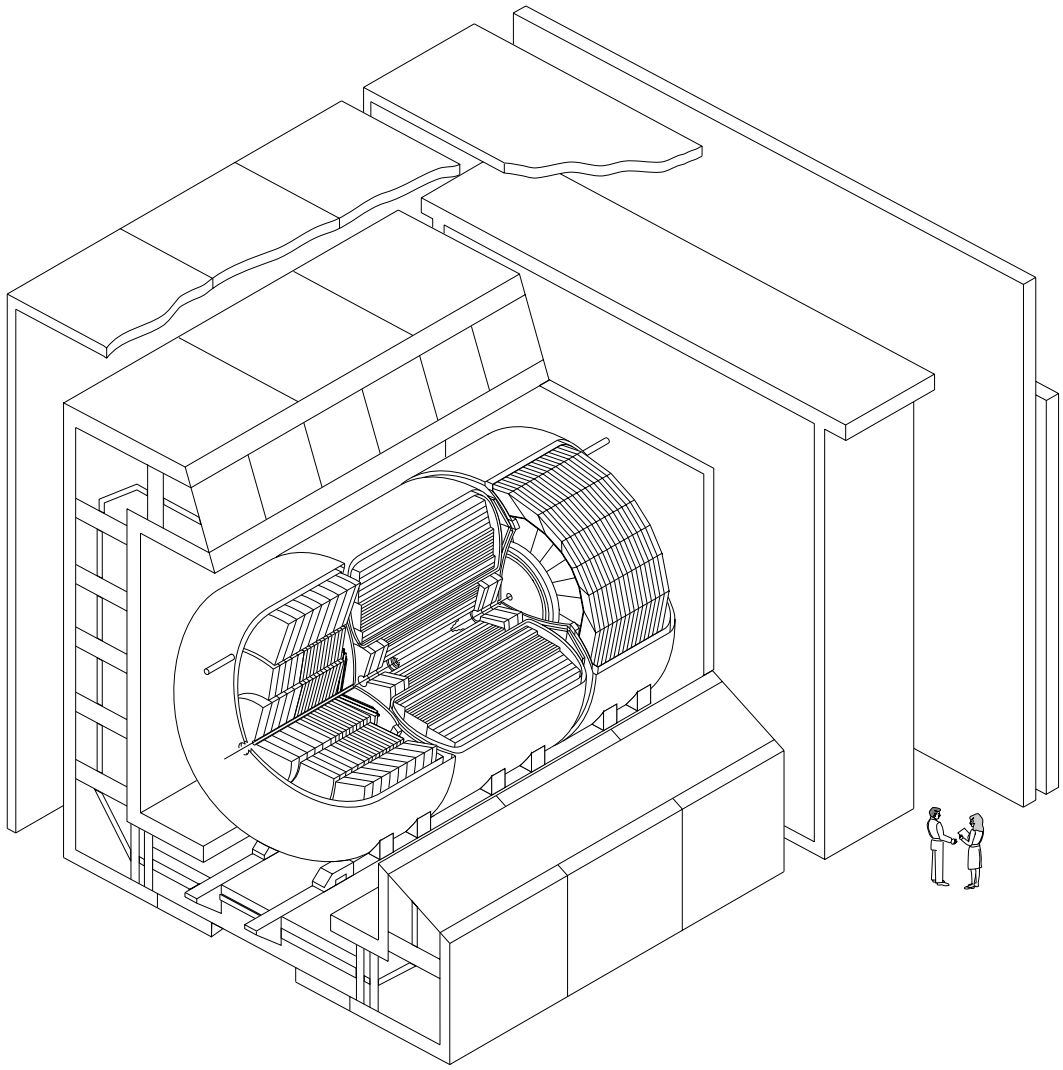

Figure 2.2: Isometric view of the DØ detector.

Appendix A, it is convenient to replace θ with the *pseudorapidity*, η, defined as

$$\eta \equiv -\ln\left[\tan\left(\frac{\theta}{2}\right)\right]. \tag{2.3}$$

Because many products of a $p\overline{p}$ collision escape detection by going down the beam pipe, it is often convenient to project the momentum and energy of parti-

cles onto a plane perpendicular to the beam pipe. This is especially true when measuring neutrino momenta, since neutrinos are inferred by an apparent momentum imbalance in the calorimeter, and their longitudinal momentum cannot be reconstructed. In the transverse plane, however, momentum and energy conservation constrains can be used. Transverse momentum (p_T) and transverse energy (E_T) are defined as:

$$p_T = p \sin\theta \tag{2.4}$$

$$E_T = E \sin\theta. \tag{2.5}$$

2.4 Central Tracking System

The Central Tracking Detectors (CD) at DØ are used to reconstruct the trajectories of charged particles. The design is simplified by the absence of a magnetic field. Without the need to measure the momenta of charged particles, emphasis is placed on good two-track resolving power, high efficiency, and good measurement of the energy loss due to ionization within the tracking volume, dE/dx (which distinguishes between electrons and closely spaced photon conversion pairs, $\gamma \to e^+e^-$). In addition, the central trackers are responsible for making a precise measurement of the location of the interaction vertices for each event, as well as improving the accuracy of the muon momentum measurements.

The central tracking system is shown in Figure 2.3. It consists of four detector subsystems: a vertex drift chamber (VTX), a transition radiation detector (TRD), a central drift chamber (CDC), and two forward drift chambers (FDC). The VTX, TRD, and CDC have a cylindrical geometry and are arranged concentrically around the beam pipe. The FDCs are oriented perpendicular to the

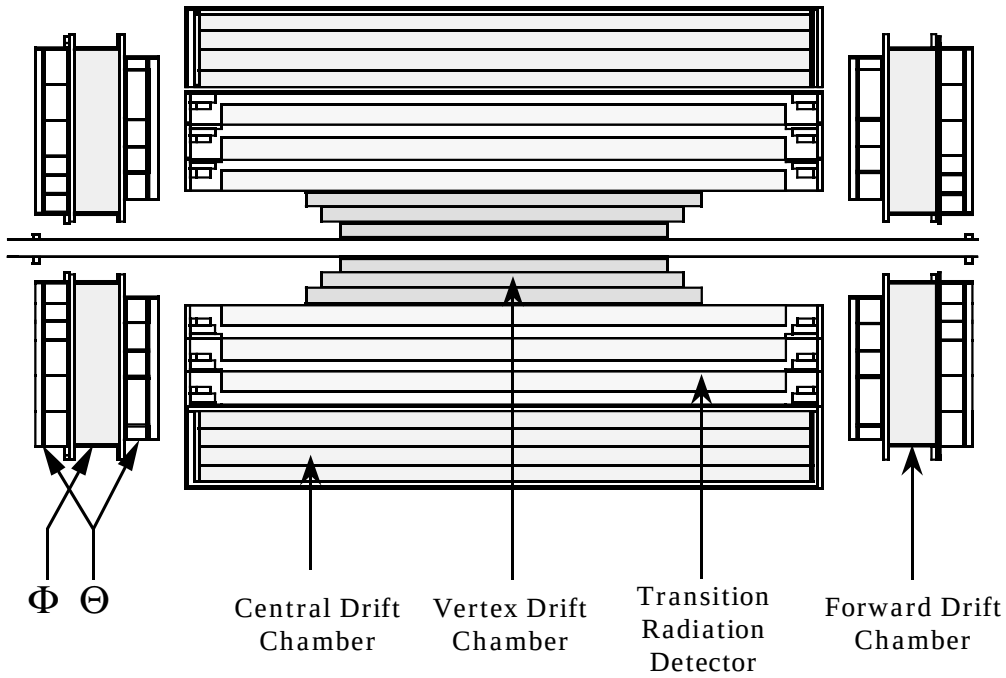

Figure 2.3: Side view of the DØ central tracking detectors.

beam pipe, and are composed of three chambers: one Φ chamber, with sense wires oriented axially to measure the ϕ coordinate of the hits, is sandwiched between two Θ chambers (rotated from each other in ϕ by 45°). Each Θ chamber contains four quadrants with sense wires oriented perpendicular to the axial direction to measure the θ coordinate of the hits. Figure 2.4 illustrates the layout of the FDC. The entire central tracking system is contained within the inner cylindrical aperture of the calorimeters, of radius $r = 75$ cm and length $l = 270$ cm. A detailed description of the central tracking detectors can be found in Refs. [21, 22, 23, 24, 25, 26, 27, 28, 29, 30]. The remaining of this section will briefly describe the basic operating principles of the wire drift chambers.

The VTX, CDC, and FDC are wire drift chambers. When a charged particle passes through a gas, it creates electron/ion pairs along its trajectory (it *ionizes*

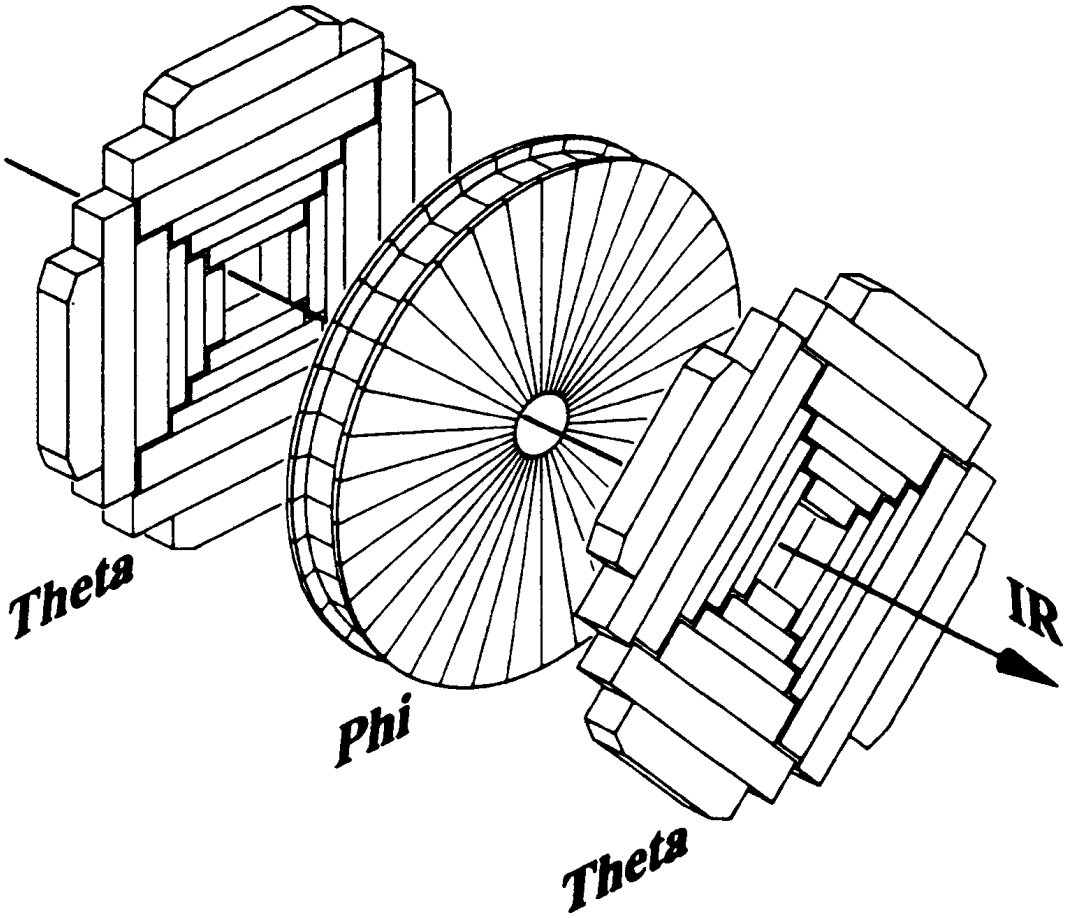

Figure 2.4: Layout of the FDC.

the gas). In the presence of an electric field, the electrons will drift towards the positively charged *sense wire*. The ions will drift in the opposite direction, but they move considerably slower because of their larger mass, and their motion can be neglected. The small diameter of the sense wire produces a very strong electric field in its immediate vicinity which accelerates the drift electrons to energies high enough to induce further ionization. In this manner, the number of drift electrons increases exponentially, creating an *avalanche* that gives rise to a measurable electrical current. The difference between the known $p\overline{p}$ collision time and the arrival time of the pulse at the sense wire is called the *drift time*,

which, combined with a knowledge of the drift velocity of the electrons in the gas, is used to infer the drift distance of the electrons. Multi-wire drift chambers have several sense wires strung in parallel, and their positions are well known. From the drift time and inferred drift distances, the trajectories of charged particles are reconstructed. A measurement of the energy loss due to ionization of the gas is achieved by measuring the total collected charge in each sense wire. Higher energy loses result in a higher number of ionized gas molecules, which in turn results in a higher integrated charge in the sense wires. By measuring $\int Idt$ in each sense wire we can therefore measure dE/dx. Further discussion on drift chambers can be found in Ref. [31].

The TRD at DØ is used primarily for electron identification, as it can distinguish electrons from heavier hadrons, but it is not used in this analysis.

2.5 Calorimeter

The design of the DØ detector places very heavy emphasis on calorimetry. The calorimeter is the most important part of DØ, as it provides the only means to measure the energy of electrons, photons, and jets. It also plays a vital role in the identification of electrons, muons, taus, photons, jets, and neutrinos, and can be used to measure their position because of its fine segmentation.

The interaction of photons and electrons with matter at energies well above 10 MeV occurs primarily via the creation of electron/positron pairs and the Bremsstrahlung mechanism[1]. An electromagnetic shower develops as an alter-

[1] This is the mechanism where a charged particle interacts with the Coulomb field surrounding a nucleus and emits an energetic photon.

nating sequence of interactions of these two types. For example, a primary electron will lose energy by emitting a photon. The photon will convert into an e^+e^- pair, which in turn will lose energy by emitting other photons. The process keeps occurring and the shower keeps developing until the energy of all secondary particles reaches the level where ionization losses and atomic excitations become important. Since, at high energies, the angles of emission of the electrons and photons are small, the shower develops primarily in the direction of motion of the original electron. The energy loss of an electromagnetic particle is characterized by the *radiation length* $X_\circ$:

$$\frac{dE}{E} = -\frac{dx}{X_\circ} \,. \tag{2.6}$$

The radiation length is dependent on the absorbing medium[2]: it is 0.32 cm for uranium and 13.5 cm for liquid argon. The typical transverse size of an electromagnetic shower in the DØ calorimeter is about 1–2 cm.

The physical process governing the interaction of a hadronic particle with matter is quite different from the one just described for electromagnetic particles. *Hadronic showers* are produced from the inelastic collisions of hadrons with the surrounding atomic nuclei, or from the multi-particle production of slow pions and kaons. These secondary hadrons will in turn undergo additional inelastic collisions, or produce more slow hadrons. Shower development ceases once ionization losses and nuclear absorption become dominant. It is important to note that typical secondary hadron production occurs with a transverse momentum of ~ 350 MeV/c [32]. Hence, hadronic showers tend to be more spread out laterally than electromagnetic ones. The typical transverse size of a hadronic

[2]The radiation length of a material of atomic number A, and charge Z can be approximated [32] as $X_\circ$ [g/cm^2] $= 180A/Z^2$.

shower in the DØ calorimeter is about 10 cm. The longitudinal development of the hadronic showers scales with the nuclear absorption (or interaction) length of the medium, $\lambda_\circ$. The absorption length for uranium is $\lambda_\circ = 10.5$ cm, thus causing the hadronic shower to be much longer than an electromagnetic shower of similar energy. Occasionally, a hadronic shower can fluctuate electromagnetically. If a neutral pion decays into a pair of photons, the jet will then look like an electromagnetic shower. This results in some small fraction of instrumental misidentification of QCD jets as electrons, and constitutes the dominant source of background in this analysis. This issue is discussed at some length in Chapter 6.

The DØ calorimeter is a *sampling* calorimeter, in which the shower development of an incident particle is periodically sampled in sensitive layers via the ionization of an active medium. Layers of passive absorber placed between the sampling layers make it possible to build a compact, hermetic device. Since most of the energy ends up being absorbed by the passive material, only a small fraction is read out, or sampled, and a correction proportional to this *sampling fraction* is needed to measure the total energy of incident particles.

The DØ calorimeter is composed primarily of plates of uranium absorber, separated by gaps of liquid argon that function as the sensitive ionization medium. It consists of three parts, a central calorimeter (CC) and two forward, or end calorimeters (EC). These are segmented longitudinally into an inner electromagnetic section (EM), and an outer hadronic section (HAD). The EM calorimeter is segmented longitudinally into four layers, the third being at the shower maximum for electromagnetic showers, and it is about 20 radiation lengths ($X_\circ$) deep. The HAD calorimeter is likewise segmented into a fine hadronic section

(FH) with thicker uranium plates, and a coarse hadronic section (CH) with thick copper or stainless steel plates. The entire calorimeter is about 7 nuclear absorption lengths ($\lambda_\circ$) deep in the CC at $\eta = 0$ and about 10 $\lambda_\circ$ in the EC at $\eta = 4.5$. Figure 2.5 shows the different calorimeter sections.

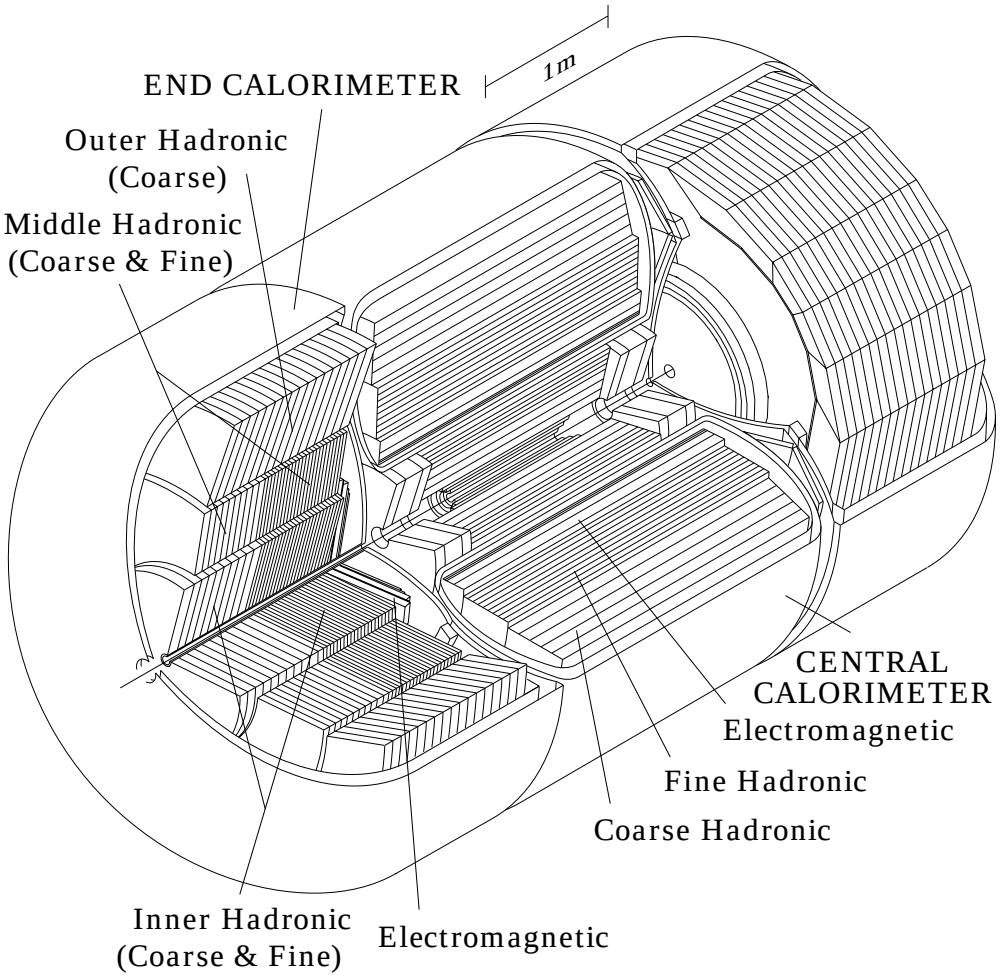

Figure 2.5: Isometric view of the DØ calorimeter system.

The calorimeter is also segmented transversely in *pseudoprojective* towers, each covering approximately $\delta\eta \times \delta\phi = 0.1 \times 0.1$, with a further segmentation of 0.05×0.05 in the third EM layer. Figure 2.6 shows the segmentation of the DØ calorimeter. The CC electromagnetic calorimeter covers $|\eta| \leq 1.1$, while the EC

electromagnetic calorimeter covers $1.4 \leq |\eta| \leq 4.2$. The hadronic calorimeter system provides full coverage to $|\eta| \leq 4.2$. The CC electromagnetic calorimeter is divided into 32 modules in ϕ, with a small uninstrumented region at each module boundary.

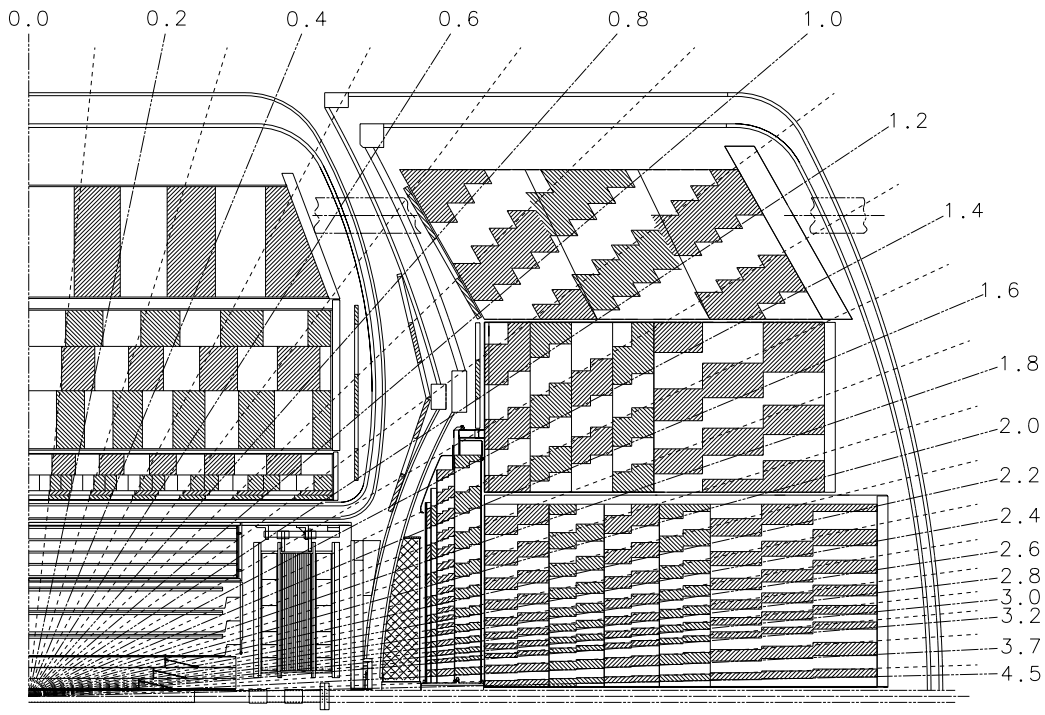

Figure 2.6: Side view of one quadrant of the calorimeters. The alternating shaded and unshaded regions denote individual calorimeter towers. Also shown are lines of constant pseudorapidity intervals.

2.6 The Muon Spectrometer

Muons are identified by their very penetrating nature: their lifetime of 2.2 μs is much larger than the scale of the detector (thus making them stable for all practical purposes), and their mass of $\approx 200 m_e$ is too large to initiate an electro-

magnetic shower[3]. The calorimeter is made thick enough that only muons are likely to penetrate its outermost layers. These muons are detected in proportional drift tube (PDT) chambers surrounding the calorimeter. The principle of operation of these chambers is nearly identical to that of the VTX, CDC and FDC (see Section 2.4). In addition, their momenta can be measured since the three layers of PDT chambers are on either side of toroidal magnets (see Figure 2.2). The momentum resolution is most easily parameterized in terms of the inverse momentum $k = 1/p$. This resolution is measured to be:

$$\frac{\delta k}{k} = 0.18 \oplus \frac{0.03}{k} \ . \tag{2.7}$$

The DØ muon system is not used in this analysis. A brief description was given for completeness, and the interested reader is referred to [19, 33] for details.

2.7 Trigger and Data Acquisition

The Tevatron operates with a 3.5 μs interval between bunch crossings, which amounts to a rate of $\sim$ 286 kHz. It is neither practical nor interesting to read out the entire detector at each beam crossing. Most of the physics processes of interest have a very small cross section compared to the total $p\overline{p}$ cross section (see Chapter 7 for a discussion of the total $p\overline{p}$ cross section). The process of choosing the desired events is called *triggering*, and it is carried out in different stages. At each stage there is a limited amount of information available for making the choice, and a limited amount of time in which to do so. The DØ trigger system consists of three different trigger levels, each with increasingly

[3]Muons with energies less than $\sim$ 500 GeV do not readily produce an electromagnetic shower.

sophisticated event characterization, called Level-Ø, Level-1, and Level-2. A brief description of each trigger level follows.

2.7.1 Level-Ø

The Level-Ø trigger uses a set of scintillation counters (called LØ counters) mounted on the front face of the forward calorimeters. The spectator quarks in an inelastic $p\overline{p}$ collision will hadronize in the far forward region. The Level-Ø trigger therefore looks for a coincidence between signals from the LØ counters at each end of the detector. This requirement reduces the rate from 286 kHz down to about 150–200 kHz. The counters are more than 99% efficient in detecting inelastic $p\overline{p}$ collisions. The Level-Ø system [34] performs several functions:

- Trigger on inelastic $p\overline{p}$ collisions;
- Luminosity monitoring;
- Identification of multiple interactions within one beam crossing;
- Fast determination of the z-coordinate of the interaction vertex.

The LØ counters consist of two layers of 1.6 cm thick scintillators covering $1.9 \leq |\eta| \leq 4.3$. Each layer has ten short (7 cm $\times$ 7 cm) scintillators, each glued to a single photo-multiplier (PMT), and four long (7 cm $\times$ 65 cm) scintillators, each glued to two PMTs, one at each end. The average time resolution is 240 ps for the short scintillators and 510 ps for the long ones. The two layers are oriented perpendicular to each other. The counters are located at $z = \pm 140$ cm, and provide a fast interaction trigger (within 800 ns) and a vertex resolution of 15 cm, which improves all E_T and $\not{E}_T$ calculations at Level-1 and Level-2.

2.7.2 Level-1

The Level-1 system is a hardware trigger that uses coarse information from the calorimeter, the muon system, the LØ counters, and the accelerator timing signals in order to select events of interest. At its heart lies the Level-1 trigger framework [35, 36], a programmable hardware processor that coordinates various vetoes which can inhibit triggers, accounts for trigger rates and dead-times, and digitizes the data before handing the event to the Level-2 trigger. It consists of a network of 256 AND–OR terms (called *latch bits*). Each of these bits contains specific requirements, such as the presence of an EM trigger tower with $E_T > 10$ GeV. The 256 input AND–OR trigger terms are reduced to 32 output terms, corresponding to 32 specific Level-1 triggers. Each Level-1 trigger is a logical combination of the 256 input terms, whether that term is required to be asserted, negated, or ignored. Each trigger has also a programmable prescale[4] that can be used to control the input rate to the Level-2 trigger.

The event rate out of Level-1 is roughly 100 Hz, and it makes most decisions within the 3.5 μs interval between beam crossings. Trigger vetoes are related to any Main Ring activity (recall that the Main Ring passes through the calorimeter) as well as to any required prescales to reduce the output rate. The Level-1 and Level-1.5 calorimeter triggers use energy measurements in trigger towers of size 0.2×0.2 in $\eta \times \phi$ space and the LØ z measurement to calculate global variables such as total E_T, $\not{E}_T$, EM E_T, and hadronic E_T. For a detailed description of the Level-1 and Level-1.5 calorimeter triggers, see Refs. [35, 36, 37, 38].

[4]Setting the prescale to some integer value N causes the trigger to pass the event once in every N times that its trigger is satisfied.

2.7.3 Level-2

The Level-2 system [39, 40] functions as the DØ data acquisition system and the Level-2 software trigger. It is composed of 48 parallel microprocessors and reduces the 100 Hz input rate to 2 Hz. Software filtering [41] of events on each of the Level-2 nodes is accomplished by a series of filter *tools*. Each tool has a specific function related to identification of a type of particle or event characteristic. Jets, muons, calorimeter EM clusters, track association with calorimeter clusters, scalar E_T (ΣE_T), and $\not\!\!E_T$, have their own filtering tools. For example, an electron filter tool may depend on a minimum number of calorimeter EM clusters, minimum E_T for each cluster, and track association with the clusters. The tools are associated in particular combinations and ordered into *scripts*. Each of the 32 Level-1 trigger bits is associated with one or more scripts. For example, a single electron trigger from Level-1 can have several Level-2 scripts depending upon the E_T threshold or other features in the event (e.g. energy isolation or the presence of $\not\!\!E_T$). There are a maximum of 128 Level-2 scripts. For each Level-1 bit that is passed, a call is made to its Level-2 associated scripts. If any of the Level-2 scripts are passed, the event is sent to the online cluster to be logged and recorded on permanent storage media.

Chapter 3

Data Event Selection

Candidate $W \to e\nu$ and $Z \to ee$ events are identified through their decay to an electron and a neutrino, or to two electrons which have an invariant mass consistent with the mass of the Z boson, respectively. The decay leptons typically have a transverse energy comparable to half the mass of the vector boson, or about 40 to 45 GeV. The particles that balance the component of the W or Z boson momentum transverse to the beam axis are referred to as the "recoil". Particles from the break-up of the proton and anti-proton in the inelastic collision are referred to as the "underlying event". Particles from the recoil and underlying event are indistinguishable. The transverse momentum distribution of the W or Z boson peaks at about 7 GeV and falls off rapidly at higher p_T values.

The $W \to e\nu$ and $Z \to ee$ event selection starts by imposing a set of trigger requirements. Events which pass the W or Z triggers are written to tape for subsequent analysis. Offline, further selection requirements are applied in order to obtain samples which are as large as possible while keeping the background contamination at reasonably small levels. Backgrounds in the $W \to e\nu$ and $Z \to ee$ samples are discussed in Chapter 6.

The Tevatron's physics collider run lasted from 1992 to 1996. This run, known as Run 1, consists of three running periods: Run 1a, Run 1b, and Run 1c. This analysis uses data only from Run 1b [1], which amounts to an integrated luminosity of 84.5 pb^{-1}.

3.1 Event Reconstruction

The information recorded by the DØ detector is in the form of digital signals: pulse heights, widths and times, which need to be interpreted as physics objects. This complicated task is performed by the standard reconstruction software package (DØRECO). DØRECO starts by processing the raw data into high-level objects, such as energy clusters in the calorimeters or tracks in the tracking and muon systems. These objects are in turn combined to form the physical particles that originated in the $p\overline{p}$ collisions: electrons, photons, jets, muons, and neutrinos ($\not\!\!E_T$). A description of the event reconstruction process at DØ is outside the scope of this dissertation. The interested reader is referred to [44] for a nice discussion of event reconstruction and particle identification.

3.2 Electron Identification

Electrons from W and Z boson decays typically have a large E_T, and are isolated from other particles. They are associated with a track in the tracking system,

[1] A measurement of $\mathcal{R}$ using Run 1a data has been published [6], and Run 1c data is not used because there were no $W \to e\nu$ triggers in use during this run. The additional gain in statistics was not deemed worthwhile, so the DØ Collaboration elected to focus on the search for hadronically-decaying W bosons, which required considerable trigger bandwidth.

and with a large deposit of energy in one of the EM calorimeters.

The emphasis of the algorithms used in DØRECO is towards maximum efficiency in the reconstruction of electrons and photons. This implies that a fair amount of background is present at this point, and that the task of further separating it from the real signal is left to the individual analyses. Standard techniques have been developed in the identification of electrons, which introduce additional criteria that reduce the background considerably while retaining most genuine electrons for the analysis. Two of the criteria rely on calorimeter information and exploit the difference between an electromagnetic and a hadronic shower: the electromagnetic energy fraction (f_{em}) and the H-matrix chi-squared (χ^2_{hm}), which is derived from an analysis of the shower shape. The third criterion, shower isolation fraction (f_{iso}), also relies on calorimetric information. However, this criterion is not based on the shower itself: it is a topological cut which is consistent with the decay of electrons from W and Z gauge bosons. Finally, the fourth criterion is based on calorimetric and tracking information: track match significance (S_{trk}) quantifies the quality of the track matching performed for electrons, and is used to reject photons which are copiously produced in QCD events through $\pi^0 \to \gamma\gamma$ decays.

3.2.1 Electromagnetic Energy Fraction

Electrons and photons have, by definition, a large electromagnetic fraction: 90% of the cluster energy must be deposited in the EM layers of the calorimeter in order to be considered electrons or photons by DØRECO. For electrons originating from decays of W and Z bosons, this requirement is quite loose. Figure 3.1 shows

the distribution of $f_{\rm em}$ for *probe* electrons[2] from $Z \to ee$ decays, and "electrons" from multijet-triggered data, which are required to have small $\not\!\!E_T$. The former is dominated by signal, while the latter is dominated by background (highly electro-magnetic hadronic showers, or *jets*, which fake an electron). Additional background rejection is obtained by the cut $f_{\rm em} > 0.95$. A central electron is an electron in the CC, and a forward electron is an electron in the EC.

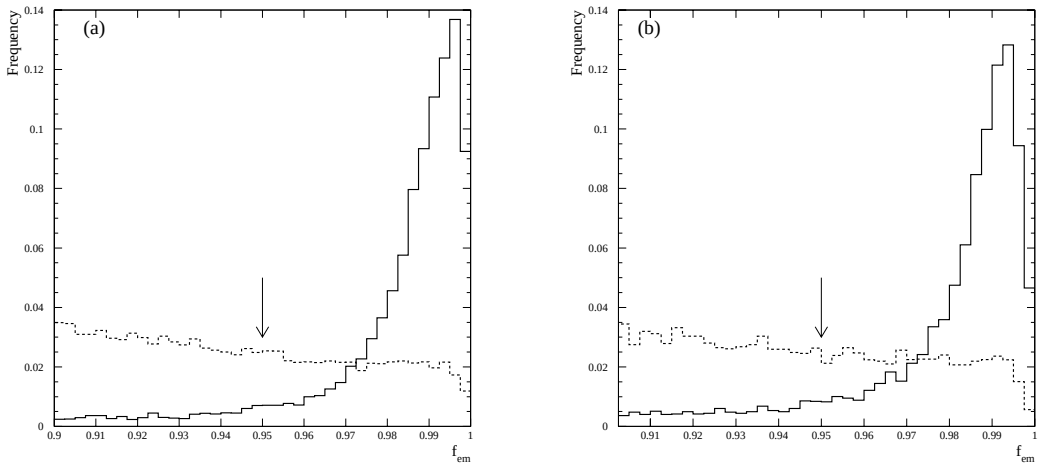

Figure 3.1: EM fraction $f_{\rm em}$ distribution for probe electron candidates from $Z \to ee$ data (solid) and electron candidates from multijet triggered data (dashed), for (a) central electrons and (b) forward electrons. No other cuts have been applied to the probe or multijet electron candidates. The relative normalization is arbitrary, for shape comparison.

[2]If one electron in a $Z \to ee$ event passes all the electron ID requirements, has $E_T > 25$ GeV, and forms an invariant mass close to the Z mass with a second electron, the second electron is called a probe electron (see Section 5.1).

3.2.2 Shower Shape Analysis

The shower shape of an electromagnetic object (electron or photon) can be characterized by its longitudinal and transverse profile: it is dependent on the fraction of cluster energy deposited in each cell of the calorimeter. These fractions, besides being dependent on the incident electron energy and impact position, are also correlated: a shower which fluctuates and deposits a large fraction of its energy in the first layer will then deposit a smaller fraction in the subsequent layers and vice versa. To fully account for all possible correlations, a covariance matrix M of 41 observables is built which characterizes the "electron-ness" of the shower [45, 46, 47]. The observables are the fractional energies in layers EM1, EM2 and EM4 of the calorimeter, and the fractional energy in each cell of a 6×6 array of EM3 cells in $\eta - \phi$ space centered on the most energetic tower in the cluster. In addition, the logarithm of the cluster energy is included as an observable to account for the dependence of the fractional energy deposits on the cluster energy. Finally, the z-coordinate of the interaction vertex (z_{vtx}) is included, to account for the dependence of the shower shape on the angle of incidence into the calorimeter. Since the calorimeter geometry is η-dependent[3], 37 different matrices M are built, one for each of the 37 pseudorapidity towers in half of the calorimeter. The other half, with negative z-coordinates, is handled using reflection symmetry.

The matrix elements are computed using a reference sample of Monte Carlo electrons[4] with a wide range in energies (10 GeV to 150 GeV), and a wide range

[3]The transverse cell size is a function of the pseudorapidity.

[4]Monte Carlo simulation of the calorimeter is performed using GEANT [48].

in z_{vtx}. For two observables x_i and x_j, the correlation is defined as:

$$M_{ij} = \frac{1}{N}\sum_{n=1}^{N}(x_i^n - \overline{x}_i)(x_j^n - \overline{x}_j) \ , \tag{3.1}$$

where N is the number of Monte Carlo electrons used, x_i^n is the value of the ith observable of the nth reference electron and $\overline{x}_i$ is the mean of the ith observable for the entire reference set. These matrices were verified using test beam electrons in order to ensure that they adequately describe real data.

For a particular shower, characterized by the observables x_i', the covariance parameter:

$$\chi^2_{hm} = \sum_{i,j=1}^{41}(x_i' - \overline{x}_i)H_{ij}(x_j' - \overline{x}_j) \ , \tag{3.2}$$

is computed, where $H = M^{-1}$ is the error matrix obtained from the inverse of the correlation matrix M. This parameter $\chi^2_{\rm hm}$ measures how closely the cluster shape is consistent with an electromagnetic shower. In general, the values of the observables x_i are not normally distributed, and therefore the covariance parameter $\chi^2_{\rm hm}$ does not follow a true χ^2 distribution. Nevertheless, the covariance parameter offers strong rejection power against background sources, since only genuine electrons will have low $\chi^2_{\rm hm}$ values, as illustrated in Figure 3.2. It should be noted that this figure is used for illustration only, and efficiencies are calculated from the $Z \to ee$ data.

In this analysis, electron candidates are required to have $\chi^2_{\rm hm} < 100$. The effect of this cut on probe electrons from $Z \to ee$ decays and "electrons" from multijet triggers is shown in Figure 3.3.

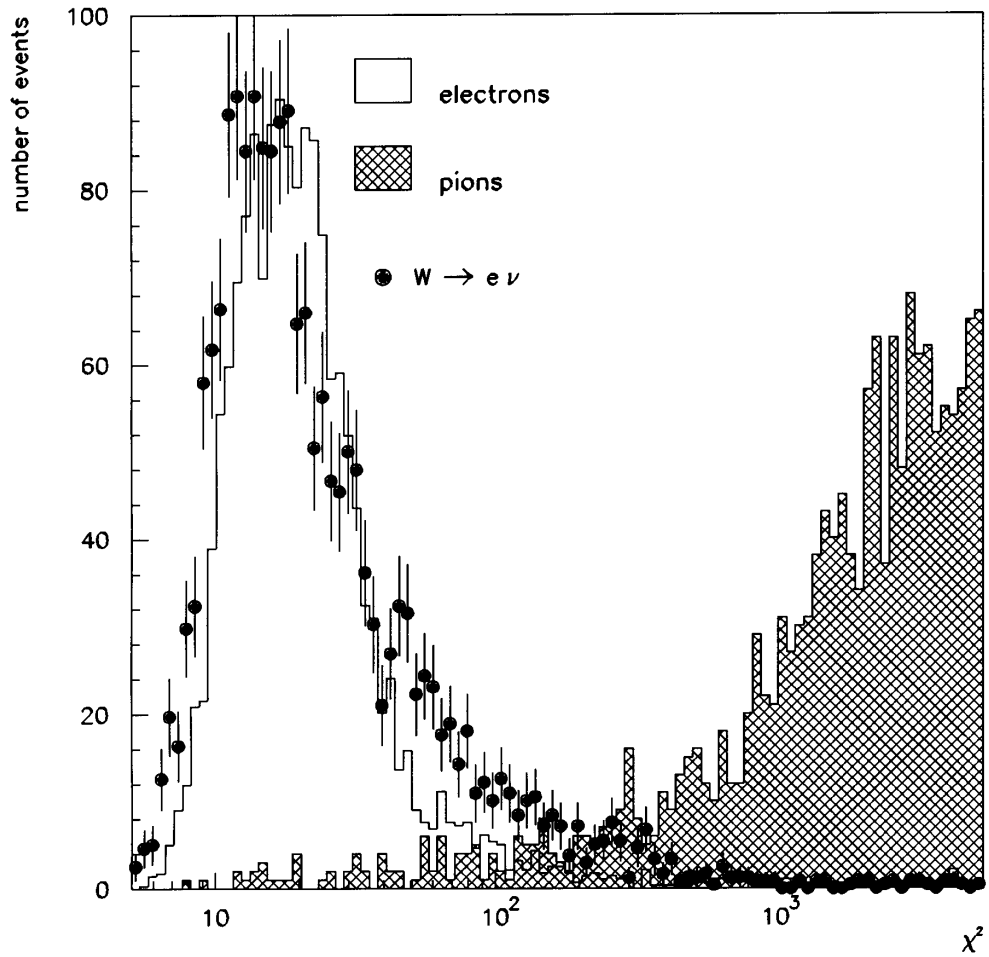

Figure 3.2: H-Matrix $\chi^2_{\rm hm}$ distribution for test beam electrons (unshaded), test beam pions (shaded), and electrons from an early $W \to e\nu$ sample (dots). The error bars are statistical only.

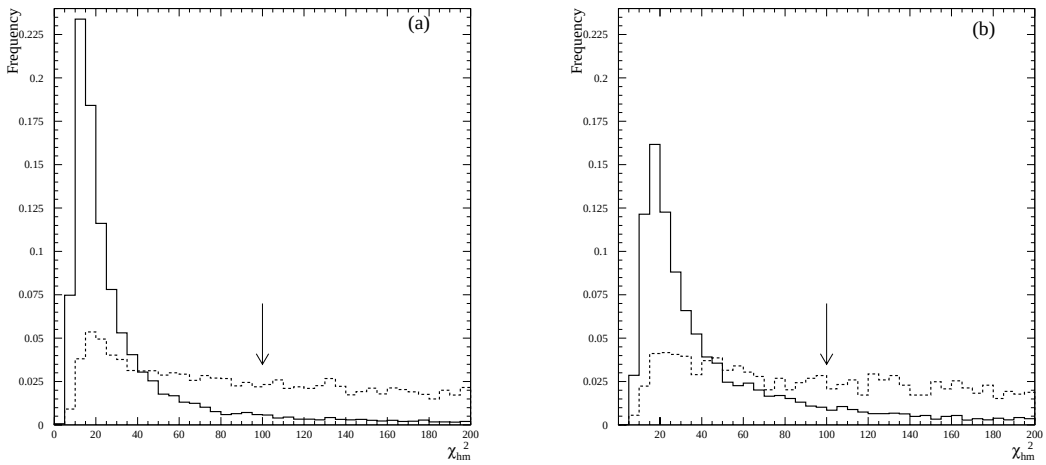

Figure 3.3: H-matrix $\chi^2_{\rm hm}$ distribution for probe electron candidates from $Z \to ee$ data (solid) and electron candidates from multijet triggered data (dashed), for (a) central electrons and (b) forward electrons. No other cuts are applied to the candidate electrons. The relative normalization is arbitrary.

3.2.3 Shower Isolation

Electrons originating from the decays of W and Z bosons are isolated: very little activity surrounds the calorimeter cluster, since the electron was not produced in association with other particles. In contrast, the production of π^0 and η particles (which decay to two photons and thus create an electromagnetic shower), or the production of electrons from heavy quark leptonic decays, that are isolated from other hadrons is relatively rare[5]. Hence an isolation requirement does not identify genuine electrons, but rather selects a particular type of physics process: in this case, requiring isolated electrons preferentially selects W and Z boson events, while rejecting other sources of real electrons or photons.

Since electromagnetic showers are usually contained in a cone of radius $R =$

[5]It is on the order of 10^{-3}–10^{-4}.

0.2, an isolation fraction variable is defined as:

$$f_{iso} = \frac{E_{total}(0.4) - E_{EM}(0.2)}{E_{EM}(0.2)} \ , \tag{3.3}$$

where $E_{total}(0.4)$ is the total energy in an isolation cone of radius $R = 0.4$, and $E_{EM}(0.2)$ is the electromagnetic energy in a core cone of radius $R = 0.2$. Distributions of the isolation variable, $f_{\rm iso}$, are shown in Figure 3.4 for probe electrons from $Z \to ee$ decays and "electrons" from multijet triggers. For this analysis, a requirement of $f_{\rm iso} < 0.15$ is imposed on all electron candidates.

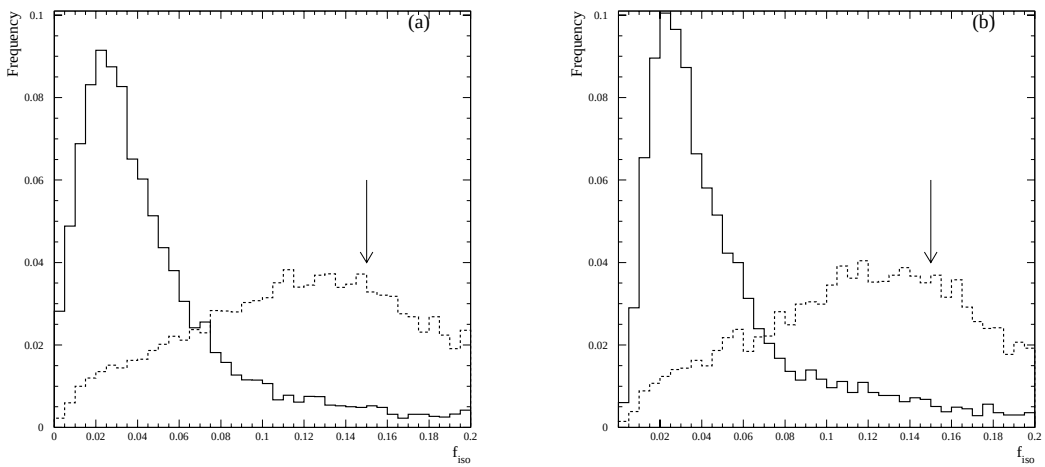

Figure 3.4: Isolation distribution $f_{\rm iso}$ for probe electron candidates from $Z \to ee$ data (solid) and electron candidates from multijet triggered data (dashed), for (a) central electrons and (b) forward electrons. No other cuts are applied to the candidate electrons, and the relative normalization is arbitrary.

3.2.4 Track Matching

Electrons are defined by DØRECO as electromagnetic clusters with a track present in a road defined by the vertex position and the cluster centroid. Since the road

definitions are quite loose, background contamination due to accidental overlaps (such as the presence of π^0 or η and additional nearby soft charged hadrons) can be substantial. The tracks of genuine electrons are expected to be well aligned with the calorimeter cluster, hence background rejection can be achieved if tighter cluster–track matching is performed.

To quantify the quality of the cluster–track matching, the track is extrapolated into the EM3 layer of the calorimeter, and the distance between the projection and the cluster centroid is determined in both longitudinal (θ) and transverse (ϕ) directions. In order to place any significance on this spatial mismatch, one must understand the resolutions in track projection–cluster matching. For electrons in the central calorimeter, this resolution is 1.7 cm in the longitudinal direction and 0.3 cm in the transverse direction. For electrons in the end calorimeter, these resolutions are 0.8 cm and 0.3 cm respectively [49, p. 80]. The track match significance in the central calorimeter is then defined as:

$$S_{trk}^{CC} = \sqrt{\left(\frac{\rho\Delta\phi}{\sigma_{\rho\phi}}\right)^2 + \left(\frac{\Delta z}{\sigma_z}\right)^2}\,, \tag{3.4}$$

where $\rho\Delta\phi$ is the transverse spatial mismatch, Δz is the longitudinal spatial mismatch, and $\sigma_{\rho\phi}$ and σ_z the corresponding resolutions. Similarly, the track match significance in the end calorimeter is defined as:

$$S_{trk}^{EC} = \sqrt{\left(\frac{\rho\Delta\phi}{\sigma_{\rho\phi}}\right)^2 + \left(\frac{\Delta\rho}{\sigma_\rho}\right)^2}\,, \tag{3.5}$$

where $\rho\Delta\phi$ is the transverse spatial mismatch, $\Delta\rho$ is the longitudinal spatial mismatch, and $\sigma_{\rho\phi}$ and σ_ρ the corresponding resolutions. To clarify the definition of track match significance further, an illustration of its physical meaning is shown in Figure 3.5: track projections onto the surface of the EM3 layer which fall within the indicated significance ellipse are considered good matches.

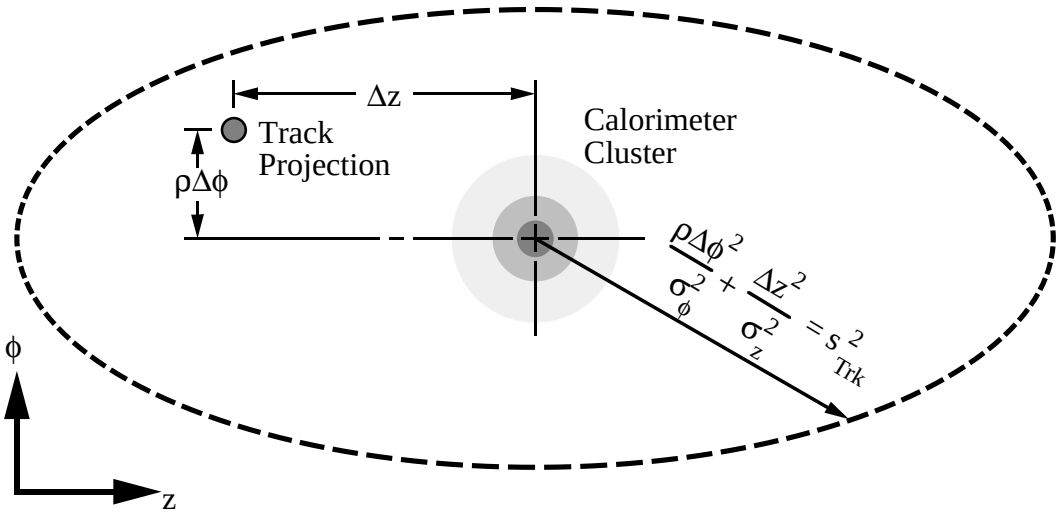

Figure 3.5: Definition of track match significance in terms of the cluster centroid in EM3 and the projection of the track to the radius of EM3 [49, p. 81].

Distributions of the track match significance variable, S_{trk}, are shown in Figure 3.6 for electrons from $Z \to ee$ decays and electrons from multijet triggers. For this analysis, the track match significance requirement is $S_{\mathrm{trk}} < 5$ for central electrons and $S_{\mathrm{trk}} < 10$ for forward electrons. The looser cut on forward electrons is due to large non-gaussian tails in the EC resolutions.

3.3 Neutrino Identification

Neutrinos, which have only weak interactions, do not interact in the detector, and thus create apparent momentum imbalance in an event. For each $W \to e\nu$ candidate event, we measure the momentum imbalance in the plane transverse to the beam direction ($\not\!\!E_T$), and attribute this to the neutrino.

The calculation of $\not\!\!E_T$ is based upon energy deposits at the calorimeter cell level. A missing transverse energy vector, $\vec{\not\!\!E}_T$, is defined so that it cancels exactly

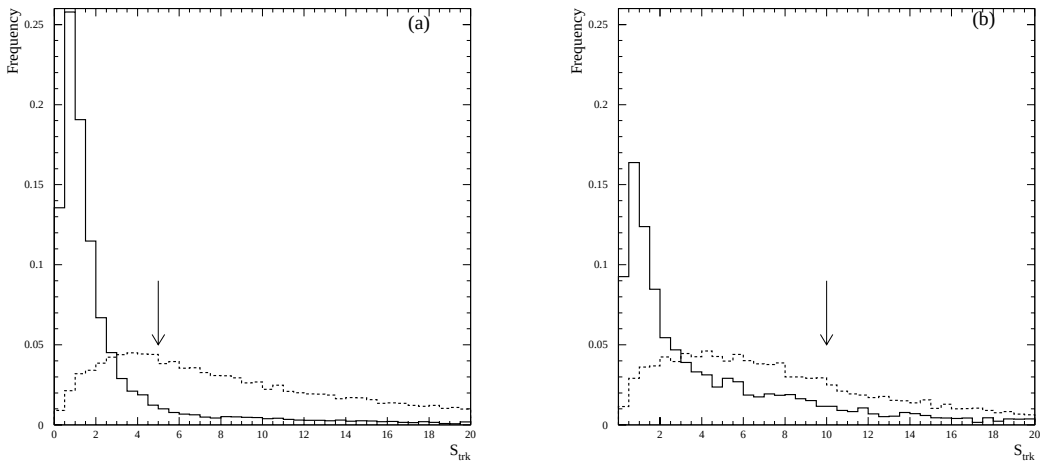

Figure 3.6: Track match significance $S_{\rm trk}$ distribution for electron candidates from $Z \to ee$ data (solid) and electron candidates from multijet triggered data (dashed), for (a) central electrons and (b) forward electrons.

the total transverse energy vector in the calorimeter:

$$\not{E}_x = -\sum_{\text{all cells}} E_x(\text{cell}) \qquad \not{E}_y = -\sum_{\text{all cells}} E_y(\text{cell}) \ , \tag{3.6}$$

and

$$\vec{\not{E}}_T = \begin{pmatrix} \not{E}_x \\ \not{E}_y \end{pmatrix} \ . \tag{3.7}$$

The missing transverse energy, $\not{E}_T$, is just the magnitude of this vector:

$$\not{E}_T = |\vec{\not{E}}_T| = \sqrt{\not{E}_x^{\ 2} + \not{E}_y^{\ 2}} \ , \tag{3.8}$$

While in principle there should be no net E_T in the underlying event, effects of finite resolution can cause the measured vector E_T from the underlying event to be non zero, and the underlying event therefore contributes to the $\not{E}_T$. The neutrino E_T corresponds to the negative of the vector sum of the electron E_T, the recoil E_T, and the E_T of the underlying event.

In this analysis, energy corrections (discussed in Chapter 4) are applied to the signal electron(s) in $W \to e\nu$ and $Z \to ee$ events. These corrections are therefore propagated into the calculation of $\not\!\!E_T$. No corrections are applied to jets or muons found in the events. Since the calorimeter response to electrons and photons is different from the response to hadrons, this results in jet energy measurements which are low by about 25%. This leads to a small degradation in the $\not\!\!E_T$ resolution, but this is acceptable as long as the same prescription is followed in modeling the $\not\!\!E_T$ resolution. As discussed in Chapter 4, the fast Monte Carlo used in this analysis models the hadronic response and the $\not\!\!E_T$ resolution in a manner consistent with the data.

3.4 Electron Vertex Finding

The electron vertex finding algorithm [49, sec. 4.8.1] relies on calorimeter cluster and associated track matching, instead of tracking roads. For a given electromagnetic cluster in the calorimeter, a search is performed for the best matching track, regardless of whether this track was contained in the tracking road. This search is performed on all CDC and FDC tracks, and track match significance is computed exactly as described in Equation 3.4 and Equation 3.5. This track can then be used to determine the origin of the electron by extrapolating the line connecting the calorimeter cluster's center-of-gravity and the track's center-of-gravity to the beamline. Hence, the z-coordinate of the interaction vertex, denoted as z_v, is given by:

$$z_v = z_0^{trk} - \left(\frac{z_0^{cal} - z_0^{trk}}{\rho_0^{cal} - \rho_0^{trk}} \right) \rho_0^{trk} \ , \tag{3.9}$$

where $(z_0^{trk}, \rho_0^{trk})$ and $(z_0^{cal}, \rho_0^{cal})$ are the centers-of-gravity of the drift chamber track and the calorimeter cluster respectively. This extrapolation is illustrated in Figure 3.7 for added clarity. The best matching track must satisfy the significance criteria mentioned in Section 3.2.4, namely $S_{\mathrm{trk}} < 5$ for central electrons and $S_{\mathrm{trk}} < 10$ for forward electrons.

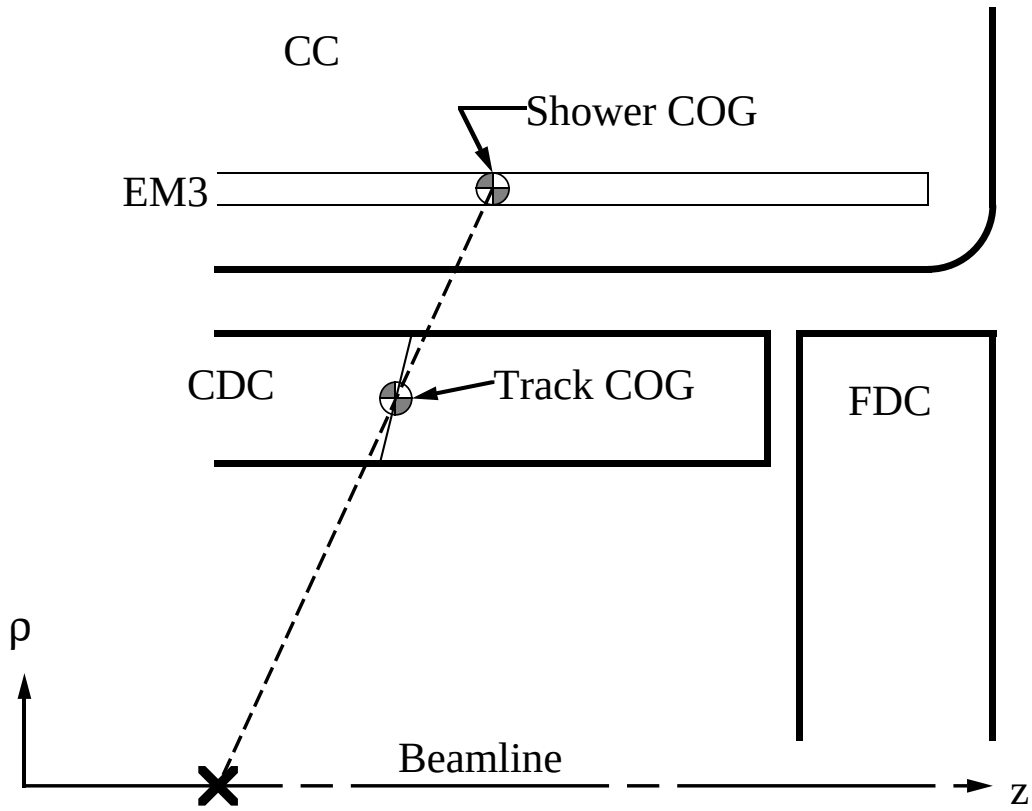

Figure 3.7: Cluster vertex determination by electron–track projection [49, p. 84].

The vertex resolution achieved by this technique can be measured from $Z \to ee$ candidate events: it is proportional to the difference between the z-intercepts of the two electrons. The single electron vertex resolution, σ_z, is given by:

$$\sigma_z = \frac{1}{\sqrt{2}}\sigma(z_1 - z_2) \tag{3.10}$$

if the z-intercepts z_1 and z_2 of the two electrons are uncorrelated. The distribution of $(z_1 - z_2)$ is shown in Figure 3.8, which indicates that $\sigma_z = 1.9$ cm.

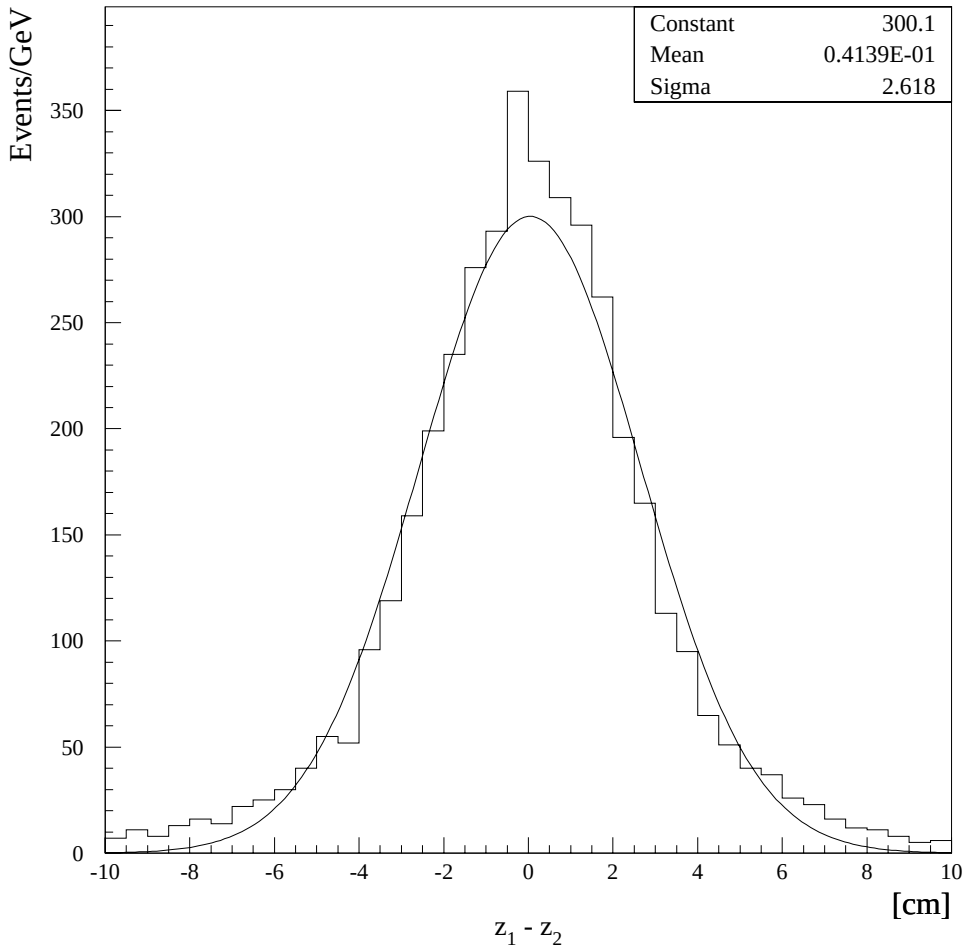

Figure 3.8: Distribution of $(z_1 - z_2)$ in $Z \to ee$ events (cm). Also shown are the parameters for the fit to a gaussian distribution.

In $Z \to ee$ events there might be more than one electron with a matching track. The single event vertex position is determined by the most central electron

which has a matching track. The most central electron is the one with smallest $|\eta_D|$, where detector eta, η_D, is the pseudorapidity of the electron calculated using the electron position in the calorimeter and the vertex at the center of the detector, $z = 0$ cm. In $W \to e\nu$ events, the one electron's matching track determines the event vertex.

The performance of the electron vertex finding algorithm can be compared to the standard algorithm in DØRECO, where all reconstructed tracks are used, and the primary vertex is defined as the vertex with the largest track multiplicity. In fact, with the knowledge of the single electron vertex resolution, it is possible to measure how often DØRECO misreconstructs the primary vertex position. The standard vertex is considered to be mismeasured if it is at least 5 standard deviations from the single electron vertex (in this case, this distance amounts to 10 cm). As is shown in Figure 3.9a, the rate at which this occurs in $Z \to ee$ events grows as a function of instantaneous luminosity. For the inclusive $Z \to ee$ sample, about 13% of the events have mismeasured primary vertices. In contrast, the rate at which $(z_1 - z_2) > 10$ cm is much flatter as a function of instantaneous luminosity, indicating that the electron vertex algorithm is quite robust. This situation would have been quite different if the busy environment in high luminosity events was affecting the electron vertex algorithm via random overlaps and/or reconstruction inefficiencies.

In addition, the invariant mass spectrum of $Z \to ee$ candidate events is shown in Figure 3.9b for both vertexing algorithms. It is clear that the electron vertex algorithm increases the number of events in the central peak region. The broader distribution for the standard vertex algorithm is caused by misreconstructed interaction vertices. While the electron energy is measured in the calorimeter, the

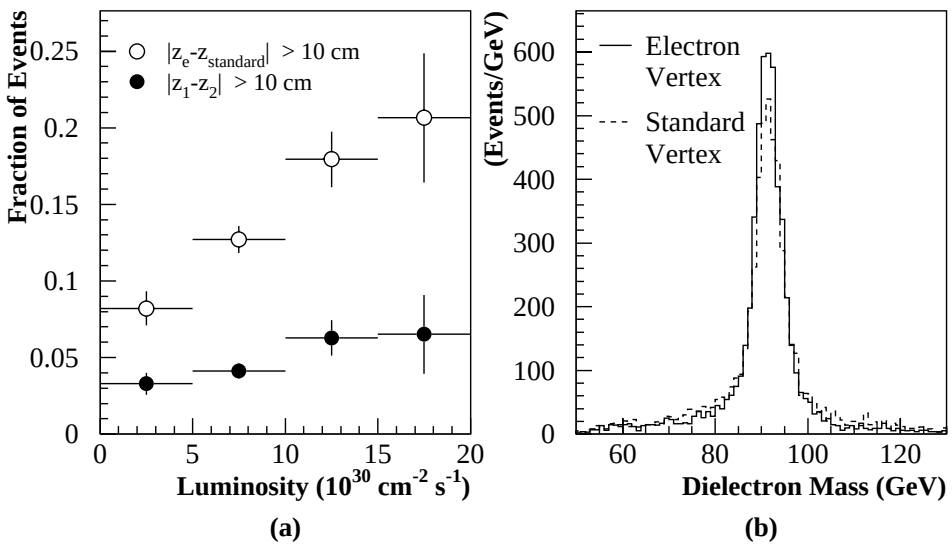

Figure 3.9: (a) Frequency at which the standard vertex is mismeasured as a function of instantaneous luminosity. The standard vertex is considered to be mismeasured if it is found more than 10 cm away from the electron vertex. The rate at which the electron z-intercepts differ by more than 10 cm is also shown. (b) Invariant mass distribution for $Z \to ee$ events using the two vertexing algorithms [49, p. 86].

electron's $\cos\theta$ is obtained from the line connecting the vertex and the calorimeter cluster. A mismeasured vertex leads to a mismeasurement of $\cos\theta$ and thus of the invariant mass of the two electrons.

3.5 Offline Electron Selection

Before proceeding to the selection of W and Z boson events, a description of the electron selection itself is given below. Two classifications are used to describe

the signal electrons: a loose selection which identifies "loose" electrons and a tight selection which identifies "tight" electrons. The tight electrons form a subset of the loose ones. In order to ensure a well understood detector response, the fiducial region is selected such that non-instrumented or poorly instrumented regions of the detector are eliminated. These regions include the inter-cryostat region between the CC and the EC calorimeters, the very forward regions where the segmentation of the EM calorimeter decreases, and the boundaries between the electromagnetic central calorimeter modules. Tight and loose electrons are defined as follows:

- <u>Loose electron</u>
  - EM cluster in the good fiducial region;
    - Central Calorimeter: $|\eta_D| < 1.1$ and $0.05 < \Delta\phi_{crk} < 0.95$;
    - Endcap Calorimeter: $1.5 < |\eta_D| < 2.5$.
  - H-matrix $\chi^2_{\rm hm} < 100$;
  - EM fraction $f_{\rm em} > 0.95$;
  - Isolation fraction $f_{\rm iso} < 0.15$;
- <u>Tight electron</u>
  - Loose electron
  - A matching central detector track with significance $S_{\rm trk} < 5(10)$ in the CC(EC).

Loose and tight electrons share all calorimeter-based electron identification criteria. However, loose electrons are not required to have a matching track. This

class of electrons is only used in $Z \to ee$ event selection in order to increase the statistics of the Z sample. The variable $\Delta\phi_{crk}$ is defined as the ϕ-angle distance between the electron cluster and the edge of any CC calorimeter module, (the boundaries between these modules are sometimes referred to as "cracks"), in units of the angle subtended by the module:

$$\Delta\phi_{crk} = \mathrm{MOD}(\frac{32}{2\pi}\phi_{cluster}, 1) \ . \tag{3.11}$$

The fiducial region represents a $\sim 25\%$ loss in acceptance of the full calorimeter solid angle.

3.6 $W \to e\nu$ Selection

Candidate $W \to e\nu$ events are selected through their signature of an isolated, high-p_T electron and a high-p_T neutrino. The selection occurs in two stages: trigger and offline. Trigger requirements are rather loose, and offline requirements are imposed to optimize the signal to background ratio.

3.6.1 $W \to e\nu$ Trigger Requirements

The $W \to e\nu$ data sample was collected with the EM1_EISTRKCC_MS trigger. This trigger was configured in two different ways during Run 1b, the change occurring with the introduction of the Calorimeter Level-1.5 trigger halfway through the run (trigger configuration menu version 10.0). The EM1_EISTRKCC_MS trigger had the following conditions:

- Level-Ø trigger (hardware)

- The universal Level-Ø minimum bias requirement was imposed for about the first half of Run 1b: this consisted of the detection of an inelastic collision with simultaneous hits in the north and south LØ counters, as well as a fast z determination with $|z| < 96.875$ cm;
- The requirement was removed for trigger versions ≥ 10.0. It operated in a *mark and pass* mode, where the Level-Ø requirement was checked but the result was not used in the trigger decision. However, this result was recorded so that the cut may be studied and imposed offline (this issue will be discussed in Chapter 5).

- Level-1 trigger (hardware)
  - $E_T^{em} > 12.0$ *or* 10.0 GeV. The threshold changed with trigger version 10.0;
  - GoodCal Main Ring beam veto: see discussion below.

- Level-1.5 trigger (hardware)
  - $E_T^{em} > 15.0$ GeV (this cut was introduced with trigger version 10.0);
  - $f_{\mathrm{em}} > 0.85$ (this cut was introduced with trigger version 10.1).

- Level-2 filter (software)
  - $E_T > 20.0$ GeV;
  - Loose shower shape (ele) and isolation fraction (iso) cuts ($eis \equiv ele \cdot iso$);
  - $\not{E}_T > 15.0$ GeV.

As mentioned earlier, the Main Ring component of the Tevatron accelerator system passes through the outer part of the hadronic calorimeter. Beam losses from the Main Ring can create significant energy deposits in the calorimeter, resulting in large false $\not\!\!E_T$. The largest losses occur when beam is being injected into the Main Ring. Events occurring within a 400 ms window (called the `MRBS_LOSS` window) of injection are rejected by the GoodCal requirement, leading to only a small loss of data. Large beam losses can also occur when particles in the Main Ring pass through the DØ detector. Events within a 1.6 μs window (called the `MICRO_BLANK` window) around these time periods are rejected offline, resulting in an approximately 8% loss of data. The GoodBeam veto rejects events occurring in the `MRBS_LOSS` or `MICRO_BLANK` time windows.

3.6.2 $W \to e\nu$ Offline Selection

The final selection of $W \to e\nu$ events is performed from all Run 1b data, after runs with known problems are removed [50]. The following cuts are used:

- Event must pass EM1_EISTRKCC_MS trigger;
- Event must pass the Level-Ø minimum bias requirement (see Section 3.6.1);
- Event must pass the GoodBeam veto condition.
- Event must have one tight triggered electron with $E_T > 25$ GeV;
  - the vertex for the event is defined by this electron. The z-coordinate of the vertex must have $|z| < 97$ cm in order to match the Level-Ø requirement;
- Event must have corrected $\not\!\!E_T > 25$ GeV;

- Events containing a second loose electron with $E_T > 25$ GeV are excluded (to minimize the $Z \to ee$ background with mismeasured $\not{E}_T$).

At the highest luminosities, the $W \to e\nu$ trigger was prescaled by a factor of two to reduce the trigger rate to an acceptable level. It was not necessary to prescale the $Z \to ee$ trigger. To ensure that luminosity-dependent effects cancel in the ratio of the cross sections, we discard runs with a $W \to e\nu$ prescale or with no $W \to e\nu$ trigger.

A total of 67078 events passes the $W \to e\nu$ requirements, of which 46792 events have their electron in the CC, with 20286 in the EC. The topological breakdown into central (CC) or forward (EC) events is summarized in Table 3.1. Figure 3.10 shows the transverse mass distribution of the candidates.

Table 3.1: Summary of the $W \to e\nu$ signal event sample and topological breakdown.

$W \to e\nu$ Signal Events	
CC	46792
EC	20286
Total	67078

3.7 $Z \to ee$ Event Selection

Candidate $Z \to ee$ events are selected using the signature of two isolated high-p_T electrons. The actual selection proceeds along similar lines to the W case, namely in two stages: trigger and offline.

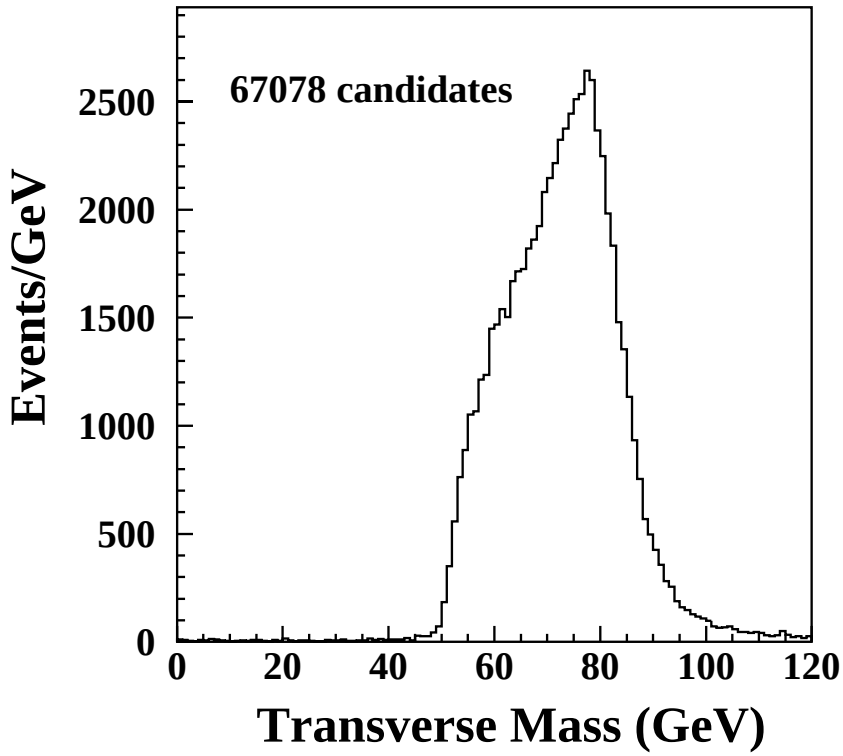

Figure 3.10: The transverse mass distribution of the final $W \to e\nu$ candidate event sample in GeV.

3.7.1 $Z \to ee$ Trigger Requirements

The $Z \to ee$ data sample was collected with the EM2_EIS2_HI trigger. This trigger was also configured in two different ways during Run 1b, the change occurring with trigger version 10.0. The EM2_EIS2_HI trigger had the following conditions:

- Level-Ø trigger
  - The universal Level-Ø minimum bias requirement was imposed.
- Level-1 trigger
  - 2 EM objects with $E_T^{em} > 7.0$ GeV;
  - MaxLive beam veto: events occurring in the `MRBS_LOSS` *and* `MICRO_BLANK` periods simultaneously, were rejected.
- Level-1.5 trigger
  - 2 EM objects with $E_T^{em} > 12.0$ GeV (trigger version ≥ 10.0);
  - 2 EM objects with $f_{\mathrm{em}} > 0.85$ (trigger version ≥ 10.1).
- Level-2 filter
  - 2 EM objects with $E_T > 20.0$ GeV;
  - Loose shower shape and isolation fraction cut (*eis*) on both objects.

3.7.2 $Z \to ee$ Offline Selection

The final selection of $Z \to ee$ events is performed from all Run 1b data after runs with known problems are removed [50]. The following cuts are used:

- Event must pass the EM2_EIS2_HI trigger;
- Event must pass the GoodBeam veto condition.
- Two loose triggered electrons with $E_T > 25$ GeV each, one of which must be tight;

- the vertex for the event is defined by the tight electron. In case both electrons are tight, the most central (smallest $|\eta_D|$) is used to define the vertex. The z-coordinate of the vertex must have $|z| < 96.875$ cm in order to match the Level-Ø requirement;

- Invariant mass of the dielectron pair: $75 < M_{ee} < 105$ GeV.

Runs in which the W trigger was prescaled or in which there was no $W \to e\nu$ trigger are discarded, in order to have exact cancelation of luminosity systematics in the ratio $\mathcal{R}$ of cross sections. For the same reason, the same Main Ring veto is imposed offline for both $W \to e\nu$ and $Z \to ee$ selections.

A total of 5397 events passes the $Z \to ee$ selection criteria, of which 2737 have both electrons in the CC calorimeter, 2142 have one in the CC and one in the EC, and 518 have both electrons in the EC calorimeter. The topological breakdown into central-central (CC-CC), central-forward (CC-EC), and forward-forward (EC-EC) events is summarized in Table 3.2. Figure 3.11 shows the invariant mass distribution of the final $Z \to ee$ candidates.

Table 3.2: Summary of the $Z \to ee$ signal event sample and topological breakdown.

$Z \to ee$ Signal Events	
CC–CC	2737
CC–EC	2142
EC–EC	518
Total	5397

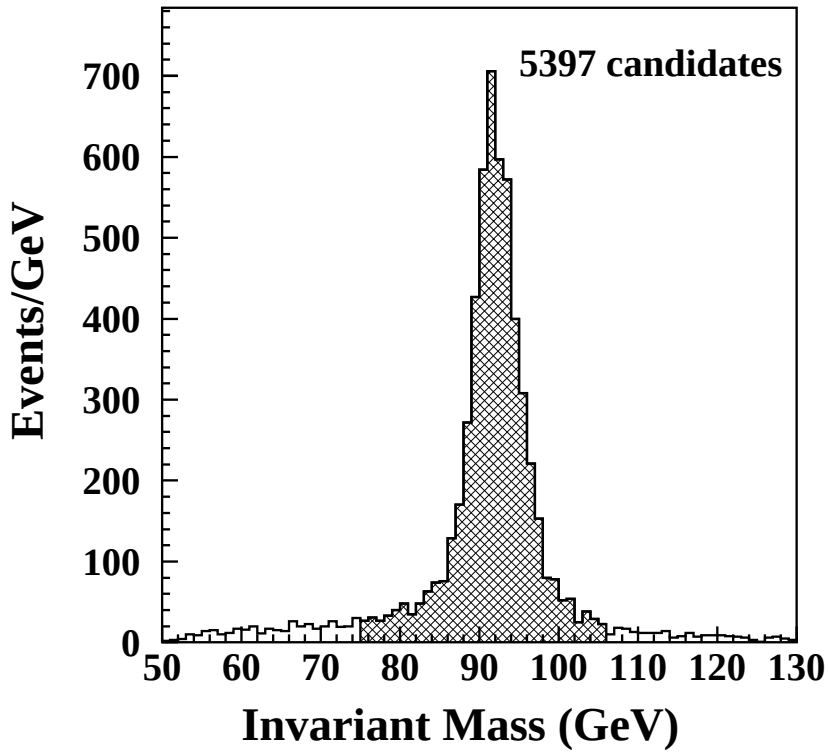

Figure 3.11: The invariant mass distribution of the final $Z \rightarrow ee$ candidate event sample in GeV. The shaded region represents the dielectron invariant mass requirement.

Chapter 4

Acceptance

In order to measure the cross sections $\sigma(p\overline{p} \rightarrow W + X) \cdot B(W \rightarrow e\nu)$ and $\sigma(p\overline{p} \rightarrow Z + X) \cdot B(Z \rightarrow ee)$, one needs to know what fraction of the $W \rightarrow e\nu$ and $Z \rightarrow ee$ events produced end up being observed. Electrons might escape detection if they enter an uninstrumented region of the detector. Also, electrons which do not satisfy the fiducial or kinematic requirements are not used in the cross section measurements. We define the detector acceptance as the fraction of $W \rightarrow e\nu$ or $Z \rightarrow ee$ events which pass the fiducial and kinematic requirements. Since one has no way of counting the number of events which are undetected, the geometric and kinematic acceptances of the selection criteria are calculated using a fast Monte Carlo simulation. This chapter describes the Monte Carlo used, gives the acceptance results, and discusses Drell-Yan and next-to-leading-order (NLO) corrections.

4.1 The CMS Monte Carlo

The Monte Carlo used in this analysis, called CMS [51, 14] (after Columbia–Michigan State, where the main authors worked), was originally developed for

the measurement of the W boson mass at DØ [52]. This section gives a brief description of CMS. More detailed descriptions can be found in Refs. [51, 14]. The detector simulation was re-tuned for this analysis, because the W mass analysis used only electrons with $|\eta_D| < 1.1$, and imposed different fiducial cuts at the azimuthal boundaries of the central calorimeter modules. In addition, the W mass analysis was restricted to events with W and Z boson $p_T < 15$ GeV, while this is not the case for the present analysis. The CMS Monte Carlo generates $W \to e\nu$ and $Z \to ee$ events in two steps. Initially, the W or Z boson, the recoil system, and the underlying event are generated with appropriate kinematic properties, and the boson is forced to decay in the electron channel. A second stage then models the response of the detector and the effect of the geometric and kinematic selection criteria.

4.1.1 Event Generation

$W \to e\nu$ and $Z \to ee$ event generation consists of two parts: production and decay of W and Z bosons. The physics governing these processes is briefly discussed in Chapter 1.

W and Z Boson Production

Vector boson production is ideally modeled with a fully differential cross section:

$$\frac{d^5\sigma}{dm dp_T dy d\phi d\epsilon} \tag{4.1}$$

where m, p_T, y, ϕ, and, ϵ are the vector boson mass, transverse momentum, rapidity, azimuthal angle, and polarization, respectively. In the CMS Monte

Carlo, this differential cross section is factorized into four separate pieces:

$$\frac{d^5\sigma}{dm dp_T dy d\phi d\epsilon} = \frac{d\sigma}{dm} \cdot \frac{d^2\sigma}{dp_T dy} \cdot \frac{d\sigma}{d\phi} \cdot \frac{d\sigma}{d\epsilon} \ . \tag{4.2}$$

This factorization is not strictly correct, since correlations exist between the mass, transverse momentum, rapidity, and polarization terms. However, these correlations have a negligible effect on the acceptance. As a cross check, the acceptances are also calculated using events generated with the PYTHIA [53] event generator, and the results are consistent with those from CMS.

Azimuthal and Polarization Distributions

The ϕ distribution is trivial: $\frac{d\sigma}{d\phi}$ is uniform, hence a value is chosen at random in the interval $[0, 2\pi]$. The polarization of W and Z bosons is discussed in Section 1.4.4. In the generation of Z bosons, the polarization vector is chosen randomly to lie either in the direction of the incoming proton, or opposite to it. For the W boson case, the charge defines its polarization. For a W^+, if at least one valence quark is involved in the W boson production, the polarization vector is opposite the proton direction. For the fraction of events ($f_{ss} \approx 20\%$) in which the quarks involved in the W boson production both originate from the sea, one half of these events have their polarization reversed.

Mass Distribution

The mass distribution of the boson is generated according to a relativistic Breit-Wigner convoluted with the CTEQ4M [54] parton distribution functions, and has the form of Equation 1.44, as discussed in Section 1.4.2. This is done by generating $W \to e\nu$ events in the mass range 40–120 GeV and $Z \to ee$ events in

the mass range 50–130 GeV using the PYTHIA generator. The resulting invariant mass distributions, shown in Fig. 4.1, are then used as input for CMS: for each event, a mass is picked at random from one of these histograms. The mass

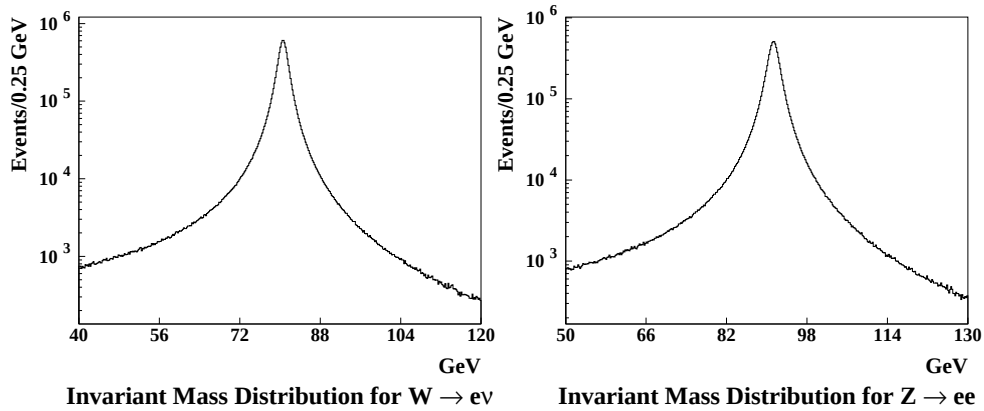

Figure 4.1: Invariant mass distributions for $W \to e\nu$ (left) and $Z \to ee$ (right) generated using PYTHIA. For each generated event, the CMS Monte Carlo picks a mass randomly from these distributions.

distributions show a clear resonance at the W or Z boson mass. The parton distribution functions are decreasing functions of parton momentum. As a result, the convolution of the partonic cross sections with the parton distribution functions favors the production of vector bosons with a lower mass. This effect can also be seen in the figure. For the Z boson, events are generated according to the Z-boson line shape. Dielectron events which arise from virtual photons γ^* or from interference between the Z and the γ^* propagators are not included in the generation, since we want to report the cross section due only to the Z boson. These *Drell-Yan* processes therefore need to be subtracted from the data, as discussed in Chapter 6. The generator produces bosons only over a finite mass range, and a small correction in the acceptance is included to account for

this.

Transverse Momentum and Rapidity Distributions

The transverse momentum and rapidity distributions of the boson are generated by computing the differential cross section, $d^2\sigma/dp_T^2dy$, using LEGACY, a program provided by Ladinsky and Yuan [12], as discussed in Section 1.4.3. In the high-p_T regime ($p_T > 50$ GeV), a second order perturbative calculation by Arnold and Reno is used [11]. For the low-p_T regime ($p_T < 50$ GeV), the resummed calculation of Ladinsky and Yuan [12] is used. The resummed double differential cross section for vector boson production is given by Equation 1.45, with S_{NP} given by Equation 1.47. For this analysis, LEGACY generates transverse momentum *vs.* rapidity distributions, also called p_T-y grids, using the CTEQ4M parton distribution functions for consistency with the boson mass generation. Separate p_T-y grids are used for positively and negatively polarized W bosons. For the Z boson, the polarization is not important, and a single grid is used. Figure 4.2 shows the vector boson transverse momentum distribution for $W \to e\nu$ and $Z \to ee$ candidate events, and for the Monte Carlo (after smearing for detector response).

W and Z Boson Decay

The W and Z bosons are forced to decay in the electron channel. The angular distribution of the decay leptons is discussed in Section 1.5. CMS treats the leptons as massless, performs the decay in the boson center-of-mass frame, and then boosts the leptons to the lab frame according to the boson momentum. Figure 4.3 shows the angular (θ) distribution for electrons from W and Z boson

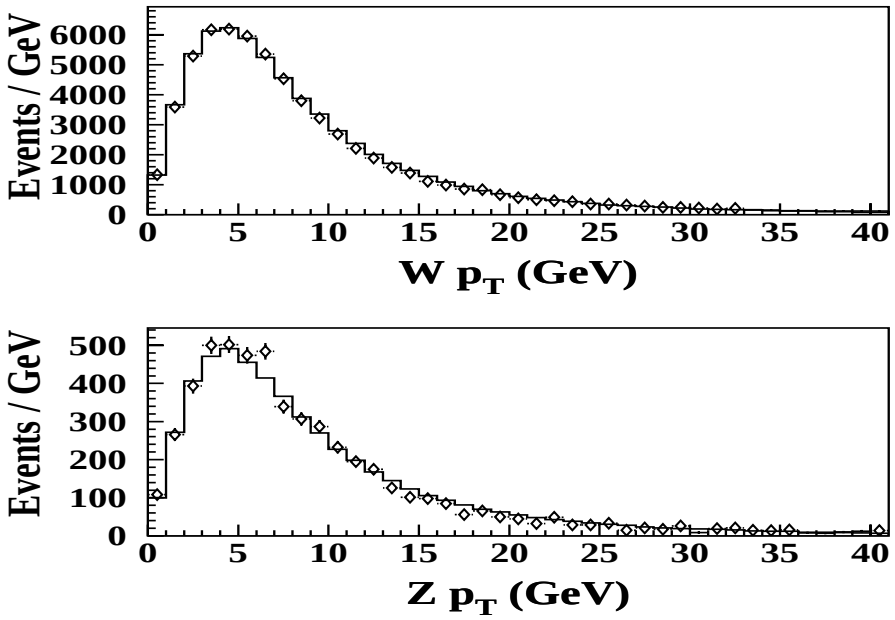

Figure 4.2: The transverse momentum distribution for W and Z bosons. The top plot shows the P_T^W distribution for $W \to e\nu$ candidates (diamonds) and for CMS (histogram). The bottom plot is the corresponding distribution for the Z boson. The error bars are the statistical uncertainty of the data.

decays for the $W \to e\nu$ and $Z \to ee$ candidate events and for the Monte Carlo. The boson decays include the effects of lowest-order internal bremsstrahlung, where a photon is radiated from a final state electron, using the Berends-Kleiss calculation [55]. Approximately 31% of the W boson events and 66% of the Z boson events have a photon with an energy above 50 MeV in the final state. In the simulation, the energies of the photon and its associated electron are combined if their separation, $\sqrt{\Delta\eta^2 + \Delta\phi^2}$, is less than 0.3.

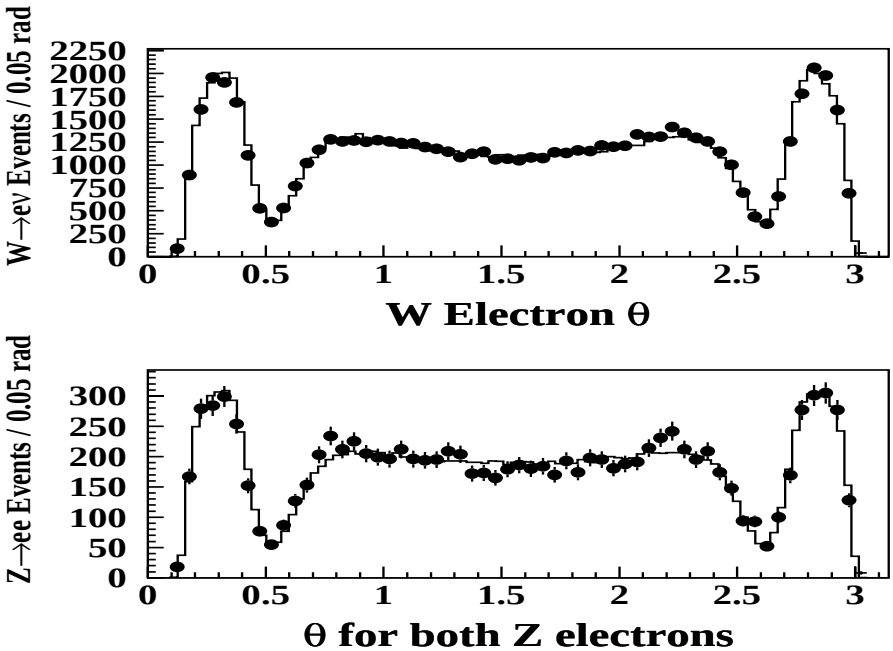

Figure 4.3: Top: the electron θ distribution for $W \to e\nu$ data and for Monte Carlo. The dots are the data and the histogram is CMS. The error bars are the statistical uncertainty in the data. Bottom: corresponding distributions for *both* electrons in $Z \to ee$ events.

4.1.2 Detector Response

After $W \to e\nu$ and $Z \to ee$ events are generated with appropriate kinematic properties, CMS models the detector response. The z position of the event vertex is smeared to match the distribution of the data. Electron energies and angles are smeared according to measured resolutions, and are corrected for offsets in energy scale due to contamination from particles from the underlying event or the recoil in the calorimeter towers containing the electron signal. The recoil momentum is also smeared by the measured resolution, and corrected for any

losses of particles to the same calorimeter towers as the electron, and for effects of underlying event.

Event Vertex

The primary vertex distribution is generated as a gaussian with a width of 27 cm and a mean position of -0.6 cm, to match the observed distribution. Figure 4.4 shows the z position of the event vertex for $Z \to ee$ candidate events and for the CMS Monte Carlo.

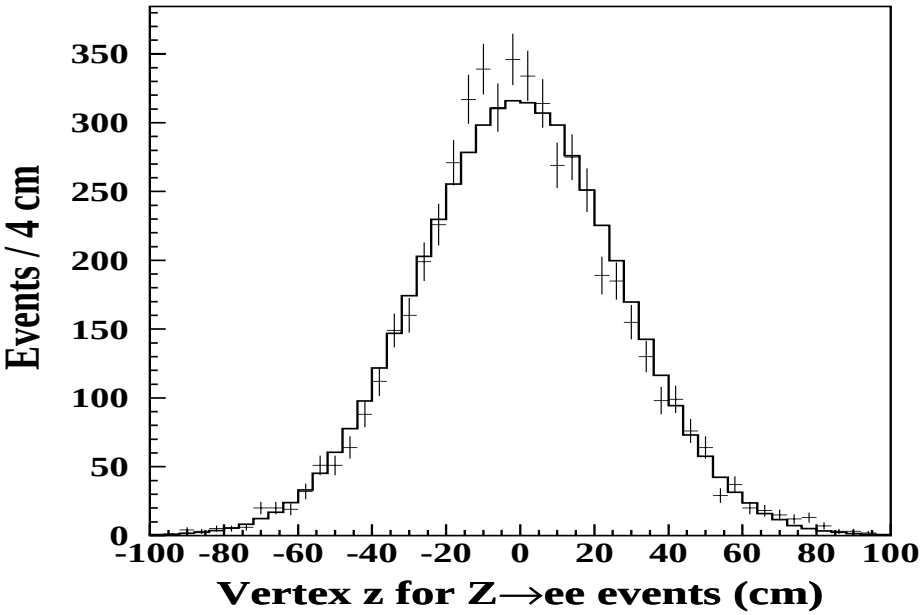

Figure 4.4: The z position of the event vertex for $Z \to ee$ candidates (crosses with statistical uncertainty error bars) and for CMS (histogram).

Electromagnetic Energy Scale

The electron energy scale is adjusted to reproduce the known mass [43] of the Z boson. The energy scale in the CC is obtained by plotting the invariant dielectron mass of CC-CC $Z \to ee$ events and adjusting the scale until the Monte Carlo distribution agrees with the data. Once the CC scale is known, the EC scale is obtained by plotting the invariant dielectron mass of CC-EC events and applying the same procedure. Figure 6.3 shows the invariant mass distribution for data and Monte Carlo $Z \to ee$ events in all three topologies (CC-CC, CC-EC, and EC-EC). The uncertainty in energy scale is 0.1% for the CC, and 1.6% for the EC. The large uncertainty in the EC energy scale is due to a rapidity dependent miscalibration of the EC calorimeter. A correction for this is applied in each sample which contains EC electrons (CC-EC $Z \to ee$ events, EC-EC $Z \to ee$ events, and EC $W \to e\nu$ events). One fits the corresponding invariant or transverse mass distributions to the data, determines which EC energy scale results in the best fit, and the uncertainty is taken as the size of the correction to the energy scale.

Electromagnetic Energy Resolution

The electron energy resolution is measured from the observed width of the Z. The observed width has contributions from the Breit-Wigner and from detector resolution. The Breit-Wigner width is known to very high precision from LEP experiments [16], and the detector component is dominated by the energy resolution. The electron energy resolution (ΔE) can be parameterized as $\Delta E/E = \mathcal{C} \oplus \mathcal{S}/\sqrt{E_T}$, where $\mathcal{C}$ and $\mathcal{S}/\sqrt{E_T}$ are called the constant and sampling terms, respectively. $\mathcal{S}$ is known to high precision from test beam studies and is

0.135 $\mathrm{GeV}^{1/2}$ for CC electrons and 0.157 $\mathrm{GeV}^{1/2}$ for EC electrons. To determine the constant term $\mathcal{C}$, Monte Carlo Z experiments are generated with different values of $\mathcal{C}$. The predicted invariant mass distribution for each experiment is fit to a Breit-Wigner convoluted with a gaussian. The Breit-Wigner width is fixed, but the gaussian width is allowed to float. The data is fit in the same way, and $\mathcal{C}$ in the simulation is adjusted until the Monte Carlo and data distributions have the same width. Figure 4.5 shows the result of fitting the invariant mass distribution of CC-CC $Z \to ee$ candidates to a Breit-Wigner convoluted with a gaussian. Figure 4.6 shows the r.m.s. of the gaussian that is obtained when the same procedure is applied to Monte Carlo as a function of the CC constant term, along with the result from the data. The intersection of the two gives the constant term. The constant term in the CC is thus determined to be 0.014 ± 0.002 with the uncertainty being dominated by the statistics of the $Z \to ee$ sample. In a similar manner, the constant term in the EC is determined to be $0.00^{+0.01}_{-0.00}$.

The uncertainty in the polar angle of CC electrons is parameterized as an uncertainty in the position of the track at a radius of 62 cm for CDC tracks. The z position of the track at this radius has a 0.3 cm uncertainty. The uncertainty in the polar angle for EC electrons is absorbed into the large uncertainty in the EC energy scale.

Hadronic Scale

The hadronic recoil vector is reconstructed by simply summing the transverse momentum vectors of all the cells in the calorimeter excluding those cells assigned to the electrons. The response of the calorimeter to the hadronic recoil differs from the response to objects which shower electromagnetically. This difference

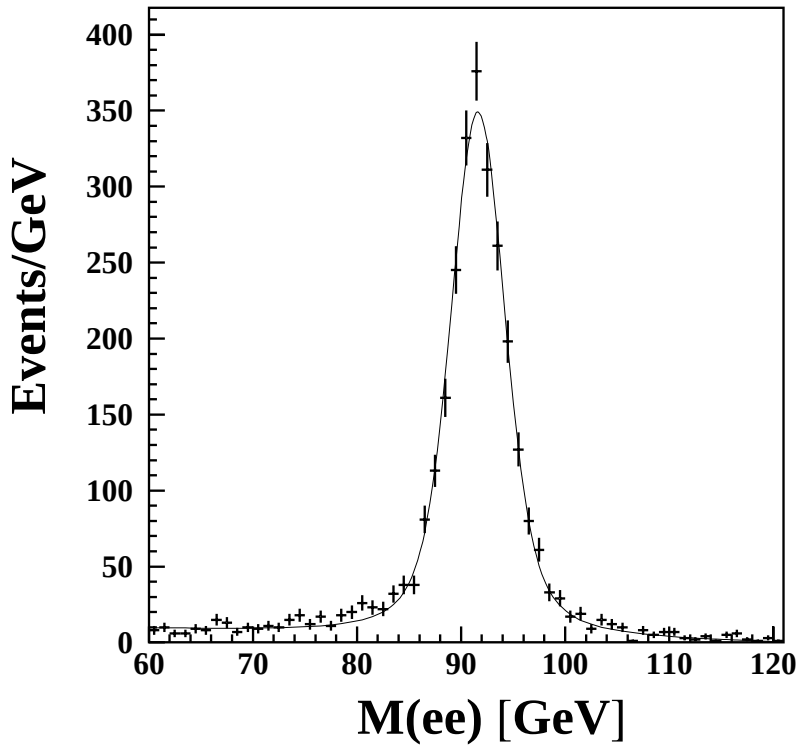

Figure 4.5: Invariant mass distribution for the CC-CC $Z \to ee$ data sample. A Breit-Wigner convoluted with a gaussian resolution is fit to this distribution, and the width is used to determine the constant term in the CC electron energy resolution. The χ^2 per degree of freedom for the fit is 88.7/56.

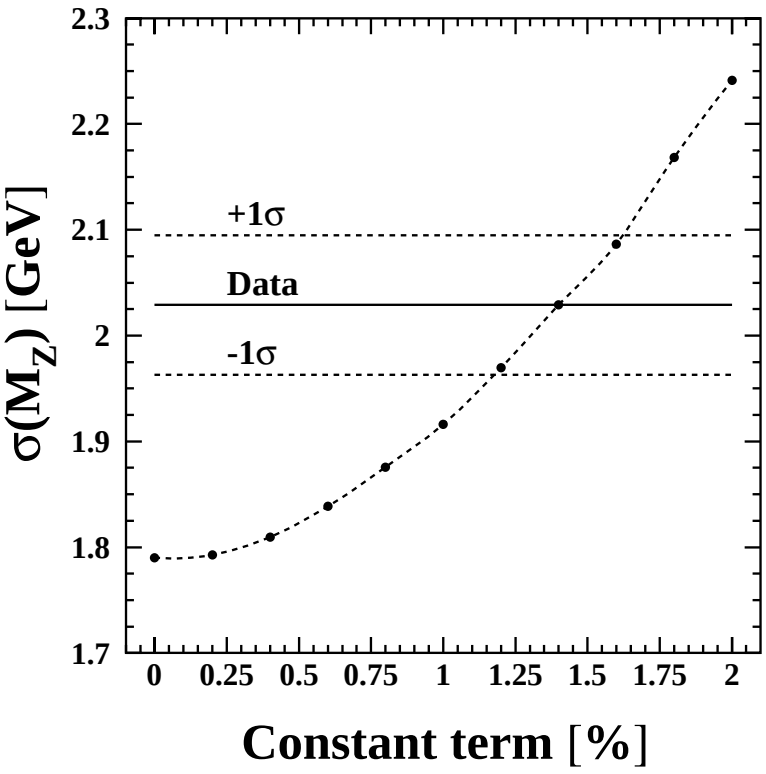

Figure 4.6: Determination of the constant term for the electron energy resolution. The curved dashed line connecting the Monte Carlo points shows the correlation between the constant term in the CC electron energy resolution and the fitted width of the CC-CC $Z \to ee$ invariant mass distribution from the Monte Carlo. The horizontal solid line shows the fitted width of the CC-CC data sample, and the horizontal dashed lines the uncertainty on the fitted width. From the intersection of the data line with the curved dashed line we determine the constant term for CC electrons to be 0.014 ± 0.002.

occurs because the hadronic calorimeter modules are physically different from the electromagnetic modules, and because the processes by which hadrons interact in material are different from electron and photon interactions. The hadronic response of the calorimeter is determined using $Z \to ee$ events, by comparing the p_T^Z measured from the electron pair to that measured from the hadronic system. The particle distributions in the W and Z recoil distributions should be very similar, so this determination should be valid for both. To perform this comparison it is useful to use a coordinate system in the transverse plane which depends only on the electron directions, and not the momenta. The $\hat{\eta}$ axis, which is unrelated to pseudorapidity, is defined as the bisector of the azimuthal angle between the two electrons, as shown in Figure 4.7. The $\hat{\xi}$ axis is perpendicular to $\hat{\eta}$. The $\hat{\eta}$ projections of the recoil are minimally sensitive to the electron energy resolution. One can therefore best understand the hadronic response by comparing the component of the p_T of the Z boson along $\hat{\eta}$ as calculated using the energies of the electrons, $(p_T^{ee})_\eta$, to that calculated by summing the transverse momentum of all towers in the calorimeter, except those containing the electrons, $(p_T^{\mathrm{rec}})_\eta$.

The true momentum vectors of the dielectron and recoil systems are equal and opposite by momentum conservation. Therefore, if the hadron and electron responses were equivalent,$(p_T^{ee})_\eta + (p_T^{\mathrm{rec}})_\eta$ would be zero on average. Because the calorimeter response is different for electrons and for recoil particles, the algebraic sum of $(p_T^{\mathrm{rec}})_\eta$ and $(p_T^{\mathrm{ee}})_\eta$ is on average non zero. The average value of this "η-imbalance" scales linearly with $(p_T^{ee})_\eta$. A relative scale α_H would cause a slope of approximately $1 - \alpha_H$ in the plot of $(p_T^{ee})_\eta + (p_T^{\mathrm{rec}})_\eta$ *vs.* $(p_T^{ee})_\eta$. This plot is shown in Figure 4.8.

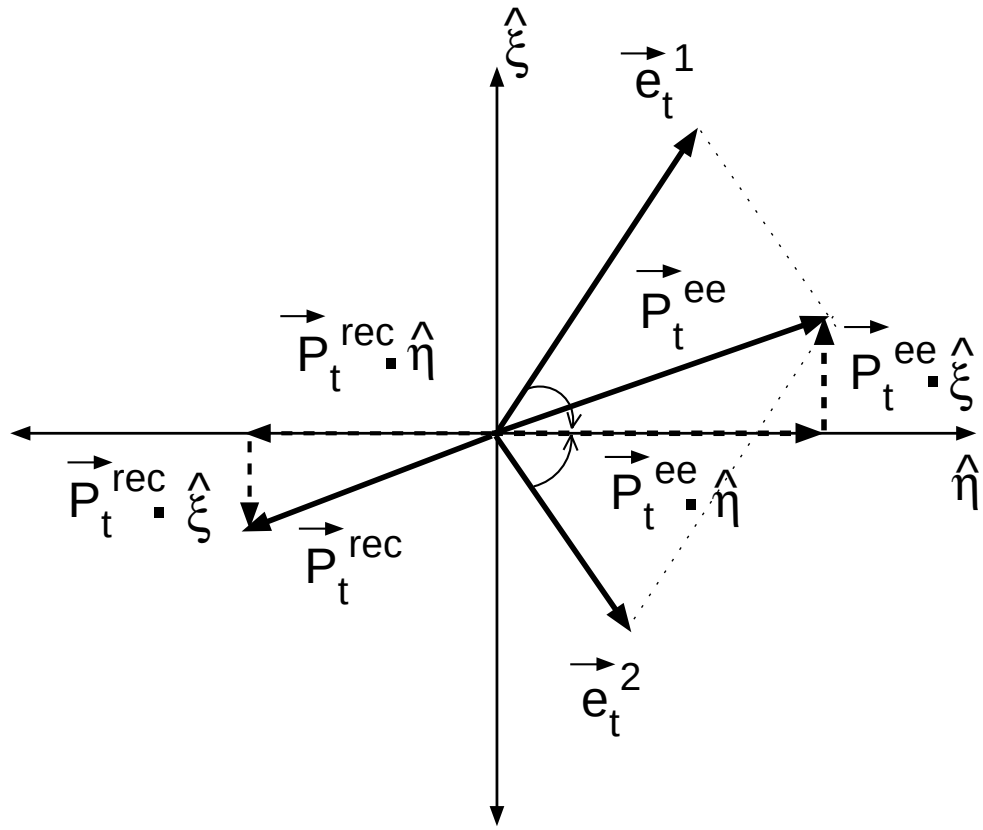

Figure 4.7: Definition of the η–ξ coordinate system in a $Z \to ee$ event. The $\hat{\eta}$ axis is the bisector of the electron directions in the transverse plane; the $\hat{\xi}$ axis is perpendicular to $\hat{\eta}$.

The recoil scale used in the simulation is tuned such that applying the same procedure to Monte Carlo events yields the same response as the data. Figure 4.9 shows the slope of the average $(p_T^{\rm rec})_\eta + (p_T^{\rm ee})_\eta$ versus $(p_T^{ee})_\eta$ from the Monte Carlo as a function of the hadronic scale, along with the slope determined from data. The intersection of the two determines the hadronic response to be 0.753 ± 0.024 relative to the electromagnetic energy scale, with the uncertainty being dominated by uncertainties in the EC electromagnetic energy scale.

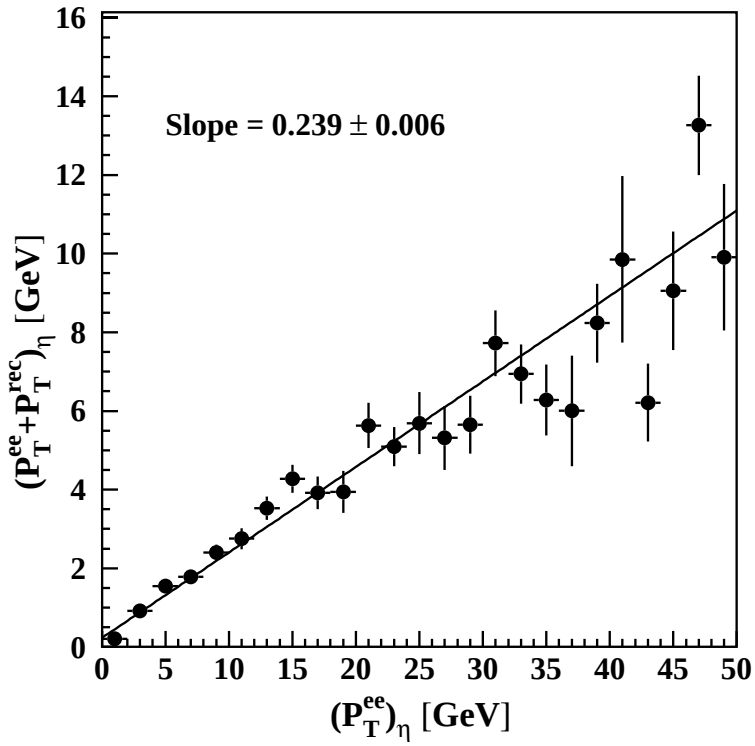

Figure 4.8: The η-imbalance, $(p_T^{\rm rec})_\eta + (p_T^{\rm ee})_\eta$, versus $(p_T^{ee})_\eta$ from the $Z \to ee$ sample. The solid line is a linear fit to the data points, with a slope of 0.239 ± 0.006.

Hadronic Resolution

Since the recoil is measured using a sum over the entire calorimeter, the hadronic resolution receives contributions from every process which affects the calorimeter. These processes include electronic and uranium noise, multiple interactions, W

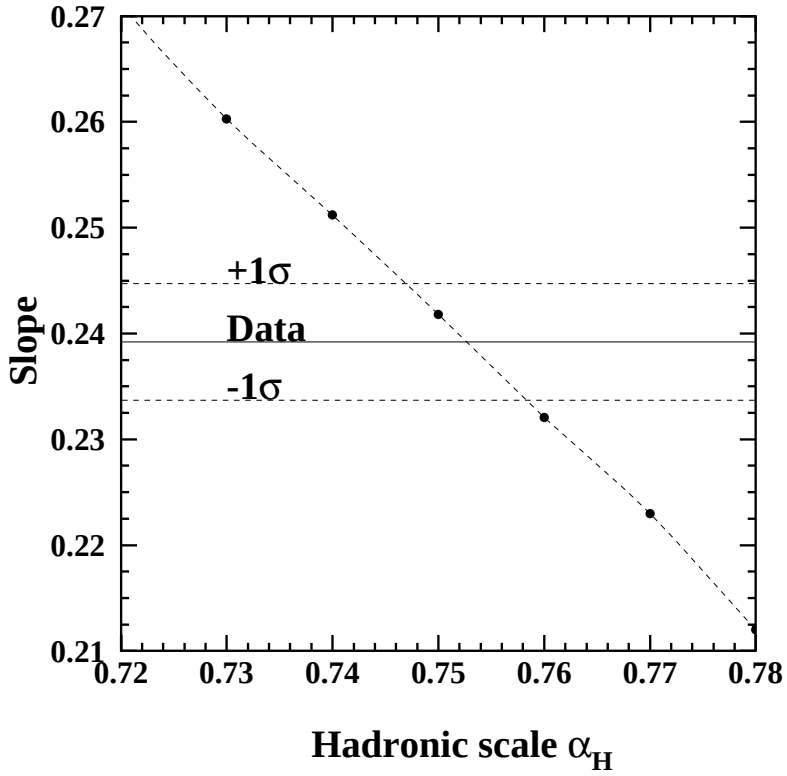

Figure 4.9: Determination of the hadronic scale α_H. The points represent the slope of the line $(p_T^{\rm rec})_\eta + (p_T^{\rm ee})_\eta$ versus $(p_T^{ee})_\eta$ obtained from Monte Carlo as a function of α_H. The intersection of the dashed line connecting the Monte Carlo points with the solid line, obtained from data, determines the hadronic scale used in the simulation. We take $\alpha_H = 0.753 \pm 0.024$.

or Z underlying event, and the recoil system itself. It is clearly difficult to model all these processes, and therefore collider data is used to measure the hadronic

resolution. The hadronic energy resolution is parameterized in the same way as the electron energy resolution, and from jet studies [56] it is found to have a constant term of 4% and a sampling term of $0.8/\sqrt{p_T/\mathrm{GeV}}$.

The underlying event is modeled using events taken with a LØ trigger (minimum bias events) with the same luminosity profile as the W and Z boson samples. Since these events should not contain high p_T neutrinos, the $\not\!\!E_T$ of minimum bias events is indicative of the resolution due to the underlying event. We pick a minimum bias event randomly from this sample, and its $\not\!\!E_T$ is combined vectorially with that of the simulated W boson. To account for any possible difference between the underlying event in W boson and in minimum bias events, we scale the $\not\!\!E_T$ vector chosen from the minimum bias sample by a multiplicative scale factor. The scale factor is estimated using the $Z \to ee$ sample and set so that the width of the "η-balance" distribution from the simulation agrees with that from the data, where "η-balance" is $(p_T^{\mathrm{rec}})_\eta$ (corrected for the hadronic scale) subtracted from $(p_T^{ee})_\eta$. Figure 4.10 shows this quantity for the $Z \to ee$ event sample. Figure 4.11 shows the r.m.s. of the $(p_T^{\mathrm{rec}})_\eta$ distribution from the simulation as a function of the minimum bias scale factor. The simulation has the same r.m.s. as the data when the scale factor between the minimum bias events and the W boson underlying events is 1.01 ± 0.02.

Figure 4.12 shows the electron detector pseudorapidity distribution, η_D, for $Z \to ee$ candidates and for the Monte Carlo after all corrections and cuts except for track match have been applied. The sharp edges correspond to the fiducial requirements applied to the electrons. The data and the Monte Carlo agree well. Since the tracking efficiency is obtained from the Z data (as explained in Chapter 5), the figure shows electrons without the tracking requirement.

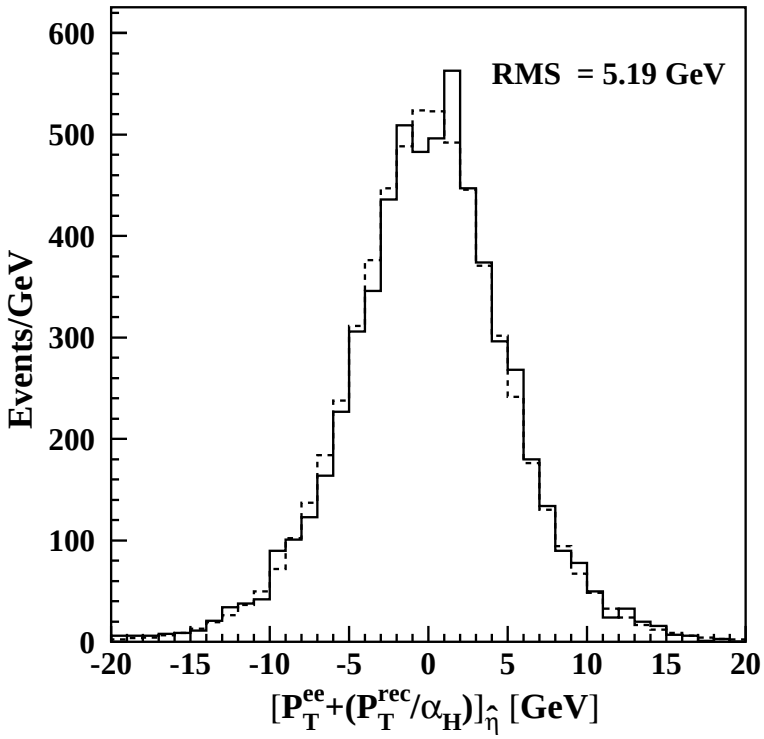

Figure 4.10: Distribution of the "η-balance", the magnitude of the vectorial sum of $(p_T^{rec})_\eta/\alpha_H$ and $(p_T^{ee})_\eta$, for events in the $Z \to ee$ sample (solid histogram), and for Monte Carlo (dashed histogram).

Figure 4.13 shows the transverse energy distribution of the highest and second highest E_T electron for the $Z \to ee$ candidates and for the Monte Carlo. The kinematic cut on both electrons is $E_T > 25$ GeV.

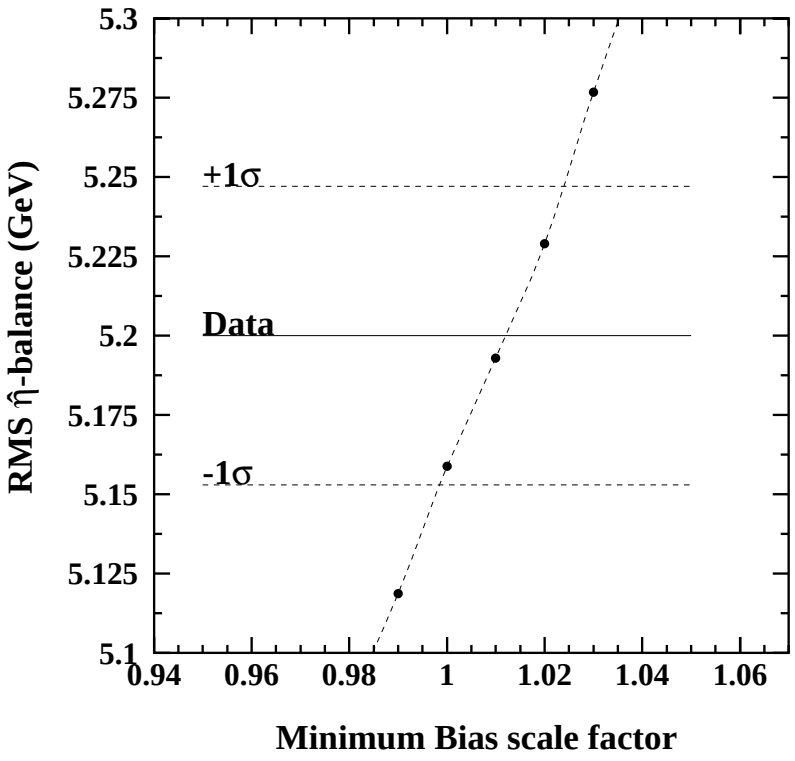

Figure 4.11: Determination of the minimum bias scale factor. The points represent the r.m.s. of the η-balance distribution from Monte Carlo as a function of the minimum bias scale factor. The solid horizontal line shows the r.m.s. from the data sample. The intersection of the dashed line connecting the Monte Carlo points with the data line determines the minimum bias scale factor used in the simulation to be 1.01 ± 0.02.

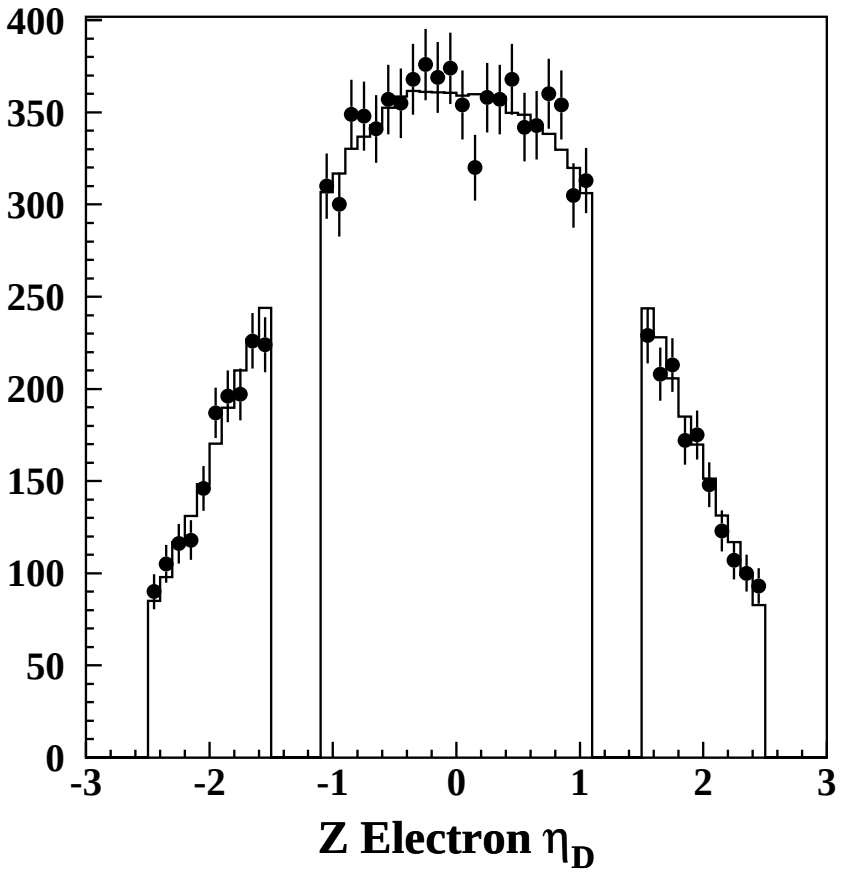

Figure 4.12: The electron η_D distribution for $Z \to ee$ candidates (solid circles) and for the Monte Carlo (histogram) after all corrections and cuts except track match have been applied. The error bars represent the statistical uncertainty in the data.

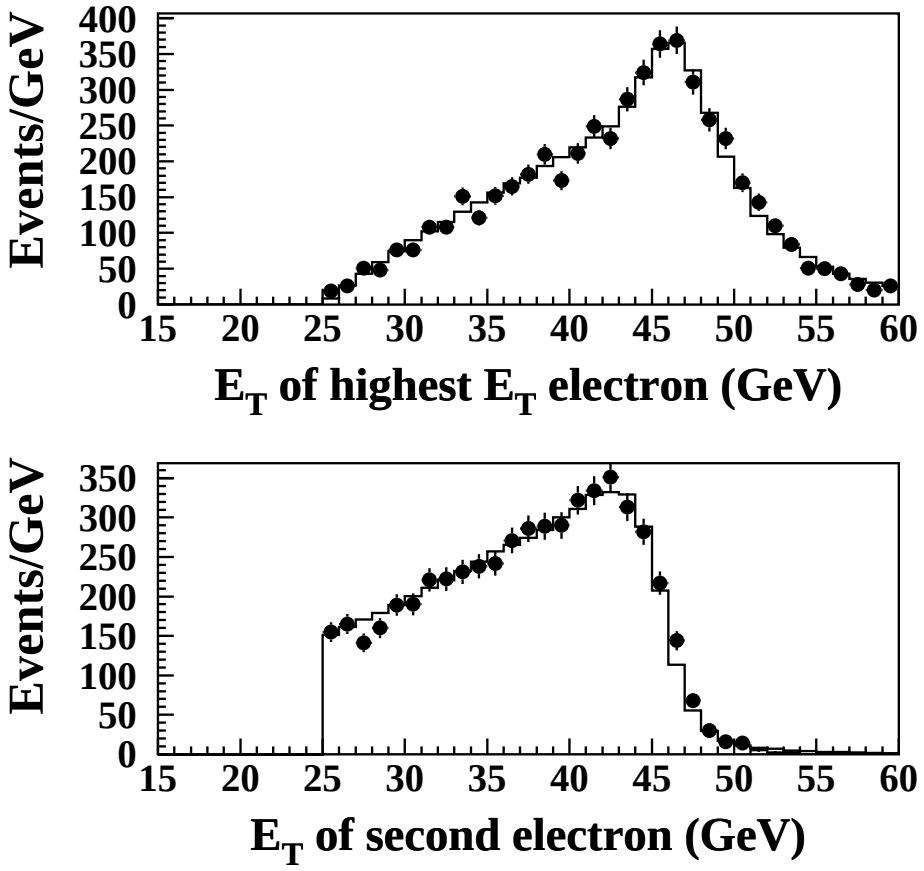

Figure 4.13: The electron E_T distribution for $Z \to ee$ candidates (solid circles) and for the Monte Carlo (histogram) after cuts and corrections have been applied. The error bars represent the statistical uncertainty in the data. The top plot corresponds to the highest E_T electron and the bottom plot to the second electron for each $Z \to ee$ event.

4.2 Geometric and Kinematic Acceptance

The acceptance is defined as the fraction of generated $W \to e\nu$ or $Z \to ee$ events satisfying the kinematic and geometric requirements. Samples of 25,000,000 events are used to estimate all systematic uncertainties, except those from ambiguities in the parton distribution functions and differences in generators. For these, we use the slower PYTHIA generator and samples of 1,000,000 events, corresponding to a statistical error of 0.1%, which is small compared to the dominant uncertainties. Table 4.1 shows the acceptance results and a summary of the systematic uncertainties.

The systematic uncertainties are obtained by varying the input parameters to the CMS Monte Carlo. The uncertainties from the boson p_T spectra are calculated by varying the theoretical parameters in Ref. [12] within the range quoted by the authors. The systematic uncertainties from the choice of parton distribution functions are calculated from the largest excursion in acceptance found using the CTEQ4M [54], CTEQ2pM [54], MRSD- [58], MRS(G) [59], GRV94HO [60], and versions of the MRSAp distribution functions with values of the strong coupling constant ranging from 0.150 to 0.344 [61].

The systematic uncertainties in the acceptance due to the presence of radiative photons in the event come from uncertainties in the minimum separation in η-ϕ space the electron and the photon must have in order to be resolved as separate clusters by the calorimeter clustering algorithm. The uncertainties due to effects of the clustering algorithm are calculated by varying the size $R = \sqrt{\Delta\eta^2 + \Delta\phi^2}$ of the cone that is used to decide whether or not the photon will be resolved from the electron in the detector between 0.2 and 0.4.

We use a W boson mass of 80.375 GeV and width of 2.066 GeV, and vary

Table 4.1: Acceptances, their ratio, and their systematic uncertainties for W and Z boson events.

	A_W	A_Z	$\frac{A_W}{A_Z}$
Acceptance	0.465 ± 0.004	0.366 ± 0.003	0.787 ± 0.007
Error source	$\frac{\delta A_W}{A_W}$ [%]	$\frac{\delta A_Z}{A_Z}$ [%]	$\delta\left(\frac{A_Z}{A_W}\right)/\left(\frac{A_Z}{A_W}\right)$ [%]
p_T spectrum	0.096	0.104	0.100
Parton distribution functions	0.189	0.314	0.252
Clustering algorithm	0.141	0.294	0.153
δM_W	0.130	—	0.130
$\delta_{,\ W}$	0.050	—	0.050
EM energy scale	0.685	0.337	0.698
EM energy resolution	0.024	0.037	0.044
Hadronic response	0.129	—	0.129
Hadronic resolution	0.078	—	0.078
Angular resolution	0.019	0.046	0.027
Generated mass range	0.150	0.180	0.234
Generator	0.343	0.516	0.172
Total	0.85%	0.78%	0.85%

these by ±0.065 GeV and ±0.060 GeV, respectively. The W mass is the result of combining the measurements from DØ [52], CDF [57], and a fit to all direct W mass measurements from LEP [43]. The W boson width is the current world

average [2, 3, 4, 5, 6, 7]. The systematic uncertainties in the acceptance due to the EM energy scale, EM resolution, hadronic response, and hadronic resolution are found by varying the relevant parameters in the Monte Carlo simulation by their individual uncertainties. The resolution on the polar angle of electron tracks is dominated by the uncertainty in the measurement of the track center of gravity. The uncertainty due to the angular resolution is therefore estimated by varying the position of the track's center of gravity within the measured resolutions.

The generation of W and Z bosons is limited to the mass ranges [40-120] GeV for W bosons and [30-150] GeV for Z bosons. The error quoted on generated mass in Table 4.1 is the uncertainty in the fraction of events outside this mass window that would pass our selection criteria. This is calculated by generating PYTHIA events in the range [0-1000] GeV. The error is dominated by the statistics of the Monte Carlo samples, but is well below the dominant uncertainties. The error quoted on the generator is from a comparison of the difference in acceptance between our Monte Carlo and PYTHIA (after smearing PYTHIA for detector response).

The acceptances and their uncertainties for $W \to e\nu$, $Z \to ee$, and their ratio are shown in Table 4.1. The W boson acceptance is $A_W = 0.465 \pm 0.004$. The largest contributions to the uncertainty arise from uncertainties in the EM energy scale, the difference between our generator and PYTHIA, and uncertainties in the parton distribution functions (pdf's). The acceptance for $Z \to ee$ events is $A_Z = 0.366 \pm 0.003$. The largest sources of systematic uncertainty arise from the difference between our generator and PYTHIA, uncertainties in the EM energy scale and in the parton distribution functions, and effects of the electron-photon

clustering algorithm in radiative Z decays. In the ratio of acceptances, a few of the systematic uncertainties are reduced by partial cancelations of correlated errors. The ratio of the acceptances is $A_Z/A_W = 0.787 \pm 0.007$. The largest contributions to the uncertainty in the ratio of acceptances arise from uncertainties in the EM energy scale and in the pdf's, and from effects of a finite generation mass window.

4.3 NLO Electroweak Radiative Corrections

Next to leading order (NLO) electroweak processes modify the cross sections and their ratio [62]. A full NLO calculation is available for the W boson, which suggests that the W boson cross section would decrease by a multiplicative factor of 0.998 ± 0.001 [63]. For the Z boson, only the full QED calculation is available, missing the purely weak part. For the ratio $\mathcal{R}$, the best theoretical estimate at this time is a multiplicative factor of 1.00 ± 0.01 [63], where the uncertainty is dominated by the difference between the NLO corrections to the W and Z boson cross sections, due mainly to the purely weak corrections missing in the Z boson calculation. This theoretical uncertainty is therefore expected to be reduced in the future. A 1% uncertainty on $\mathcal{R}$ due to NLO electroweak radiative corrections is quoted in this analysis.

Chapter 5

Efficiencies

The trigger and offline selection cuts used to identify genuine $Z \to ee$ or $W \to e\nu$ events and to reduce the background cause a fraction of the real signal to be lost. For example, shower fluctuations could cause a genuine electron to be rejected by the isolation or shower shape requirement, or an electron track could be lost due to an inefficiency of the central detector. This chapter concerns the measurement of the frequency at which signal events are lost due to the selection cuts themselves.

5.1 Electron Identification Efficiencies

An accurate measurement of the efficiency of the electron identification cuts requires a clean sample of unbiased electrons. This sample, called the *diagnostic* sample, should in principle be selected with a minimum of cuts, thus avoiding the introduction of any bias. These cuts must also be uncorrelated with the one that is under study. One might be tempted to consider a beam of pure electrons delivered to the detector. This was indeed done in test beam measurements where the initial attempts at defining the electron selection criteria were

developed. However, it is not possible to deliver such a beam to the actual DØ detector. The alternative is then to rely on collider data to provide the required diagnostic sample from which the selection criteria can be measured. Samples of electrons from W and Z events are perfect candidates for such diagnostic samples, since the electrons then have all the characteristics (e.g. the underlying event or multiple interactions effects) which might affect the efficiencies that need to be measured.

Despite its large size, efficiency measurements from a sample of W electrons is quite difficult, since the reconstruction of the W invariant mass is impossible due to the presence of a neutrino. Without a characteristic Breit-Wigner to yield a mass region with good signal to background ratio and with easily estimated backgrounds, one is reduced to using electron selection criteria just to define the diagnostic sample, thus introducing bias and possible correlation effects.

$Z \to ee$ events are much better suited for the task at hand: by requiring the reconstructed dielectron invariant mass to be close to M_Z, and by imposing the tight electron identification criteria on one of the electrons, one obtains a clean sample of unbiased, or *probe*, electrons which contain little background. Of course, the precision of the measurement is statistically limited by the number of available $Z \to ee$ events. In addition, any uncertainty in the determination of the amount of background will give rise to a systematic uncertainty in the efficiency measurement.

The diagnostic sample of electrons is obtained from a $Z \to ee$ sample passing the EM2_EIS_ESC Level-2 filter, which requires one isolated EM cluster with $E_T > 20$ GeV, and a second EM cluster with no requirement other than $E_T > 16$ GeV. Since a Level-2 transverse energy cut of 16 GeV is 100% efficient for elec-

trons with offline transverse energy $E_T > 25$ GeV, this loosely triggered electron becomes the *probe* electron from which the efficiency of the offline selection cuts will be measured.

An electron is considered a *probe* electron if the other electron in the event passes all the tight electron requirements (see Section 3.5), both electrons have $E_T > 25$ GeV, and M_{ee} is close to M_Z. We count the number of events inside a Z invariant mass M_{ee} window before and after applying the electron identification criteria under study to *each* probe electron. The ratio of these numbers after background subtraction gives the efficiency. It is important to note that the tight electron cuts are applied for each EM cluster in the event. Therefore, in the case where both electrons are tight, the event is used twice in the efficiency calculation.

5.1.1 Background Subtraction

In order to quantify the uncertainty in the efficiencies due to the background subtraction mechanism, four methods are used to determine the background:

A. A sideband averaging technique. Lower and upper sideband regions are defined outside the signal region of $86 < M_{ee} < 96$ GeV in order to estimate the amount of background. The lower sideband region is $60 < M_{ee} < 70$ GeV, and the upper sideband region is $110 < M_{ee} < 120$ GeV. These regions are chosen to be symmetric about the signal region, and cover the same range in invariant mass. The number of background events is then taken to be the average of the two sideband regions;

B. Method *A* is repeated for a signal region $81 < M_{ee} < 101$ GeV. With this

signal region, the number of background events is taken to be the sum of the two sideband regions;

C. The dielectron mass spectrum is fit using a Breit-Wigner convoluted with a Gaussian (to account for the resolution in the measurement) and a linear background in the region $70 < M_{ee} < 110$ GeV. The linear fit parameters are then used to estimate the number of background events which must be subtracted out. The signal window is $86 < M_{ee} < 96$ GeV;

D. Method *C* is repeated for a signal window $81 < M_{ee} < 101$ GeV.

Figure 5.1 illustrates the background subtraction methods.

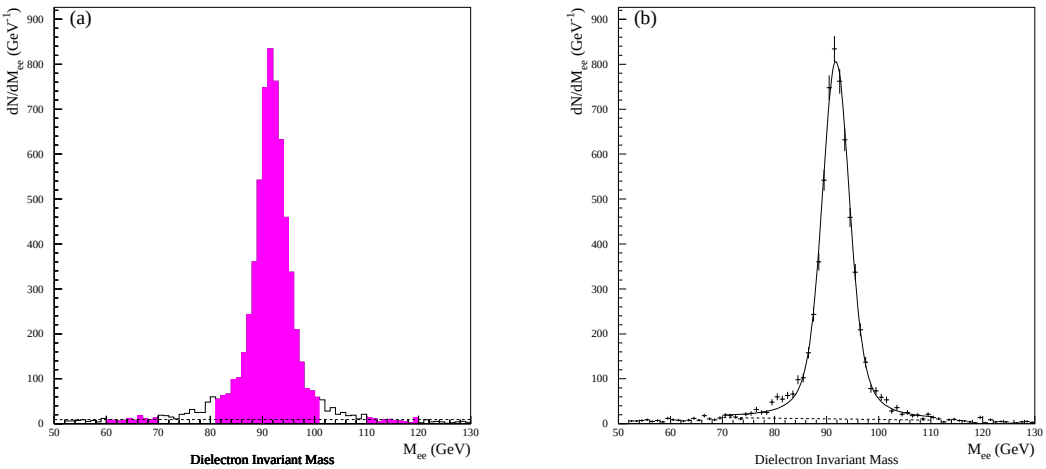

Figure 5.1: Illustration of the background subtraction methods used in the determination of electron identification efficiencies: (a) sideband technique, and (b) fit technique. The dashed line shows the estimated background.

An exponential shape for the background was also used as a check, and the efficiencies resulting from such a fit agree well within the corresponding uncertainties. We have checked for any dependence of the efficiency on the E_T

of the electron, and find no effect beyond $E_T = 25$ GeV. Table 5.1 summarizes the four methods employed.

Table 5.1: Summary of the background subtraction methods used in estimating electron selection efficiencies.

Method	Background Subtraction	Signal Region
A	Sideband [60-70] [110-120] GeV	$86 < M_{ee} < 96$ GeV
B	Sideband [60-70] [110-120] GeV	$81 < M_{ee} < 101$ GeV
C	BW$\otimes$G + P1 fit	$86 < M_{ee} < 96$ GeV
D	BW$\otimes$G + P1 fit	$81 < M_{ee} < 101$ GeV

5.1.2 Single Electron Efficiencies

Five different cuts are imposed on the probe electrons, creating five different electron classes:

1. Probe electron: an electron which passes the Level-2 trigger requirement of $E_T > 16$ GeV ($esc16$). All other cuts are measured relative to this baseline cut;

2. Trigger electron: a probe electron which passes the Level-2 trigger requirements of $E_T > 20$ GeV and loose isolation and shower shape ($eis20$);

3. Track electron: a trigger electron which passes the tracking requirements, namely a matching track with $S_{\rm trk} < 5(10)$ in the CC(EC);

4. Loose electron: a trigger electron which passes the calorimetric identification criteria, namely $f_{\rm em} > 0.95$, $\chi^2_{\rm hm} < 100$, and $f_{\rm iso} < 0.15$;

5. Tight electron: a loose and track electron.

The number of signal (*i.e.* background subtracted) electrons which are contained in each category are summarized in Table 5.2. They form the basis for the different relative efficiencies which are defined and measured:

$$\begin{aligned}
\text{Level} - 2 \text{ trigger efficiency} \quad \epsilon_{\mathrm{L2}} &\equiv \frac{\#\text{ Trigger electrons}}{\#\text{ Probe electrons}} \,, \\
\text{Calorimeter ID efficiency} \quad \epsilon_{cal} &\equiv \frac{\#\text{ Loose electrons}}{\#\text{ Trigger electrons}} \,, \\
\text{Loose ID efficiency} \quad \epsilon_{l} &\equiv \frac{\#\text{ Loose electrons}}{\#\text{ Probe electrons}} = \epsilon_{L2} \cdot \epsilon_{cal} \,, \\
\text{and} \qquad \text{Tracking efficiency} \quad \epsilon_{trk} &\equiv \frac{\#\text{ Tight electrons}}{\#\text{ Loose electrons}} \,.
\end{aligned}$$

For example, the tracking efficiency for central electrons using method A is:

$$\epsilon_{trk} = \frac{3807}{4817} = 0.7903 \pm 0.0059 \,, \tag{5.1}$$

where the statistical error is binomial:

$$\epsilon = \frac{\mathrm{N}}{\mathrm{M}} \quad \Longrightarrow \quad \delta\epsilon_{stat} = \sqrt{\frac{\epsilon \cdot (1-\epsilon)}{\mathrm{M}}} \,. \tag{5.2}$$

The results of the relative efficiency calculations are listed in Table 5.3 and Table 5.4 for central and forward electrons, respectively.

5.1.3 Efficiency Correlations

The method used to measure the electron efficiencies from $Z \to ee$ events assumes that the efficiency for an electron to pass a certain cut is independent of whether there is a second electron in the event. Suppose we want to measure the efficiency of a certain cut. We tag one electron as *tight* (we call this electron the *tag* electron), and see how many *probe* electrons pass the cut under study. Recall that events with two tag electrons are therefore counted twice. The efficiency is

Table 5.2: Number of (background subtracted) central (CC) and forward (EC) electrons contained in the $Z \to ee$ signal window for various offline cuts and background subtraction methods.

Electron type	CC				EC			
	N_A	N_B	N_C	N_D	N_A	N_B	N_C	N_D
Probe	5251	6236	5222	6179	2197	2683	2212	2713
Trigger	5163	6104	5151	6082	2181	2675	2191	2695
Track	4031	4743	4030	4741	1623	1973	1641	2009
Loose	4817	5670	4798	5633	1898	2310	1919	2352
Tight	3807	4463	3801	4453	1411	1705	1433	1749

Table 5.3: Central electron relative identification efficiencies (quoted errors are statistical).

CC electron efficiencies			
Method	ϵ_{L2}	ϵ_l	ϵ_{trk}
A	0.9832 ± 0.0018	0.9173 ± 0.0038	0.7903 ± 0.0059
B	0.9788 ± 0.0018	0.9092 ± 0.0036	0.7871 ± 0.0054
C	0.9864 ± 0.0016	0.9188 ± 0.0038	0.7923 ± 0.0059
D	0.9843 ± 0.0016	0.9117 ± 0.0036	0.7905 ± 0.0054

Table 5.4: Forward electron relative efficiencies (quoted errors are statistical).

EC electron efficiencies			
Method	ϵ_{L2}	ϵ_l	ϵ_{trk}
A	0.9927 ± 0.0018	0.8639 ± 0.0073	0.7432 ± 0.0010
B	0.9970 ± 0.0011	0.8610 ± 0.0067	0.7381 ± 0.0092
C	0.9905 ± 0.0021	0.8675 ± 0.0072	0.7465 ± 0.0099
D	0.9934 ± 0.0016	0.8669 ± 0.0065	0.7437 ± 0.0090

then given by the number of probe electrons passing the cut divided by the total number of probe electrons:

$$\epsilon_{\text{cut}} = \frac{2(tt) + (tp)}{2(tt) + (tp) + (tf)} \,, \tag{5.3}$$

where

- tt = number of events where both electrons pass the tight cuts;
- tp = number of events where one electron passes the tight cuts and the other passes the cut under study but fails the tight cuts;
- tf = number of events where one electron passes the tight cuts and the other electron fails the cut under study (and therefore fails tight cuts as well).

The total number of probe electrons N can be divided into N_{pass} and N_{fail}, with N_{tag} a subset of N_{pass}, as illustrated in Figure 5.2. With these definitions in mind, the following relations hold for the different efficiencies:

- $\epsilon_{\text{tag}} = N_{\text{tag}}/N$
- $\epsilon_{\text{pass}} = N_{\text{pass}}/N$
- $\epsilon_{\text{fail}} = N_{\text{fail}}/N = (N - N_{\text{pass}})/N = 1 - \epsilon_{\text{pass}}$
- $\epsilon_{\text{pass-NO-tag}} = (N_{\text{pass}} - N_{\text{tag}})/N = \epsilon_{\text{pass}} - \epsilon_{\text{tag}}$

If there are no correlations between the electrons, we can use the above relations to calculate the efficiencies:

$$\begin{aligned} \epsilon_{tt} &= \epsilon_{\text{tag}}^2 \\ \epsilon_{tp} &= 2\epsilon_{\text{tag}}(\epsilon_{\text{pass}} - \epsilon_{\text{tag}}) \\ \epsilon_{tf} &= 2\epsilon_{\text{tag}}(1 - \epsilon_{\text{pass}}) \end{aligned} \tag{5.4}$$

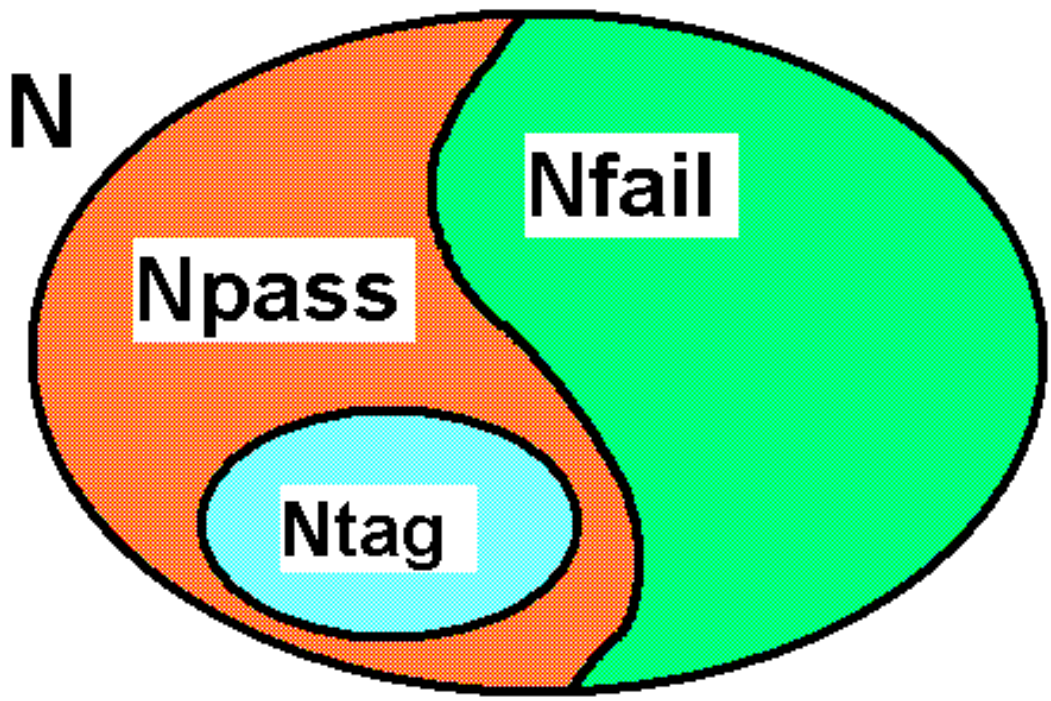

Figure 5.2: Illustration of sample sets used to measure the electron identification efficiencies.

and $\epsilon_{\rm cut}$ in equation 5.3 reduces to $\epsilon_{\rm pass}$:

$$\begin{aligned}\epsilon_{\rm cut} &= \frac{2(tt)+(tp)}{2(tt)+(tp)+(tf)} = \frac{2\epsilon_{\rm tag}^2 + 2\epsilon_{\rm tag}(\epsilon_{\rm pass}-\epsilon_{\rm tag})}{2\epsilon_{\rm tag}^2 + 2\epsilon_{\rm tag}(\epsilon_{\rm pass}-\epsilon_{\rm tag}) + 2\epsilon_{\rm tag}(1-\epsilon_{\rm pass})} \\ &= \frac{2\epsilon_{\rm tag}\epsilon_{\rm pass}}{2\epsilon_{\rm tag}\epsilon_{\rm pass} + 2\epsilon_{\rm tag} - 2\epsilon_{\rm tag}\epsilon_{\rm pass}} = \epsilon_{\rm pass}\ .\end{aligned}$$

In using this method, one therefore makes the implicit assumption that there are no correlations and that relations 5.4 hold.

The W and Z *electron* efficiencies are given by

$$\epsilon_W^{ele} = \epsilon_l \epsilon_t \tag{5.5}$$

$$\epsilon_Z^{ele} = \epsilon_{ll}(\epsilon_{tt} + \epsilon_{tl}) \tag{5.6}$$

It is important to define these precisely:

- ϵ_l = loose electron efficiency;
- ϵ_t = tracking efficiency = efficiency for a *loose* electron to pass tight requirements;
- ϵ_{ll} = efficiency for *both* electrons in a $Z \to ee$ event to pass loose requirements;
- ϵ_{tt} = efficiency for both loose electrons to pass tracking;
- ϵ_{tl} = efficiency for one loose electron to pass tracking and the other loose electron to fail tracking.

If efficiencies were uncorrelated,

$$\begin{aligned} \epsilon_{tt} &= \epsilon_t^2 \\ \epsilon_{tl} &= 2\epsilon_t(1-\epsilon_t) \\ \epsilon_{ll} &= \epsilon_l^2 \end{aligned} \tag{5.7}$$

Substituting 5.7 into 5.6 then gives

$$\epsilon_Z^{ele} = \epsilon_l^2(2\epsilon_t - \epsilon_t^2)\ . \tag{5.8}$$

This is the formula used in the overall Z electron efficiency, and it is simply the efficiency for both electrons to pass the loose cuts times the efficiency for at least one electron to pass the tracking cuts, as required by the $Z \to ee$ selection. The efficiency for the tracking requirement (that at least one of the electrons be tight) can be thought of as the efficiency that *not* both electrons fail the tracking, or $1-(1-\epsilon_t)^2$.

Loose Efficiency Correlations (Calorimeter ID)

To check for correlations in the efficiency of the loose cuts, which are all calorimetric requirements, we use a Monte Carlo sample of $Z \to ee$ events generated with HERWIG [64] and with detector response modeled through the DØ Shower Library [65]. We define

- N = number of events with 2 EM clusters passing only fiducial and kinematic requirements = 45092;
- pp = number of events with 2 loose electrons = 37167;
- pf = number of events with 1 loose electron = 7486;
- ff = number of events with 0 loose electrons = 439.

If there are no correlations, the loose electron efficiency is calculated as

$$\epsilon_l = \frac{2pp}{2pp + pf} \tag{5.9}$$

where

$$\begin{aligned} \epsilon_{pp} &= \epsilon_l^2 \\ \epsilon_{pf} &= 2\epsilon_l(1-\epsilon_l) \\ \epsilon_{ff} &= (1-\epsilon_l)^2 \end{aligned} \tag{5.10}$$

(using the relations 5.10, the right hand side of Equation 5.9 reduces to ϵ_l as expected).

The electron efficiency for the $W \to e\nu$ selection is given in Equation 5.5. The component of this efficiency that is due to the loose electron requirements is just ϵ_l. Assuming no correlations and using Equation 5.9 gives

$$\epsilon_l = 0.9085 \tag{5.11}$$

If there are correlations between the electrons in the loose efficiency, the correct way to calculate ϵ_l is to divide the number of EM clusters which pass the loose cuts by the total number of clusters:

$$\epsilon_l = \frac{2pp + pf}{2(pp + pf + ff)} = 0.9072 \tag{5.12}$$

The ratio of the two methods is 1.0014.

The electron efficiency for the $Z \to ee$ selection is given in Equation 5.6. The component of this efficiency that is due to the loose electron requirements is ϵ_{ll}. Assuming no correlations and using Equations 5.9 and 5.7 gives

$$\epsilon_{ll} = 0.8254 \tag{5.13}$$

If there are correlations, the correct way to calculate ϵ_{ll} is to divide the number of events in which both EM clusters pass the loose cuts by the total number of events:

$$\epsilon_{ll} = \frac{pp}{pp + pf + ff} = 0.8242 \tag{5.14}$$

The ratio between the two methods is 1.0013.

The differences between the efficiencies are smaller than their uncertainty. The effect of efficiency correlations in the calorimetric requirements can therefore be safely neglected.

Tracking Efficiency Correlation

While Monte Carlo simulations have been shown to reliably describe the DØ calorimeter, no reliable simulation exists for the central detector. To study any possible correlations between the tracking efficiency for the electrons, we therefore use a data sample of events which have 2 loose electrons. Since the

tracking efficiency is measured relative to the loose efficiency, this is a valid diagnostic sample.

We plot M_{ee} and obtain background-subtracted numbers in the signal region. Method A is used for the background subtraction in the following discussion, but all methods give almost identical results. The tracking efficiency ϵ_t is the efficiency for a loose electron to pass tracking. We now define:

- tt = background subtracted number of events with 2 tight electrons
  = 2550.0
- tl = background subtracted number of events with 1 tight electron
  = 1400.5
- ll = background subtracted number of events with 0 tight electrons
  = 261.0

If there are no correlations, the tracking efficiency is calculated as in Equation 5.9:

$$\epsilon_t = \frac{2tt}{2tt + tl} \tag{5.15}$$

The electron efficiency of the $W \to e\nu$ selection is given in Equation 5.5. The part of this efficiency that is due to the tracking requirement is just ϵ_t. Assuming no correlations and using Equation 5.15 gives

$$\epsilon_t = 0.7846 \tag{5.16}$$

If there are correlations, the correct way to calculate ϵ_t is to divide the number of loose electrons which pass the tracking cut by the total number of loose electrons:

$$\epsilon_t = \frac{2tt + tl}{2(tt + tl + ll)} = 0.7718 \tag{5.17}$$

The ratio between the two methods is 1.017.

The electron efficiency of the $Z \to ee$ selection is given in Equation 5.6. The part of this efficiency that is due to the tracking requirement is $\epsilon_{tt}+\epsilon_{tl}$. Assuming no correlations and using Equations 5.15 and 5.7 gives

$$\epsilon_{tt} + \epsilon_{tl} = 0.9536 \tag{5.18}$$

If there are correlations, the correct way to calculate $\epsilon_{tt} + \epsilon_{tl}$ is to divide the number of events with at least one tight electron by the total number of events:

$$\epsilon_{tt} + \epsilon_{tl} = \frac{tt + tl}{tt + tl + ll} = 0.9380 \tag{5.19}$$

The ratio between the two methods is 1.017.

The electron efficiency for a W or Z boson thus found to be $(1.7 \pm 0.3)\%$ lower than what one would get assuming no correlations. The uncertainty here is the largest variation when one uses methods B, C and D instead of A for the background subtraction. The fact that this correction is the same for W and Z boson efficiencies is not an accident: the effect of this correlation cancels exactly in the ratio of the cross sections times electronic branching fractions. A mathematical proof of this is given in Appendix B. An example may help make this cancelation more intuitive. Suppose that most of the time, the probability that one of the electrons in a $Z \to ee$ event passes the tracking cuts is uncorrelated with the probability that the other electron passes. If, for certain runs, a detector malfunction were to cause all tracking to fail, the probability that one electron fails (100%) is 100% correlated with the probability that the other fails (100%). Since all Z and W events that occur during this hardware failure would be lost, the loss cancels in the ratio.

5.2 Trigger Efficiencies

The single electron efficiencies take into account the electron Level-2 terms (E_T and loose isolation and shower shape). However, two important factors remain to be measured: the efficiency of the Level-Ø system for detecting W and Z bosons, and the efficiency of the Level-2 $\not\!\!E_T$ requirement in the $W \to e\nu$ trigger.

5.2.1 Level-Ø Efficiency

The Level-Ø trigger imposes a inelastic scattering (minimum bias) requirement on all events. It requires simultaneous hits in both LØ counters, and the resultant fast z calculation must satisfy $|z_{vtx}| < 97$ cm. In order to calculate the Level-Ø efficiency for W and Z events, the Level-Ø system logic was modified during Run 1b: events passing the $W \to e\nu$ trigger were no longer required to fire the Level-Ø trigger, but the Level-Ø decision was saved along with the event. Due to the relatively lower number of Z candidate events, the Level-Ø efficiency measured by the W sample is used in both the W and Z cross section calculations. This is not a significant shortcoming, since the underlying events in W and Z boson production are essentially identical.

From a sample of events selected using the $W \to e\nu$ selection cuts with the Level-Ø requirement removed, the Level-Ø trigger efficiency is found to be

$$\epsilon_{\text{LØ}}(W) = \epsilon_{\text{LØ}}(Z) = 0.986 \pm 0.005 \,. \tag{5.20}$$

5.2.2 Level-2 $\not\!\!E_T$ Trigger Efficiency

In order to estimate the efficiency of the Level-2 missing transverse energy term, $\not\!\!E_T^{\mathrm{L2}}$, the W event criteria is applied on events collected with the single electron monitor trigger. The latter did not have the $\not\!\!E_T^{\mathrm{L2}} > 15$ GeV cut imposed. From a total of 5245 candidate events which were collected with this trigger, 5207 pass the $\not\!\!E_T^{\mathrm{L2}} > 15$ GeV requirement. Hence the $\not\!\!E_T$ trigger efficiency is:

$$\epsilon_{\mathrm{L2}met} = \frac{5207}{5245} = 0.993 \pm 0.001 \ . \tag{5.21}$$

5.3 Overall $W \to e\nu$ Selection Efficiency

The electron efficiency for the $W \to e\nu$ event selection, which requires a tight electron, is given by:

$$\epsilon_{ele}^{w} = \epsilon_l \cdot \epsilon_t \ , \tag{5.22}$$

ϵ_l is the efficiency of the loose cuts, $\epsilon_l = \epsilon_{L2} \cdot \epsilon_{cal}$, and ϵ_t is the tracking efficiency relative to the loose electron efficiency.

The values for ϵ_{ele}^{w} are computed for each background subtraction method using the efficiencies in Tables 5.3 and 5.4. Method D is used to quote the central value of the efficiency; the systematic error due to background subtraction is taken to be half the maximum difference between the various methods. Hence, the W selection efficiencies for central (CC) and forward (EC) electrons are:

$$\epsilon_{ele}^{w}(cc) = 0.7208 \pm 0.0058 \pm 0.0062 \tag{5.23}$$

$$\epsilon_{ele}^{w}(ec) = 0.6449 \pm 0.0092 \pm 0.0062 \ , \tag{5.24}$$

where the first error is statistical and the second systematic. To calculate the overall W electron selection efficiency, the CC and EC results are combined

based on the relative acceptance fractions, which are obtained from the CMS Monte Carlo. Of the events which pass the kinematic and fiducial requirements for the $W \to e\nu$ selection, 68.70% have the electron in the CC, and 31.30% in the EC. This gives

$$\varepsilon^{w}_{ele} = 0.6970 \pm 0.0082 \,, \tag{5.25}$$

where the quoted error combines the statistical and systematic errors in quadrature. The total W selection efficiency is obtained by combining the electron selection efficiency with the Level-Ø efficiency and the Level-2 $\not\!\!E_T$ efficiency, and dividing by 1.017 to correct for the tracking efficiency (see Section 5.1.3). We find

$$\varepsilon^{w}_{tot} = \epsilon_{\mathrm{L\emptyset}} \cdot \epsilon_{\mathrm{L2}met} \cdot \epsilon^{w}_{ele} = 0.6709 \pm 0.0087 \,. \tag{5.26}$$

5.4 Overall $Z \to ee$ Selection Efficiency

In the $Z \to ee$ event selection there are two electrons which have different efficiencies for different cryostats. The Z electron efficiency for the three distinct topologies are given by:

$$\epsilon^{z}_{ele}(cc - cc) = (\epsilon^{c}_{l})^2 \cdot [2\epsilon^{c}_{t} - (\epsilon^{c}_{t})^2] \,, \tag{5.27}$$

$$\epsilon^{z}_{ele}(cc - ec) = \epsilon^{c}_{l} \cdot \epsilon^{e}_{l} \cdot (\epsilon^{c}_{t} + \epsilon^{e}_{t} - \epsilon^{c}_{t} \cdot \epsilon^{e}_{t}) \,, \tag{5.28}$$

$$\epsilon^{z}_{ele}(ec - ec) = (\epsilon^{e}_{l})^2 \cdot [2\epsilon^{e}_{t} - (\epsilon^{e}_{t})^2] \,, \tag{5.29}$$

where ϵ^{c}_{l} and ϵ^{c}_{t} are the loose and tight selection efficiencies for central electrons, and ϵ^{e}_{l} and ϵ^{e}_{t} are the corresponding efficiencies for forward electrons. The Z electron selection efficiencies are calculated for each background subtraction method using the efficiencies in Tables 5.3 and 5.4. Using method D to quote the central

values of the efficiencies, and assigning the systematic error as half the maximum difference between the four methods, the Z electron selection efficiencies are:

$$\epsilon^z_{ele}(cc-cc) = 0.7950 \pm 0.0066 \pm 0.0093 \ , \tag{5.30}$$

$$\epsilon^z_{ele}(cc-ec) = 0.7482 \pm 0.0066 \pm 0.0081 \ , \tag{5.31}$$

$$\epsilon^z_{ele}(ec-ec) = 0.7028 \pm 0.0105 \pm 0.0072 \ . \tag{5.32}$$

To calculate the overall Z electron selection efficiency, the CC-CC, CC-EC and EC-EC results are combined based on their relative acceptance fractions, with care taken to properly handle the correlation in the error calculation. The relative acceptances are obtained from the CMS Monte Carlo, and are 49.69% for CC-CC, 40.55% for CC-EC, and 9.76% for EC-EC. This gives

$$\epsilon^z_{ele} = 0.7670 \pm 0.0106 \ . \tag{5.33}$$

The quoted error combines the statistical and systematic errors in quadrature.

The total Z selection efficiency is obtained by combining the electron selection efficiency with the Level-Ø efficiency and dividing by 1.017 to correct for the tracking efficiency (see Section 5.1.3):

$$\epsilon^z_{tot} = \epsilon_{\mathrm{L\emptyset}} \cdot \epsilon^z_{ele} = 0.7436 \pm 0.0111 \ . \tag{5.34}$$

5.5 Efficiency Ratio

The primary concern of this analysis is an accurate measurement of the cross section ratio of W and Z electronic decays. A large portion of the systematic error in the efficiency ratio cancels, since the W and Z electron efficiencies are

correlated[1]. This correlation is taken into account by a simple Monte Carlo program. This program correlates the loose and tight efficiencies by using one single random number in deciding if an electron passes the loose, the tight, or both requirements simultaneously according to the true loose and tight efficiencies. From this, the W and Z boson efficiencies and their ratio are computed. An ensemble of 10000 such experiments is repeated, and the distribution of all efficiencies are fitted to gaussians. The central value of the efficiencies is obtained from the mean of the gaussian, and the error from its width. The computation of the efficiency ratio is performed for each of the background subtraction methods: the central value is again chosen to be the one from method D, while the systematic error is taken to be half the maximum difference between the various methods. The efficiency ratio is measured to be:

$$\frac{\epsilon^w}{\epsilon^z} = 1.108 \pm 0.006 \pm 0.003 = 1.108 \pm 0.007 \,. \tag{5.35}$$

5.6 Diffractive Production of Weak Bosons

Diffractive production of W and Z bosons at the Tevatron occurs when the incident p or $\overline{p}$ escapes intact, losing a small fraction of its initial forward momentum. Our cross section measurements include both diffractive and non-diffractive W and Z boson production. The perturbative theoretical calculation of Ref. [15] does not include an explicit calculation of diffraction, but diffraction contributions to the total cross sections enter through the parton distribution functions. A recent measurement [68] reports the diffractive to non-diffractive W produc-

[1] The efficiency of the Level-Ø system and the effect of correlations in the tracking efficiency cancel completely.

tion ratio to be $(1.15 \pm 0.55)\%$. No such measurement exists to date for Z bosons, although it is believed that diffractive Z production exists at roughly the same level. Recent theoretical calculations suggest that the ratio of diffractive W to Z cross sections is roughly the same as the ratio of inclusive cross sections (see Table V of Ref. [69]). Since the Level-Ø trigger requires simultaneous hits on the forward and backward scintillation counters, such events would not pass our selection unless accompanied by a minimum bias interaction. The Level-Ø trigger efficiency is calculated from W events without a Level-Ø requirement, and no correction is made to subtract diffractive W bosons, so in practice we account for all diffractive W bosons produced. The same efficiency is used for Z events under the assumption that the underlying events in W and Z boson production are essentially identical. In order to have an appreciable effect on $\mathcal{R}$, the diffractive production of Z bosons would have to be several times larger than that observed for W bosons, so we may safely neglect the effect on $\mathcal{R}$.

Chapter 6

Backgrounds

Events other than $W \to e\nu$ or $Z \to ee$ can sometimes pass the W or Z selection criteria and contaminate the data samples. These background events can be physical or instrumental. Physical backgrounds are the result of other physical processes with a final state which is indistinguishable from the one under study. An example is the decay $W \to \tau\nu$, where the tau subsequently decays into an electron and two neutrinos, giving an electron plus $\not{E}_T$ in the final state. Instrumental backgrounds are the result of physical processes with final states different from the one under study, but which are misidentified by the detector. For example, QCD events in which two jets are misidentified as electrons can mimic a $Z \to ee$ signature. The event selection cuts are designed to accept a large fraction of $W \to e\nu$ and $Z \to ee$ events while rejecting as much background as possible. Since it is desirable to have a large sample of signal events in order to reduce statistical and even systematic uncertainties, these cuts represent a compromise between retaining high efficiency and reducing the background, and as a result a small amount of background contamination is unavoidable. This does not present a problem in itself, since the cross sections can be measured

accurately as long as one has a good understanding of the amount of background present in each sample.

6.1 Backgrounds in the $W \to e\nu$ Sample

There are several sources of instrumental and physical backgrounds which can contaminate the $W \to e\nu$ sample. The largest source of background, usually referred to as QCD background, comes from multi-jet, b-quark, and direct photon sources. A QCD jet fluctuates electromagnetically and mimics the electron, while another jet is mismeasured giving rise to missing transverse energy. Other background sources are $W \to \tau\nu$ and $Z \to \tau\tau$ events where a tau decays into an electron and two neutrinos, and $Z \to ee$ events where one electron is lost in a poorly instrumented region of the detector, giving rise to $\not\!\!E_T$.

6.1.1 Backgrounds from multi-jet, b-quark, and direct photon sources

The fraction of QCD background events in the $W \to e\nu$ sample is calculated using a data-based method, by comparing the number of events in the $W \to e\nu$ sample to that of a sample with the same kinematic requirements, but with loosened or tightened electron identification requirements. We start with a relatively loose sample of M $W \to e\nu$ events which are obtained with a minimal set of cuts. We call this the *parent* sample. We then impose a set of tighter cuts, and obtain two subsamples: a *child* subsample containing P events which passed the tight cuts, and a subsample containing F events which failed. We can also think of the parent sample as being divided into two other subsamples: one containing

R real $W \to e\nu$ events, and another containing B background events. Of course, we do not know R and B, since these are precisely the numbers we want to measure, but they are related to P and F by

$$\begin{pmatrix} P \\ F \end{pmatrix} = \begin{pmatrix} \epsilon_s & \epsilon_b \\ 1-\epsilon_s & 1-\epsilon_b \end{pmatrix} \begin{pmatrix} R \\ B \end{pmatrix} , \tag{6.1}$$

where ϵ_s is the efficiency of the tight cuts (relative to the loose cuts of the parent sample) on real $W \to e\nu$ events (signal efficiency), and ϵ_b is the efficiency of the tight cuts on background events (background efficiency). There are two additional constraints from the conservation of the total number of events in the parent sample:

$$M = P + F \qquad \text{and} \qquad M = R + B \; . \tag{6.2}$$

The QCD background fraction in the child sample is the number of background events which pass the tight cuts divided by the total number of events which pass the tight cuts:

$$f^W_{QCD} = \frac{\epsilon_b B}{P} \; . \tag{6.3}$$

We know P and F, so if we can measure ϵ_s and ϵ_b the problem reduces to solving Equation 6.1 for R and B. This is just inverting the 2×2 matrix:

$$\begin{pmatrix} R \\ B \end{pmatrix} = \frac{1}{\epsilon_s - \epsilon_b} \begin{pmatrix} 1-\epsilon_b & -\epsilon_b \\ -(1-\epsilon_s) & \epsilon_s \end{pmatrix} \begin{pmatrix} P \\ M-P \end{pmatrix} \; . \tag{6.4}$$

The matrix is invertible as long as its determinant $\epsilon_s - \epsilon_b$ is not identically zero, which is certainly the case since the the electron identification criteria was constructed in such a way as to keep most genuine electrons and to reject most background sources ($\epsilon_s > \epsilon_b$). From Equation 6.4, the expression for B is:

$$B = \frac{\epsilon_s M - P}{\epsilon_s - \epsilon_b} \; , \tag{6.5}$$

which, upon substitution into Equation 6.3, yields the expression for the background fraction:

$$f_{QCD}^{W} = \frac{\epsilon_b}{P} \cdot \frac{\epsilon_s\, M - P}{\epsilon_s - \epsilon_b} \ . \tag{6.6}$$

The efficiency ϵ_s is obtained by using the method described in Chapter 5. To measure ϵ_b, we use data samples obtained using the same criteria as for the parent and child samples, except requiring small $\not\!\!E_T$ in the event instead of large $\not\!\!E_T$ (to remove W boson events). This assumes that at low $\not\!\!E_T$ most events are background, with very little contribution from W boson events. We check the validity of this assumption by looking at the $\not\!\!E_T$ distribution of the child and parent samples and comparing it to the $\not\!\!E_T$ distribution from $W \to e\nu$ and $W \to \tau\nu \to e\nu\overline{\nu}\nu$ Monte Carlo events. Figure 6.1 shows the case where the parent background sample corresponds to the nominal W selection (except for the $\not\!\!E_T$ requirement), and the child sample is obtained using an additional dE/dx cut which requires the track of the electron candidate to have an ionization consistent with that of one electron. The Monte Carlo (CMS) distribution is normalized to the child sample distribution in the high $\not\!\!E_T$ region, which is dominated by real W events. The fraction of W boson events in the low $\not\!\!E_T$ region is found to be negligible.

One source of systematic uncertainty is from the assumption that background sources in events with small $\not\!\!E_T$ have the same value for ϵ_b as those with $\not\!\!E_T > 25$ GeV. Most of the identification requirements are calorimeter-based and can, in principle, be correlated with $\not\!\!E_T$. However, the f_{QCD}^{W} measurement obtained by adding the tracking-based dE/dx requirement yields results consistent with the calorimeter-based methods, giving us confidence that the correlations between $\not\!\!E_T$ and ϵ_b are small. We do an additional check on the uncertainty due to

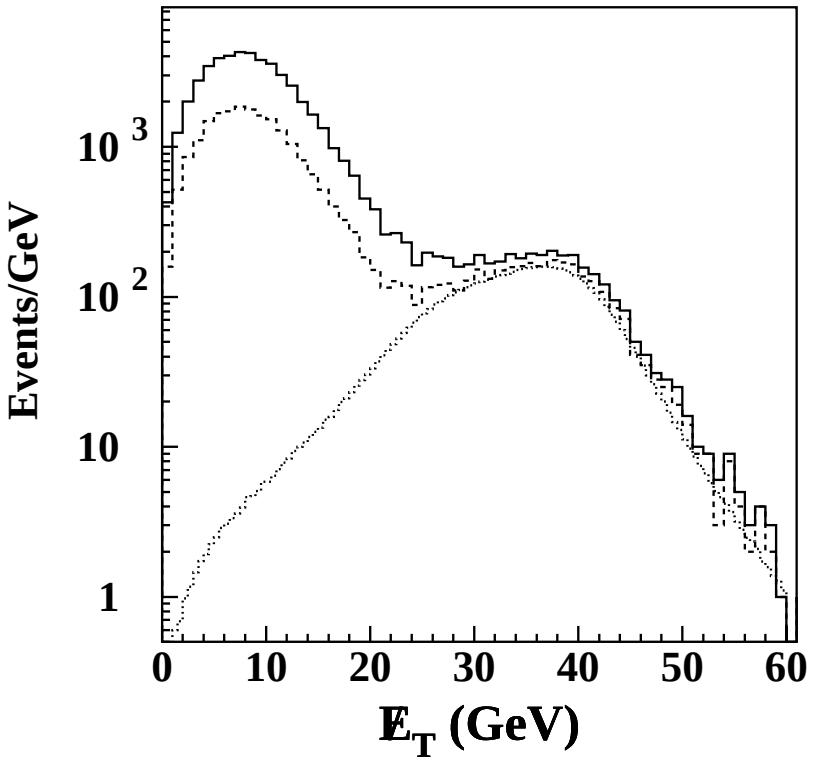

Figure 6.1: The $\not\!\!E_T$ distribution for a particular choice of parent and child inclusive electron samples. The solid line is the parent sample corresponding to the nominal W selection cuts except for $\not\!\!E_T$. The dashed line is the child sample, corresponding to nominal cuts and the additional dE/dx requirement. The dot-dash line is the sum of $W \to e\nu$ and $W \to \tau\nu \to e\nu\overline{\nu}\nu$ from Monte Carlo. There is negligible W contribution in the low (< 15 GeV) $\not\!\!E_T$ background regions.

a possible $\not\!\!E_T$ dependence of ϵ_b by varying the $\not\!\!E_T$ cutoff used to define the background sample. We use the $\not\!\!E_T$ range [0–15] GeV for the central value and the ranges [0–5], [0–10], and [10–15] GeV to evaluate the systematic uncertainty on ϵ_b.

A source of systematic uncertainty on f_{QCD} comes from the particular choice of parent/child samples used. We evaluate this uncertainty by using different parent and child requirements. We define the different parent and child samples by varying the shower shape, isolation, and electromagnetic fraction requirements and by tightening the selection by requiring the dE/dx measured in the tracking system to be consistent with that of an electron. Tables 6.1 and 6.2 show the results in the CC and EC respectively.

The uncertainty on the background fraction for any particular choice of parent and child samples is dominated by the uncertainties on ϵ_s and ϵ_b, and is given approximately by

$$\delta f^W_{QCD} \approx \frac{\epsilon_s}{\epsilon_s - \epsilon_b}\delta\epsilon_s \oplus \frac{\epsilon_b f^W_{QCD}}{\epsilon_s - \epsilon_b}\delta\epsilon_b. \tag{6.7}$$

From this equation, one can see that the method works best when $\epsilon_s - \epsilon_b$ is large, and produces large errors when this difference is small. This is to be expected: the method works best when the cuts have high efficiency for signal and high background rejection.

We take Gaussian distributions (normalized to unity) with the mean and uncertainty corresponding to each background fraction in Tables 6.1 and 6.2. For the mean value of f^W_{QCD} in each topology, we add all the CC or EC distributions and take the median of the resulting distribution. We set the systematic uncertainty in f^W_{QCD} from the symmetric band around the median with an area of 68% of the total distribution. The results are $f^{WCC}_{QCD} = 0.046 \pm 0.014$ for CC events,

Table 6.1: The fraction of the $W \to e\nu$ events in the CC that come from multi-jet, b-quark, and direct photon sources, f_{QCD}^{WCC}. In this table, $f_{\rm iso}$ refers to the electron isolation requirement, $f_{\rm em}$ to the electromagnetic fraction requirement, $\chi^2_{\rm hm}$ refers to the shower shape requirement, nominal means the electron ID used in the $W \to e\nu$ sample ($\chi^2_{\rm hm}$<100, $f_{\rm iso}$<0.15, and $f_{\rm em}$> 0.95, see Chapter 3). dE/dx means the matching track was required to have $dE/dx < 1.4$ or $dE/dx > 3.0$ for CDC tracks and $dE/dx < 1.3$ or $dE/dx > 2.5$ for FDC tracks, in order to reject photon conversions (see Ref. [70]).

Parent cuts	Child Cuts	ϵ_s	ϵ_b	f_{QCD}^{WCC} [%]
nominal	$+dE/dx$	0.933 ± 0.004	0.372 ± 0.023	3.39±0.9
$f_{\rm iso}(0.15)$,$f_{\rm em}(0.95)$	nominal	0.952 ± 0.003	0.686 ± 0.017	4.49±1.0
$f_{\rm em}(0.95)$	nominal	0.949 ± 0.003	0.650 ± 0.011	4.41±0.8
$f_{\rm em}(0.9)$	nominal	0.941 ± 0.004	0.573 ± 0.015	4.46±0.8
$f_{\rm em}(0.9)$,$f_{\rm iso}(0.15)$	nominal	0.945 ± 0.004	0.621 ± 0.016	4.76±0.8
$f_{\rm em}(0.9)$,$\chi^2_{\rm hm}(100)$	nominal	0.989 ± 0.003	0.872 ± 0.007	6.16±2.0
$f_{\rm iso}(0.15)$,$\chi^2_{\rm hm}(100)$	nominal	0.992 ± 0.002	0.934 ± 0.007	6.96±3.0

and $f_{QCD}^{WEC} = 0.143 \pm 0.043$ for EC events. To obtain the combined background fraction, we combine the CC and EC W cross sections. The weights for CC and EC events are taken as $1/\delta_u^2$, where δ_u is the total uncorrelated error for each individual cross section, and where we make the conservative assumption that there is maximal correlation between the CC and EC uncertainties (i.e., the correlated part for each uncertainty is the smaller of the two uncertainties). We then find the background fraction that corresponds to this combined W cross section. The combined background fraction is estimated to be $f_{QCD}^{W} = 0.064 \pm 0.014$.

Table 6.2: The fraction of the $W \to e\nu$ events in the EC that come from multi-jet, b-quark, and direct photon sources, f_{QCD}^{WEC}. In this table, $f_{\rm iso}$ refers to the electron isolation requirement, $f_{\rm em}$ to the electromagnetic fraction requirement, $\chi^2_{\rm hm}$ refers to the shower shape requirement, nominal means the electron ID used in the $W \to e\nu$ sample ($\chi^2_{\rm hm}$<100, $f_{\rm iso}$<0.15, and $f_{\rm em}$> 0.95, see Chapter 3). dE/dx means the matching track was required to have $dE/dx < 1.4$ or $dE/dx > 3.0$ for CDC tracks and $dE/dx < 1.3$ or $dE/dx > 2.5$ for FDC tracks (see Ref. [70]).

Parent cuts	Child Cuts	ϵ_s	ϵ_b	f_{QCD}^{WEC} [%]
nominal	$+dE/dx$	0.759 ± 0.010	0.552 ± 0.007	14.60±4.5
$f_{\rm iso}(0.15)$,$f_{\rm em}(0.95)$	nominal	0.881 ± 0.009	0.513 ± 0.016	11.03±1.5
$f_{\rm em}(0.95)$	nominal	0.880 ± 0.009	0.492 ± 0.015	11.44±1.2
$f_{\rm em}(0.9)$	nominal	0.868 ± 0.010	0.367 ± 0.015	14.48±1.2
$f_{\rm em}(0.9)$,$f_{\rm iso}(0.15)$	nominal	0.868 ± 0.009	0.398 ± 0.017	14.13±1.4
$f_{\rm em}(0.9)$,$\chi^2_{\rm hm}(100)$	nominal	0.987 ± 0.004	0.858 ± 0.013	19.99±3.3
$f_{\rm iso}(0.15)$,$\chi^2_{\rm hm}(100)$	nominal	0.991 ± 0.003	0.897 ± 0.010	21.94±3.8

6.1.2 $W \to \tau\nu$ Background

The backgrounds to the $W \to e\nu$ sample from the decay $W \to \tau\nu$, where the τ subsequently decays into $e\nu\nu$, is calculated using the same production and decay model (CMS) as in the acceptance calculation. The τ-leptons are forced to decay electronically, and then the event is smeared. Electrons from $\tau \to e\nu\nu$ decays are usually much softer than electrons from W decays. Figure 6.2 shows the E_T distribution for such electrons. Instead of a Jacobian peak at $M_W/2$, the distribution peaks at low E_T and falls off rapidly.

This background is expected to be small, since the acceptance for $W \to \tau\nu$

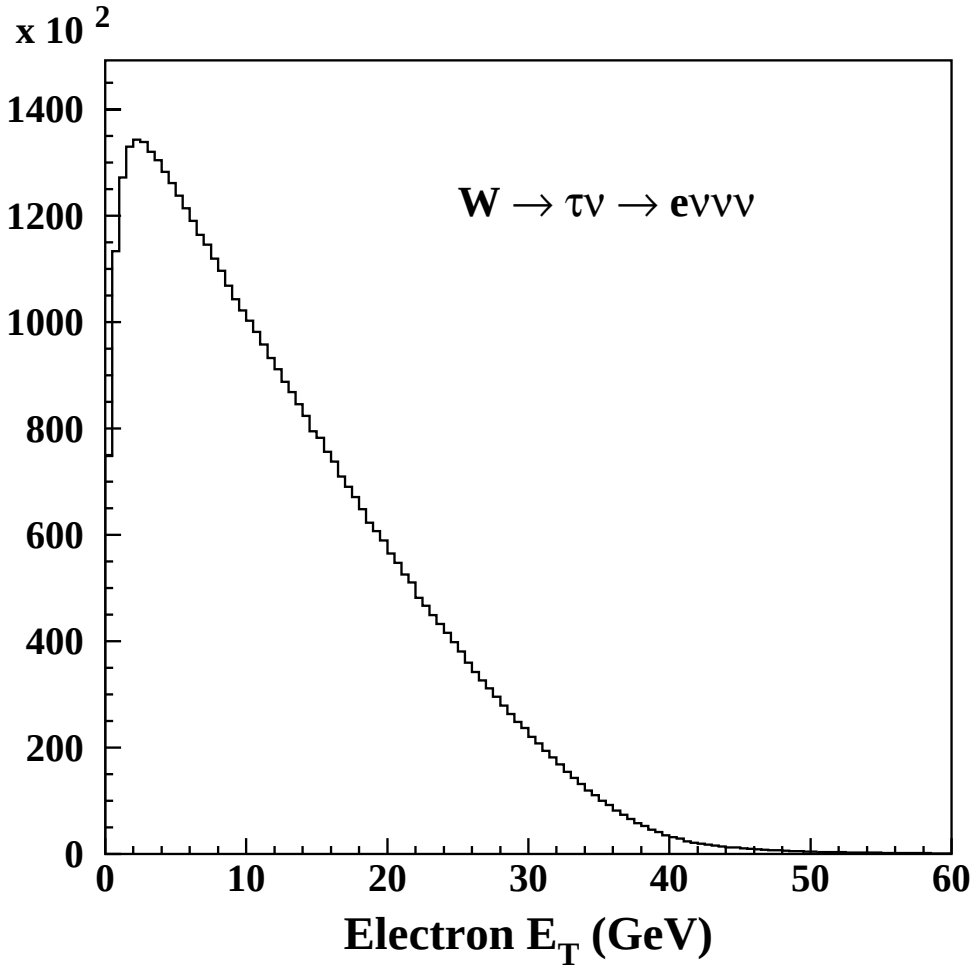

Figure 6.2: Electron E_T distribution for $W \to \tau\nu \to e\nu\nu\nu$ events.

events is reduced by the $\tau \to e\nu\nu$ branching fraction of $\approx 18\%$, and the kinematic acceptance is greatly reduced by the $E_T > 25$ GeV cut. The $W \to e\nu$ cross section is calculated as

$$\sigma_{W\to e\nu} = \frac{N_{\rm obs} - {\rm QCD} - N_Z^W - N_{W\tau\nu}}{A_W \cdot \epsilon \cdot \mathcal{L}} \ , \tag{6.8}$$

where A_W is the acceptance for $W \to e\nu$ events. Assuming lepton universality (which predicts that all leptons couple with equal strength to the weak bosons,

and therefore that $\sigma_{W\to e\nu} = \sigma_{W\to\tau\nu}$), and the fact that we do not observe any dependence of the lepton identification efficiency on the transverse energy of the lepton, we can write

$$N_{W\tau\nu} = \sigma_{W\to\tau\nu} \cdot A^W_{W\tau} \cdot \epsilon \cdot \mathcal{L} = \sigma_{W\to e\nu} \cdot A^W_{W\tau} \cdot \epsilon \cdot \mathcal{L} \ , \tag{6.9}$$

where $A^W_{W\tau}$ is the acceptance for $W \to \tau\nu$ events to pass the $W \to e\nu$ kinematic and fiducial requirements multiplied times $B(\tau \to e\nu\nu) = 0.1783$. Substituting Equation 6.9 into Equation 6.8 yields

$$\sigma_{W\to e\nu} = \frac{N_{\text{obs}} - \text{QCD} - N^W_Z}{A_W \cdot (1 + \frac{A^W_{W\tau}}{A_W}) \cdot \epsilon \cdot \mathcal{L}} \ . \tag{6.10}$$

We can therefore account for the τ backgrounds in the W boson sample by making a correction to the W boson acceptance of $(1 + \frac{A^W_{W\tau}}{A_W}) = 1.021 \pm 0.002$.

6.1.3 $Z \to ee$ and $Z \to \tau\tau$ Backgrounds

A $Z \to ee$ event can be misidentified as a $W \to e\nu$ event when one of the electrons fails the fiducial requirements, or is misidentified as a jet, and the transverse energy in the event is substantially mismeasured, yielding a large apparent $\not{E}_T$. In a similar manner, $Z \to \tau\tau$ events can mimic $W \to e\nu$ events. The $Z \to ee$ and $Z \to \tau\tau$ backgrounds are estimated using a GEANT-based [48] simulation of the detector, with HERWIG [64] to generate both $Z \to ee$ and $Z \to \tau\tau$ events. The number of Z background events in the $W \to e\nu$ sample is estimated by

$$N^W_Z = \epsilon_W \cdot N^Z_{obs}(1 - f^Z_{QCD}) \cdot \frac{A^W_{Zee} + A^W_{Z\tau}}{A_Z \cdot \epsilon_Z} \tag{6.11}$$

where A^W_{Zee} is the fraction of $Z \to ee$ events that passes the $W \to e\nu$ selection criteria, $A^W_{Z\tau}$ is the fraction of $Z \to \tau\tau$ events that passes the $W \to e\nu$ selection

criteria multiplied times the probability that at least one of the taus decays to an electron, $2B - B^2$, where $B = B(\tau \to e\nu\nu) = 0.1783$, N^Z_{obs} is the number of candidate $Z \to ee$ events, f^Z_{QCD} is the fraction of these candidates from multi-jet, b-quark, and direct photon background sources, ϵ_Z is the electron identification efficiency for $Z \to ee$ events, and A_Z is the geometric and kinematic acceptance for $Z \to ee$ events. The ratio $(A^W_{Zee} + A^W_{Z\tau})/A_Z$ is found to be 0.133 ± 0.034, and thus a total of 621 ± 155 Z events are expected to pass our $W \to e\nu$ selection. The uncertainty in this estimate has two main components: the difference between the electron identification efficiency in the simulation and in the data, and the effect of any additional overlapping minimum-bias events. This uncertainty has a negligible effect on the overall uncertainty in the W cross section and the ratio $\mathcal{R}$.

6.2 Backgrounds in the $Z \to ee$ Sample

Although the signature of two isolated, high E_T electrons is quite unique, there are sources of instrumental and physics backgrounds which contaminate the $Z \to ee$ sample. The largest source of background is again QCD multijets, where the jets fluctuate electromagnetically and fake electrons. In addition, there are physics backgrounds from Drell-Yan and $Z \to \tau\tau$ events where the taus decay into electrons.

6.2.1 Backgrounds from multi-jet, b-quark, and direct photon sources

For $Z \to ee$ events one can reconstruct the dielectron invariant mass, which gives a sharp Breit-Wigner peak, making it easier to separate the signal from the background. The background fraction for the $Z \to ee$ sample due to multi-jet, b-quark, and direct photon sources is determined by fitting the dielectron invariant mass distribution to a linear combination of a signal shape, obtained from Z/γ^* events generated with PYTHIA and processed through the detector simulation, and a background shape determined from data. Different mass distributions from different sources, such as multi-jet events, direct photon candidates, and events passing all of the $Z \to ee$ kinematic cutoffs, but failing the electron identification requirements, are used for background shapes. Figure 6.3 shows such fits with a background shape determined from direct photon data, for the case where both electrons are in the CC, for the case where one electron is in the CC and the other in the EC, for the case where both electrons are in the EC, and for the inclusive $Z \to ee$ sample. Systematic uncertainties are determined from the range of values obtained using the different background shapes, and also by varying the range of invariant masses used in the fit. The result is $f^Z_{QCD} = 0.045 \pm 0.005$.

6.2.2 Drell-Yan and Z/γ^* Interference

It is conventional to report $\sigma(p\overline{p} \to Z + X) \cdot B(Z \to ee)$ as the product of the cross section and branching fraction, assuming the Z boson is the only source of dielectron events. However, the production of dielectron events is properly described by considering the Z boson, the photon propagator, and the inter-

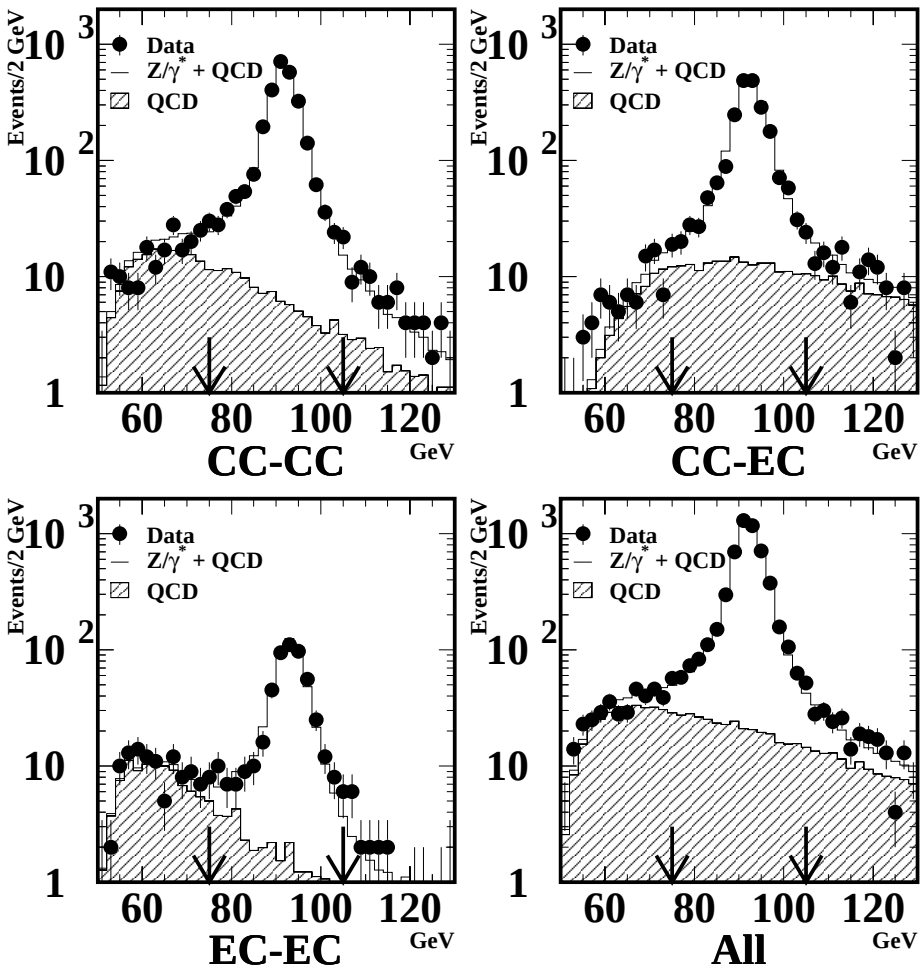

Figure 6.3: Fit of the $Z \rightarrow ee$ invariant mass distribution for the different topologies. The shaded histogram is the background shape obtained from direct photon data, and the dots are the $Z \rightarrow ee$ candidates. The solid line histogram results from fitting the data to a linear combination of the Drell-Yan signal shape from PYTHIA and the background shape.

ference between the two: $p\bar{p} \to Z/\gamma^* \to ee$. The Drell-Yan correction factor relates the number of events in our mass window to what would be expected purely from Z boson production. To obtain this correction, we use PYTHIA to generate events with just the contribution from the Z boson, and, separately, using the full Drell-Yan process with interference terms (combining Z and photon diagrams). We process both samples with the same Monte Carlo simulation used for the acceptance calculation (CMS). The ratio of the complete Drell-Yan cross section (σ_{DY}) to the cross section for the Z alone (σ_Z), for events passing our $Z \to ee$ selection criteria, is estimated to be

$$\sigma_{DY}/\sigma_Z = \frac{1}{1 - f_{DY}} = 1.012 \pm 0.001 \,, \tag{6.12}$$

or $f_{DY} = 0.012 \pm 0.001$ as the fraction of production cross section attributable to the presence of the photon propagator. The systematic uncertainty is evaluated by using the ISAJET [71] generator instead of PYTHIA and is estimated as the difference between the two generators. The dominant uncertainty is due to Monte Carlo statistics, but its effect is negligible compared to the dominant uncertainties.

6.2.3 $Z \to \tau\tau$

The final source of background comes from the $Z \to \tau\tau$ process, where both taus decay electronically. The decay rate of Z bosons into taus is identical to its decay rate to electrons[1]. However the combination of a soft electron E_T spectrum and the additional factor of $B(\tau \to e\nu\nu)^2$ make this background negligible. This is verified by generating 900 ISAJET $Z \to \tau\tau \to e\nu\nu e\nu\nu$ events, and passing

[1] Assuming lepton universality.

them through GEANT and DØRECO. After the geometric and kinematic cuts are imposed, 17 events survive. The invariant mass window cut ($75 < M_{ee} < 105$ GeV) reduces the sample to one single event. Taking into consideration the $(18\%)^2$ branching ratio factors, the acceptance of $Z \to \tau\tau$ is indeed found to be negligible, and this source of background can be safely neglected.

Chapter 7

Luminosity

A precise value of the integrated luminosity is needed for determining any absolute cross section. This analysis uses data collected at $\sqrt{s} = 1.8$ TeV during the 1994–1995 running of the Fermilab Tevatron. The measurement of luminosity is described in detail in Ref. [44], and this chapter will only present the results. Luminosity measurements are stored periodically (every minute) and then integrated over the live running time. This one-minute period is much shorter than the time it takes for the luminosity to change significantly. The counting rate $R_{L\emptyset}$ of the LØ counters is given by

$$R_{L\emptyset} = L\sigma_{L\emptyset} \tag{7.1}$$

where L is the instantaneous luminosity and $\sigma_{L\emptyset}$ is the effective $p\overline{p}$ cross section subtended by the LØ counters. Equation 7.1 yields the correct luminosity if the counting rate is the same as the interaction rate, which is the case at low luminosities. However, at higher luminosities the probability for multiple interactions per crossing increases, and the LØ counters do not distinguish between crossings with one or with multiple interactions. As a result, the linear relationship between L and $R_{L\emptyset}$ breaks down and we need to take multiple interactions

into account to calculate the luminosity. The average number of interactions per beam crossing, μ, is given by

$$\mu = L\tau\sigma_{L\emptyset} \tag{7.2}$$

where $\tau = 3.5$ μs is the time between beam crossings. The probability P_n of having n interactions in one crossing at a given luminosity is given by Poisson statistics:

$$P_n = \frac{\mu^n}{n!}e^{-\mu} \tag{7.3}$$

Since the counting rate does not distinguish between one or more interactions, it is given by the probability of having one or more interactions per crossing divided by the time between crossings:

$$R_{L\emptyset} = \frac{P_{n\geq 1}}{\tau} = \frac{1 - P_0}{\tau} = \frac{1 - e^{-\mu}}{\tau} \tag{7.4}$$

Solving for μ and using Equation 7.2 gives

$$L = \frac{-\ln(1 - \tau R_{L\emptyset})}{\tau\sigma_{L\emptyset}} \tag{7.5}$$

$R_{L\emptyset}$ is defined by the counts observed in six trigger scalers, one for each beam bunch, divided by the fixed time between crossings. This counting rate never saturated during the run, not even at the highest luminosities. The value of $\sigma_{L\emptyset}$ is obtained from

$$\sigma_{L\emptyset} = \epsilon_{L\emptyset}^{p\overline{p}}(A_{sd}\sigma_{sd} + A_{dd}\sigma_{dd} + A_{nd}\sigma_{nd}) \tag{7.6}$$

where we use the single diffractive (σ_{sd}), double diffractive (σ_{dd}), and non diffractive (σ_{nd}) components of the total inelastic $p\overline{p}$ cross section from a "world average" of the results from CDF [72], E710 [74], and E811 [75]; the LØ trigger efficiency $\epsilon_{L\emptyset}^{p\overline{p}}$ is determined using samples of data collected from triggers on

random beam crossings; and the different LØ acceptances (A_{sd}, A_{dd}, A_{nd}) are obtained from Monte Carlo studies. Table 7.1 shows the inputs to our calculation of $\sigma_{L\emptyset}$.

Table 7.1: Values used in the $\sigma_{L\emptyset}$ calculation; SD, DD and ND refer to single diffractive, double diffractive, and non diffractive, respectively.

SD Acceptance (A_{sd})	15.1% ± 5.5%
DD Acceptance (A_{dd})	71.6% ± 3.3%
ND Acceptance (A_{nd})	97.1% ± 2.0%
LØ Trigger Efficiency ($\epsilon_{L\emptyset}^{p\overline{p}}$)	91% ± 2%
SD Cross Section (σ_{sd})	9.54 mb ± 0.43 mb
DD Cross Section (σ_{dd})	1.29 mb ± 0.20 mb
ND Cross Section (σ_{nd})	46.56 mb ± 1.63 mb
$\sigma_{L\emptyset}$	43.1 mb ± 1.9 mb

Luminosities during the 1994–1995 running period ranged from 2–20 $\times 10^{30}$ cm^{-2}s^{-1}. The average luminosity for the $W \to e\nu$ and $Z \to ee$ data samples is 7.5×10^{30} cm^{-2}s^{-1}, with an average of 1.6 interactions per beam crossing. The integrated luminosity for the $Z \to ee$ and $W \to e\nu$ data samples is

$$\mathcal{L} = \int L \cdot dt = 84.5 \pm 3.6 \text{ pb}^{-1} . \tag{7.7}$$

The uncertainty in luminosity is the dominant uncertainty in the measurement of W and Z boson cross sections. Figure 7.1 shows the distribution in luminosity at the time of recording of the $W \to e\nu$ and $Z \to ee$ candidates.

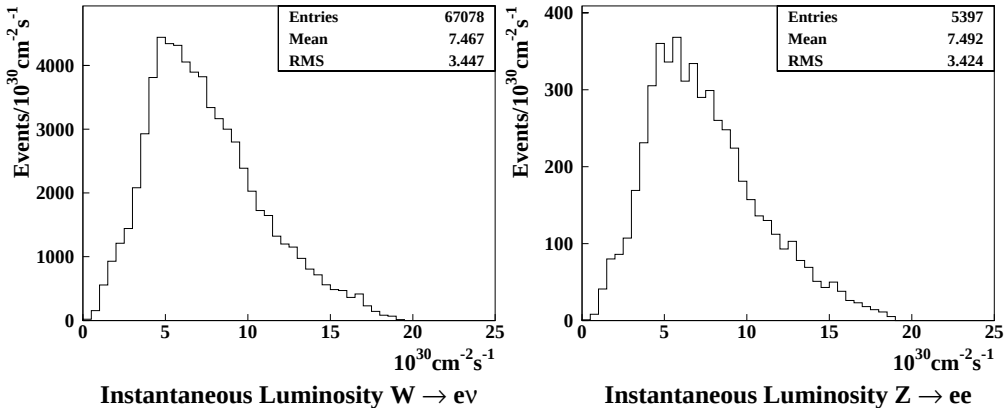

Figure 7.1: Distribution in luminosity for $W \to e\nu$ or $Z \to ee$ candidates. The mean and RMS values of the distributions are consistent with each other.

It should be noted that CDF[1] and previous DØ measurements used different normalizations for luminosity. The CDF Collaboration bases its luminosity purely on its own measurement of the inelastic $p\overline{p}$ cross section [72, 73]. As a result, current luminosities used by CDF are 6.2% lower than those used by DØ, and consequently all DØ cross sections are normalized 6.2% lower than all CDF cross sections. Previous DØ measurements relied only on results from CDF and E710. Including the recent E811 measurement of the inelastic $p\overline{p}$ cross section in the world average increased the discrepancy in normalization relative to CDF from 3.0% to 6.2% (i.e., current values are 3.2% higher than previous DØ measurements). The luminosity measurement used by DØ prior to the E811 result is described more extensively in Ref. [76].

[1]The other collider detector at the Fermilab Tevatron

Chapter 8

Results and Conclusions

8.1 Cross Section Measurements

The product of the W cross section and the branching fraction for $W \to e\nu$ is estimated using the relation

$$\sigma(p\overline{p} \to W{+}X){\cdot}B(W \to e\nu) = \frac{N^W_{obs} \cdot \left(1 - f^W_{QCD}\right) - \epsilon_W \cdot N^Z_{obs}(1 - f^Z_{QCD}) \cdot \frac{A^W_{Zee} + A^W_{Z\tau}}{A_Z \cdot \epsilon_Z}}{\epsilon_W \cdot A_W \cdot \left(1 + \frac{A^W_{W\tau}}{A_W}\right) \cdot \mathcal{L}} \tag{8.1}$$

where N^W_{obs} is the number of $W \to e\nu$ candidate events, f^W_{QCD} is the fraction of the $W \to e\nu$ candidate events that come from multi-jet, b-quark, and direct photon background sources, ϵ_W is the efficiency for $W \to e\nu$ events to pass W selection requirements, A_W is the geometric and kinematic acceptance for $W \to e\nu$, which includes effects from detector resolution, $A^W_{W\tau}$ is the fraction of $W \to \tau\nu$ events that pass the $W \to e\nu$ selection criteria, and $\mathcal{L} = \int L \cdot dt$ is the integrated luminosity of the data sample. N^W_Z corresponds to the number of Z boson events misidentified as W bosons, where one of the electrons from the Z boson decay enters an uninstrumented region of the detector or is otherwise undetected.

The product of the Z boson cross section and the branching fraction for $Z \to ee$ is determined from the relation

$$\sigma(p\overline{p} \to Z + X) \cdot B(Z \to ee) = \frac{N^Z_{obs} \cdot \left(1 - f^Z_{QCD}\right) \cdot (1 - f_{DY})}{\epsilon_Z \cdot A_Z \cdot \mathcal{L}} \tag{8.2}$$

where f_{DY} is a correction for the Drell-Yan contribution to Z-boson production. The ratio $\mathcal{R}$ can therefore be written as

$$\begin{aligned} \mathcal{R} &= \frac{\epsilon_Z}{\epsilon_W} \cdot \frac{A_Z}{A_W} \cdot \frac{1}{1 + \frac{A^W_{W\tau}}{A_W}} \cdot \frac{1}{1 - f^Z_{QCD}} \cdot \frac{1}{1 - f_{DY}} \\ &\times \left[\frac{N^W_{obs}}{N^Z_{obs}} \cdot \left(1 - f^W_{QCD}\right) - \epsilon_W \cdot \frac{(A^W_{Zee} + A^W_{Z\tau}) \cdot \left(1 - f^Z_{QCD}\right)}{A_Z \cdot \epsilon_Z}\right] \end{aligned} \tag{8.3}$$

The uncertainties on the individual cross sections are dominated by the uncertainty on the integrated luminosity measurement (4.3%). Tables 8.1 and 8.2 summarize the results for the individual cross sections.

The result for the $W \to e\nu$ cross section is

$$\sigma(p\overline{p} \to W + X) \cdot B(W \to e\nu) = 2310 \pm 10(\text{stat}) \pm 50(\text{syst}) \pm 100(\text{lum}) \text{ pb.} \tag{8.4}$$

The result for the $Z \to ee$ cross section is

$$\sigma(p\overline{p} \to Z + X) \cdot B(Z \to ee) = 221 \pm 3(\text{stat}) \pm 4(\text{syst}) \pm 10(\text{lum}) \text{ pb.} \tag{8.5}$$

Figure 8.1 shows a comparison between our results and a calculation of order α_s^2 using the program of Ref. [15] with the CTEQ4M structure functions, a Z boson mass of 91.188 GeV, a W boson mass of 80.375 GeV, and $\sin^2\theta_W$=0.2231. The DØ results in the muon channel [6] are from Run 1a(1992–1993), and have been multiplied by 0.969 for consistency with the new luminosity normalization (see Chapter 7). Figure 8.2 shows the Run 1b (1994–1995) results for the individual W and Z boson cross sections times electronic branching fraction and

Table 8.1: Values used in the $W \to e\nu$ cross section measurement.

$\sigma(p\overline{p} \to W + X) \cdot B(W \to e\nu)$	2310 ± 110 pb	
	Value	Uncertainty Contribution [pb]
N_{obs}^{W}	67078	10
ϵ_W	0.671 ± 0.009	30
A_W	0.465 ± 0.004	20
f_{QCD}^{W}	0.064 ± 0.014	35
$(A_{Zee}^{W} + A_{Z\tau}^{W})/A_Z$	0.133 ± 0.034	–
ϵ_Z	0.744 ± 0.011	–
f_{QCD}^{Z}	0.045 ± 0.005	–
N_Z^W	621 ± 155	6
$A_{W\tau}^{W}/A_W$	0.0211 ± 0.0021	5
$\mathcal{L}$	84.5 ± 3.6 pb^{-1}	100

the previous DØ results from Run 1a (1992–1993) [6] for both the electron and muon channels compared to the corresponding theoretical predictions. The Run 1a results are normalized to the new luminosity for consistency with Run 1b results.

Table 8.3 summarizes the result for the ratio of the cross sections, $\sigma(p\overline{p} \to W + X) \cdot B(W \to e\nu)/\sigma(p\overline{p} \to Z + X) \cdot B(Z \to ee)$. In the ratio, many of the systematic uncertainties, including the luminosity uncertainty, cancel. The uncertainty in $\mathcal{R}$ has five main components: the uncertainty in the multi-jet, b-quark, and direct photon backgrounds to the W boson (1.5%), the statistics of the Z boson sample (1.4%), the uncertainty in the ratio of the W and Z

Table 8.2: Values used in the $Z \to ee$ cross section measurement.

$\sigma(p\overline{p} \to Z + X) \cdot B(Z \to ee)$	221 ± 11 pb	
	Value	Uncertainty Contribution [pb]
N_{obs}^{Z}	5397	3
ϵ_Z	0.744 ± 0.011	3
A_Z	0.366 ± 0.003	2
f_{QCD}^{Z}	0.045 ± 0.005	1
f_{DY}	0.012 ± 0.001	< 1
$\mathcal{L}$	84.5 ± 3.6 pb^{-1}	10

boson acceptances (0.8%), the uncertainty in the ratio of the W and Z boson electron identification efficiencies (0.6%), and the uncertainty in the multi-jet, b-quark, and direct photon backgrounds to the Z (0.5%). In addition, we assign a 1% uncertainty in $\mathcal{R}$ due next-to-leading-order electroweak radiative corrections. The result is

$$\mathcal{R} = 10.43 \ \pm 0.15 \text{ (stat)} \pm 0.20 \text{ (syst)} \pm 0.10 \text{ (NLO)}. \tag{8.6}$$

8.2 Indirect Measurements

Using our results on $\sigma(p\overline{p} \to W + X) \cdot B(W \to e\nu) = 2310 \pm 10 \pm 50 \pm 100$ pb, $\sigma(p\overline{p} \to Z + X) \cdot B(Z \to ee) = 221 \pm 3 \pm 4 \pm 10$ pb, and $\mathcal{R} = 10.43 \ \pm 0.15 \ \pm 0.20 \pm 0.10$, we can determine the electronic branching fraction of the W boson via

$$B(W \to e\nu) = \mathcal{R} \cdot B(Z \to ee) \cdot \frac{\sigma_Z}{\sigma_W} \tag{8.7}$$

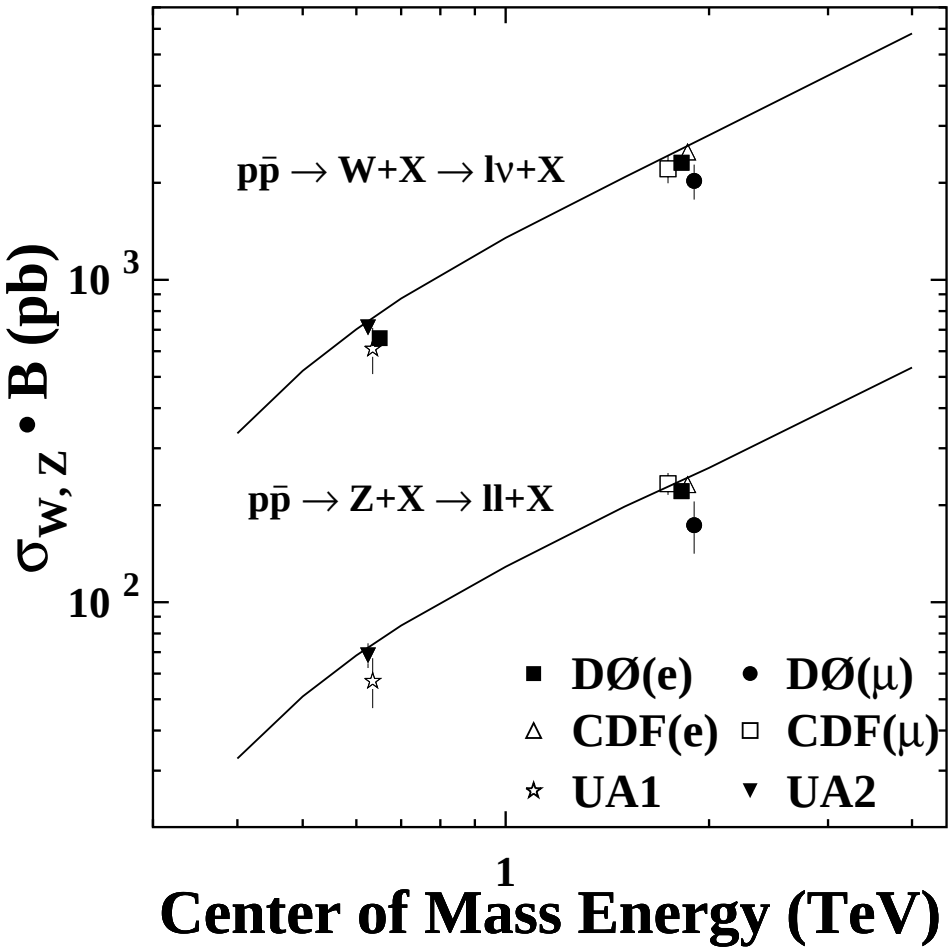

Figure 8.1: Comparison between measured and predicted cross sections, $\sigma(p\overline{p} \rightarrow W + X) \cdot B(W \rightarrow e\nu)$ and $\sigma(p\overline{p} \rightarrow Z + X) \cdot B(Z \rightarrow ee)$. The lines correspond to a theoretical calculation of order α_s^2 using the program of Ref. [15] with the CTEQ4M structure functions, a Z boson mass of 91.188 GeV, a W boson mass of 80.375 GeV, and $\sin^2\theta_W$=0.2231. The DØ results in the muon channel are from Ref. [6] normalized to the new LØ cross section.

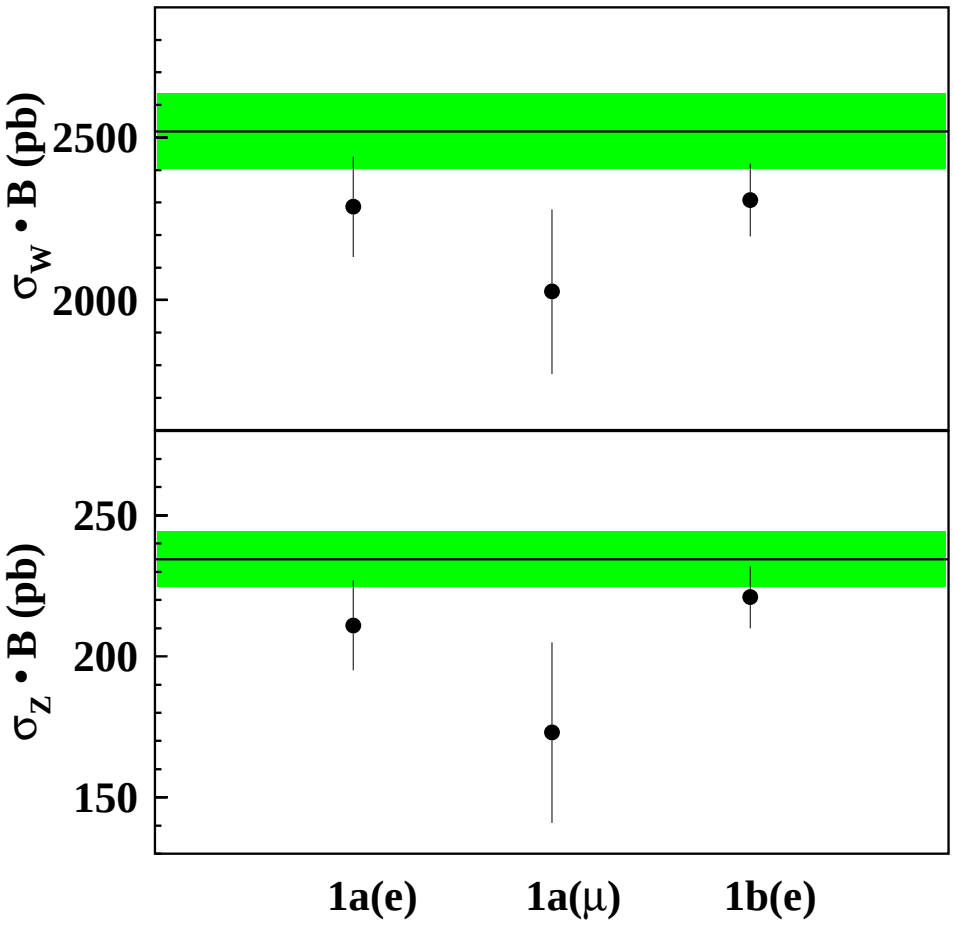

Figure 8.2: Run 1a (1992–1993) [6] and 1b (1994–1995) results for the W and Z boson cross sections times branching fractions. The line is the theoretical prediction from Ref. [15]. The central value uses $\Lambda_{\mathrm{QCD}} = 296$ MeV and the CTEQ4M structure functions. The shaded region shows the uncertainty in the prediction due to variations in α_s obtained by varying Λ_{QCD} between 213 MeV and 399 MeV. The Run 1a results have been normalized to the new LØ cross section to be consistent with Run 1b results.

Table 8.3: Values used in the Ratio Measurement.

$\mathcal{R}$	10.43 ± 0.27	
	Value	Uncertainty Contribution
N^W_{obs}/N^Z_{obs}	12.43 ± 0.18	0.15
ϵ_Z/ϵ_W	1.108 ± 0.007	0.06
A_Z/A_W	0.787 ± 0.007	0.09
$(A^W_{Zee} + A^W_{Z\tau})/A_Z$	0.133 ± 0.034	0.03
f^W_{QCD}	0.064 ± 0.014	0.16
f^Z_{QCD}	0.045 ± 0.005	0.05
f_{DY}	0.012 ± 0.001	0.01
$A^W_{W\tau}/A_W$	0.021 ± 0.002	0.02
NLO	1.00 ± 0.01	0.10

Using $B(Z \to ee) = 0.03367 \pm 0.00006$ [81] and $\sigma_W/\sigma_Z = 3.362 \pm 0.053$ [15], we get

$$\begin{aligned} B(W \to e\nu) &= 0.1044 \pm 0.0015\ (\text{stat}) \pm 0.0020\ (\text{syst}) \\ &\pm 0.0017\ (\text{other}) \pm 0.0010\ (\text{NLO})\ , \end{aligned} \tag{8.8}$$

where the next to last source of uncertainty comes from uncertainties in $B(Z \to ee)$ and in σ_W/σ_Z. The standard model prediction is $B(W \to e\nu) = 0.1084 \pm 0.002$. Assuming the standard model prediction for the electronic partial width (0.2264 ± 0.0007 GeV [82]), we can calculate the W width $,_W = ,^e_W/B(W \to e\nu)$ as

$$,_W = 2.169 \pm 0.031\ (\text{stat}) \pm 0.042\ (\text{syst})$$

$$\pm \quad 0.041 \text{ (other)} \pm 0.022 \text{ (NLO) GeV} , \tag{8.9}$$

to be compared with the standard model prediction of , $_W$ = 2.094 ± 0.006 GeV [82]. This is the most precise measurement of the W width to date. Figure 8.3 compares our measurement with previous measurements from the Tevatron and from LEP. The difference between our measured value and the standard model prediction, which is the width for the W to decay to final states other than the two lightest quark doublets and the three lepton doublets, is 0.075 ± 0.07 GeV. This is consistent with zero within uncertainties (within 1.1 sigmas), so we set a 95% confidence level limit on the W width to non-standard-model final states ("invisible width"). Assuming the uncertainty is Gaussian, removing the unphysical region where the invisible width is negative, and integrating to 95% of the remaining area we set a 95% confidence level upper limit on the invisible partial width of the W of 0.213 GeV.

Table 8.4: Comparison of the current run 1b (1994–1995) measurement to the run 1a (1992–1993) measurement.

Data Period	$\mathcal{R}$	Correlated Uncertainty	Uncorrelated Uncertainty
1a,electron (13 pb^{-1})	10.82	0.137	0.533
1a,muon (11 pb^{-1})	11.8	0	2.110
1b,electron (84.5 pb^{-1})	10.43	0.137	0.235

We combine our run 1b (1994–1995) result with the DØ Collaboration results from run 1a (1992–1993) [6] for $\mathcal{R}$. Table 8.4 compares the two measurements. Because most of the systematic uncertainties in the run 1a measurement in the

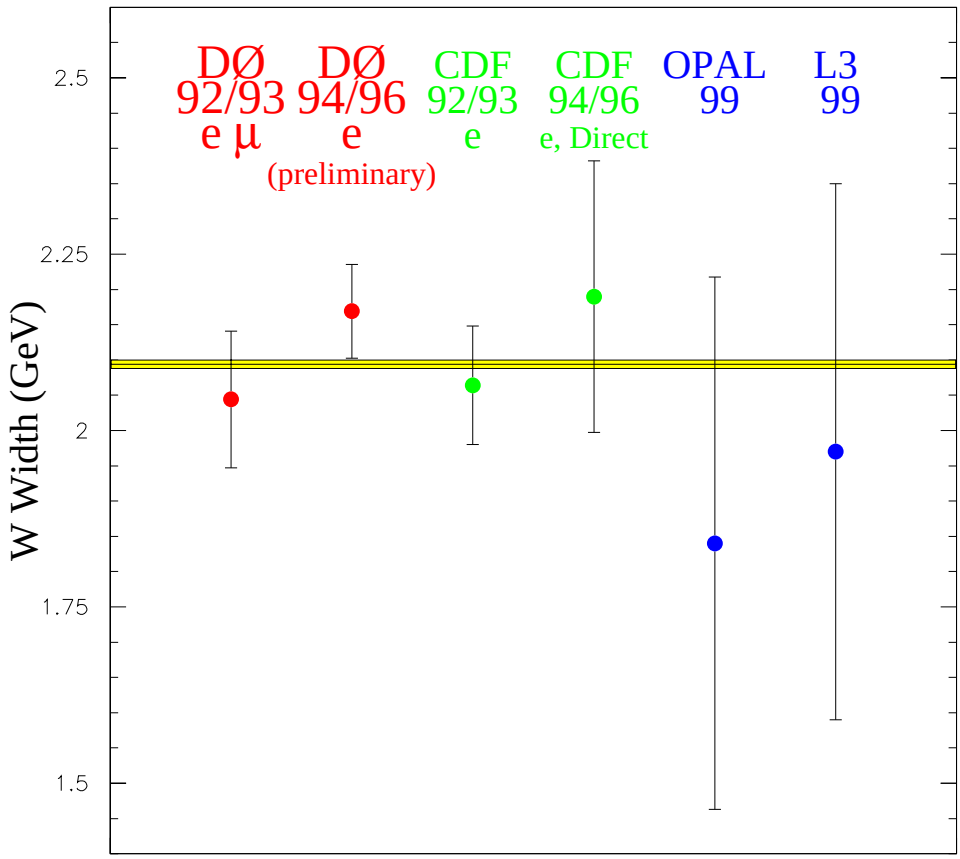

Figure 8.3: Comparison of , $_W$ measurements. The horizontal line is the standard model prediction. The OPAL and L3 results are direct measurements from kinematic fits to $qqqq$ and $qql\nu$ events from W pair decays. CDF's direct measurement uses fits to the tail of the transverse mass distribution.

electron channel were dominated by the statistics of the sample used to evaluate the uncertainty, the 1a and 1b measurements are mostly uncorrelated. Only the acceptance, the Drell-Yan correction, and the NLO uncertainties are correlated

(we have added the same 1% NLO uncertainty to the 1a result). Combining with this assumption, we get $\mathcal{R} = 10.51 \pm 0.25$, , $_W = 2.152 \pm 0.066$ GeV, and a 95% confidence level upper limit on the invisible width of 0.191 GeV. Table 8.5 summarizes our results.

Table 8.5: Results.

	1b (84.5 pb^{-1})	1a+1b combined (13 + 11 + 84.5 pb^{-1})
Ratio $\mathcal{R}$	10.43 ± 0.27	10.51 ± 0.25
$B(W \to e\nu)$	0.1044 ± 0.0032	0.105 ± 0.003
, $_W$	2.169 ± 0.070 GeV	2.152 ± 0.066 GeV
95% C.L. upper limit , $_W^{inv}$	0.213 GeV	0.191 GeV

8.3 Consistency Checks

The individual $W \to e\nu$ and $Z \to ee$ cross sections should yield the same result when measured using any particular cryostat. We calculated the cross sections using the individual calorimeter cryostats, and compared the resulting cross sections. We also checked for any dependence of our results on instantaneous luminosity.

8.3.1 Cross Sections from the Individual Cryostats

As a consistency check, we calculate the W and Z cross sections using the data from each calorimeter cryostat individually, and compare the differences between them with the uncorrelated uncertainties. The luminosity uncertainty, which is

the largest uncertainty in each individual cross section measurement, is 100% correlated between the different cryostats and therefore is not used in these comparisons. For the CC alone, the result for $\sigma(p\overline{p} \to W + X) \cdot B(W \to e\nu)$ is 2308 ± 11 (stat) ± 51 (syst) ± 99 (lum) pb. For the EC, the result is 2207 ± 16 ± 121 ± 95 pb. The dominant uncertainties in the CC are the uncertainty on the acceptance (± 21 pb), the uncertainty on the efficiency (± 31 pb), and the uncertainty from the multi-jet, b-quark, and direct photon background (± 34 pb). The dominant uncertainties in the EC are on the acceptance (± 20 pb), the efficiency (± 41 pb), and the multi-jet, b-quark, and direct photon background (± 112 pb). The uncertainties in the acceptances come from the calorimeter energy scales (mostly uncorrelated), assumptions on the distribution in boson transverse momentum (correlated), and assumptions on the effects of final state radiation (correlated). The systematic uncertainties in the efficiencies are mostly correlated. There is a statistical component that would be uncorrelated, but we neglect it here and assume the efficiencies are correlated (to be conservative). The uncertainties in QCD backgrounds are mostly uncorrelated between the CC and the EC. Using the full uncertainty in the background, (the uncertainties in acceptance and efficiency can be neglected for the purposes of this comparison) we estimate the difference between the CC and EC cross sections as 101 ± 19 ± 117 pb.

Using only CC- CC combinations, the result for $\sigma(p\overline{p} \to Z + X) \cdot B(Z \to ee)$ is 223 ± 4 ± 4 ± 10 pb. For CC- EC combinations, it is 216 ± 5 ± 4 ± 9 pb. For EC- EC combinations, it is 235 ± 10 ± 5 ± 10 pb. The dominant uncertainty in the CC-CC measurement is from the uncertainty on the lepton identification efficiency (3.5 pb). The dominant uncertainties in the CC-EC

measurement are from lepton identification (3.3 pb) and QCD background (2.3 pb). In the EC-EC measurements, lepton identification contributes 4.5 pb to the uncertainty, and QCD background contributes 2.5 pb. To estimate the errors on the difference, we assume that the efficiencies are correlated. For the CC-CC measurement, the background contribution is small. Because the CC-EC and EC-EC backgrounds both contain an EC electron candidate, we assume the background is 100% correlated. We therefore consider only the statistical uncertainty, and we get $\sigma_{CC-CC} - \sigma_{CC-EC} = 7 \pm 6$ pb, $\sigma_{CC-CC} - \sigma_{EC-EC} =$ -12 $\pm$ 11 pb, and $\sigma_{CC-EC} - \sigma_{EC-EC}=$ -19 $\pm$ 11 pb.

8.3.2 Dependence on Instantaneous Luminosity

This is the first attempt by DØ to accurately measure cross sections at relatively high instantaneous luminosities. As was mentioned in Chapter 7, the average instantaneous luminosities during Run 1b for the $W \rightarrow e\nu$ and $Z \rightarrow ee$ data samples was $\approx 7.5 \times 10^{30}$ cm^{-2}s^{-1}, resulting in an average of 1.6 of interactions per beam crossing. This implies that a large fraction of the $W \rightarrow e\nu$ and $Z \rightarrow ee$ events are accompanied by multiple interactions. To search for any dependences on luminosity, the data is divided into five subsamples according to the value of the instantaneous luminosity when each event occurred so that each subsample contained approximately one fifth of the events. The mean values of the instantaneous luminosity for each sample are 3.33, 5.40, 7.24, 9.43, and 13.29 $\times 10^{30}$ cm^{-2}s^{-1}. For each subsample, the electron identification efficiencies, the integrated luminosity, and the backgrounds from multi-jet, b quarks, and direct photons were re-calculated. The electron identification efficiency for W events for the highest luminosity bin is 17% lower than that for the lowest luminosity bin,

and the multi-jet background is 2% larger. Figures 8.4 and 8.5 show the W and Z cross section, respectively, as a function of luminosity. Figure 8.6 shows the ratio of cross sections in the five bins of instantaneous luminosity. The observed cross sections and their ratio do not appear to depend on instantaneous luminosity: the data is statistically consistent with no luminosity dependence.

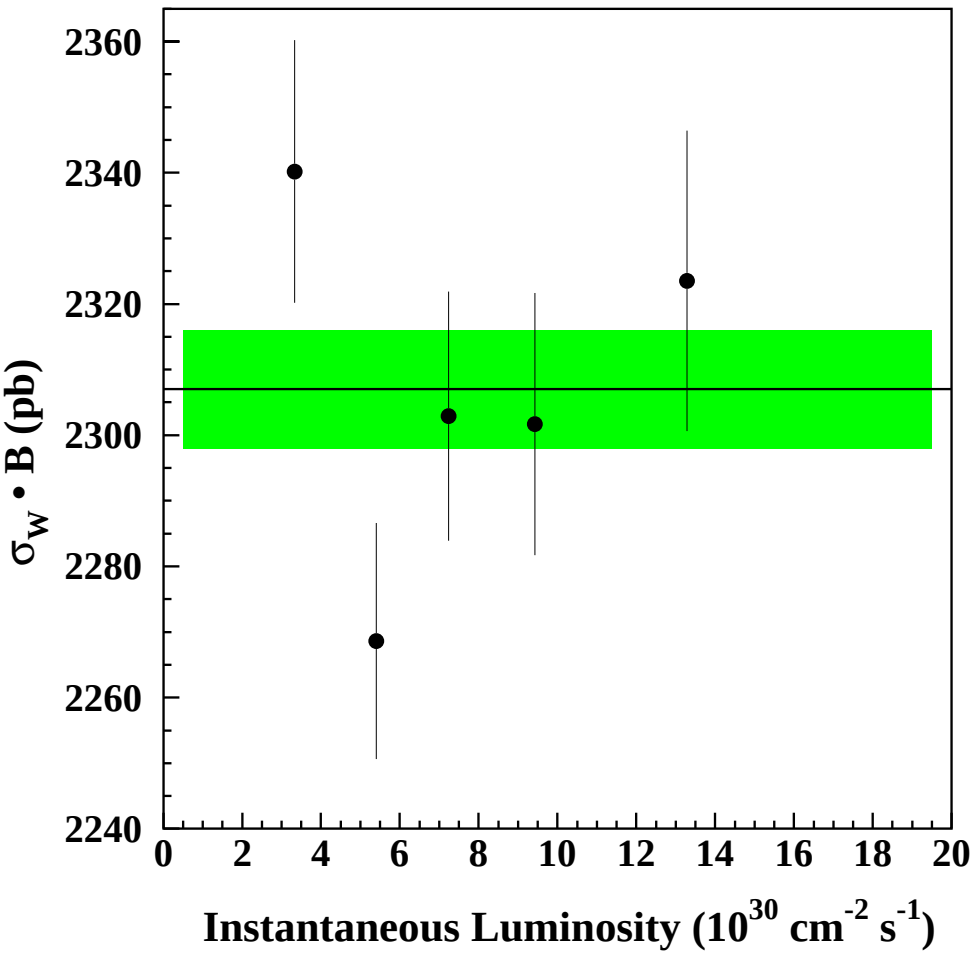

Figure 8.4: The $W \to e\nu$ cross section versus instantaneous luminosity. The error bars are statistical only. The solid line is the result from summing over all instantaneous luminosities, and the shaded band is the corresponding statistical uncertainty.

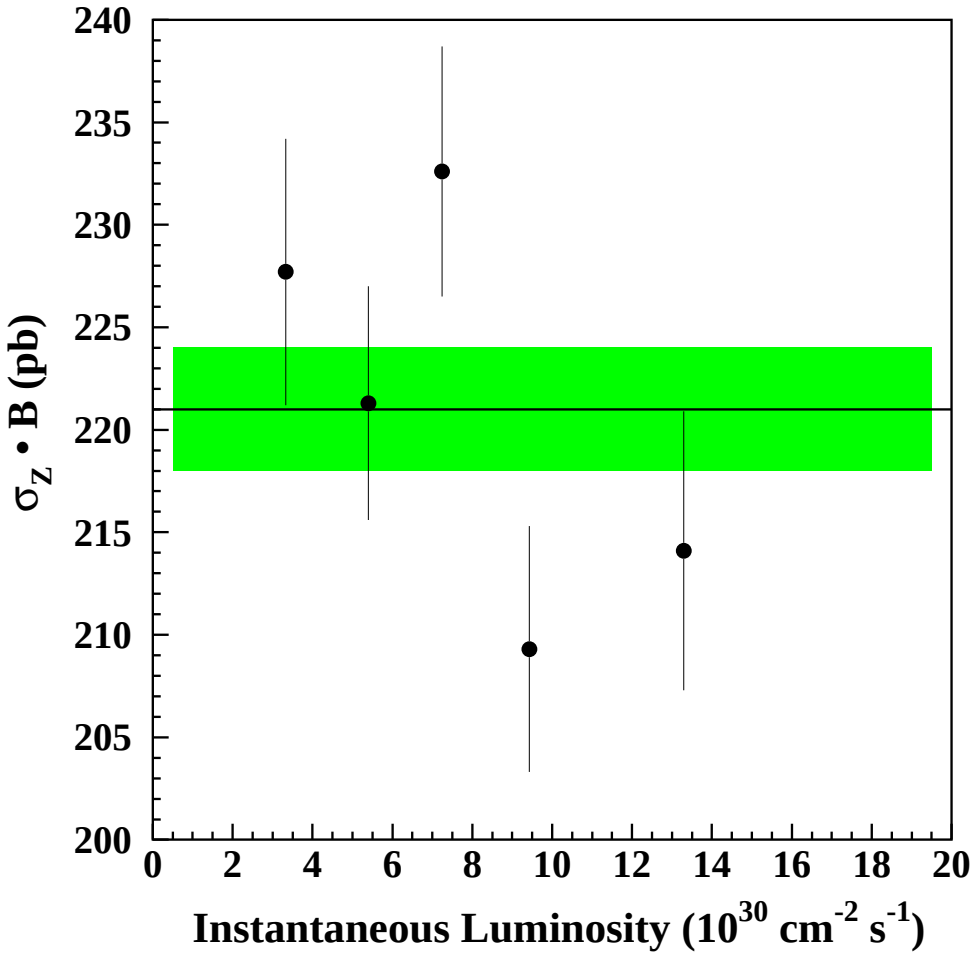

Figure 8.5: The $Z \to ee$ cross section versus instantaneous luminosity. The error bars are statistical only. The solid line is the result from summing over all instantaneous luminosities, and the shaded band is the corresponding statistical uncertainty.

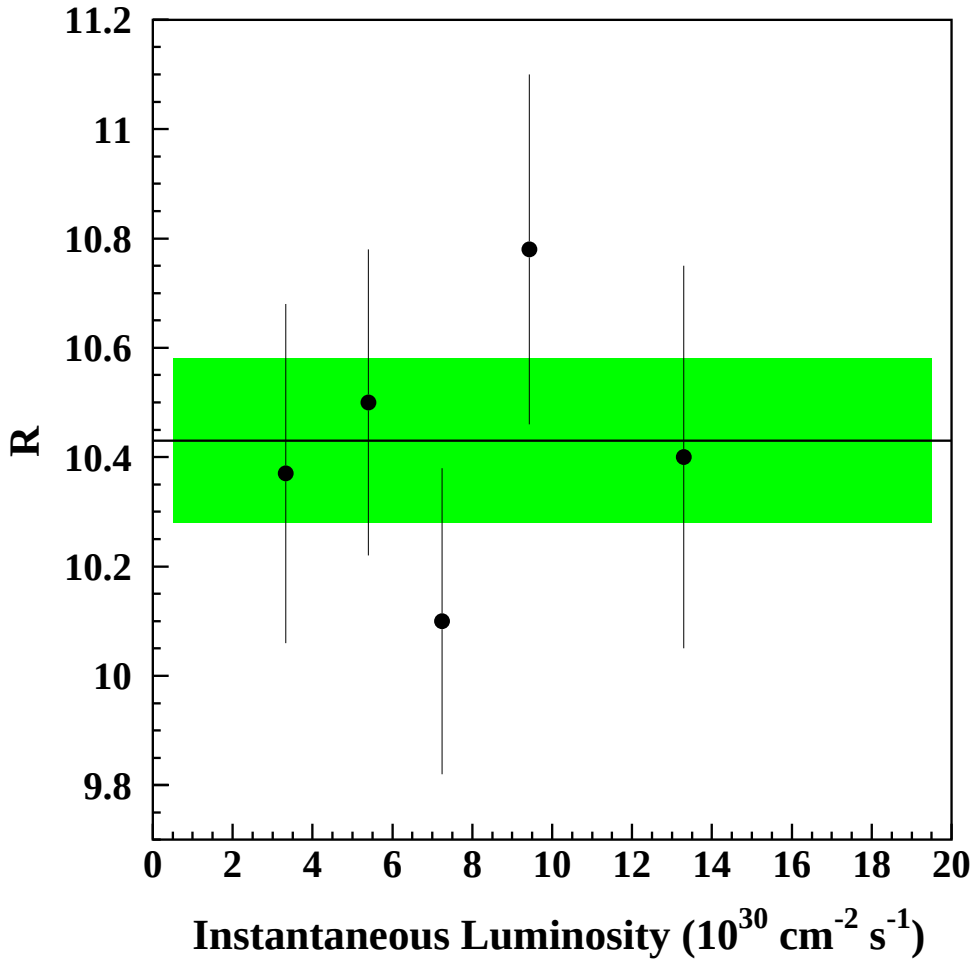

Figure 8.6: The ratio $\sigma(p\overline{p} \to W + X) \cdot B(W \to e\nu)/\sigma(p\overline{p} \to Z + X) \cdot B(Z \to ee)$ versus instantaneous luminosity. The error bars are statistical only. The solid line is the result from summing over all instantaneous luminosities, and the shaded band is the corresponding statistical uncertainty.

Chapter 9

Conclusions and Future Prospects

Using 84.5 pb^{-1} of data collected at DØ during Run 1b, we have measured the W and Z production cross section times electronic branching fractions. From 67078 $W \to e\nu$ candidate events and 5397 $Z \to ee$ candidate events we determined

$$\sigma(p\overline{p} \to W + X) \cdot B(W \to e\nu) = 2310 \ \pm 110 \text{ pb} \tag{9.1}$$

$$\sigma(p\overline{p} \to Z + X) \cdot B(Z \to ee) = 221 \ \pm 11 \text{ pb} \tag{9.2}$$

where the errors are dominated by a 4.3% uncertainty in the integrated luminosity. These are in agreement with standard model theoretical predictions (see Figure 8.2 and caption):

$$\sigma(p\overline{p} \to W + X) \cdot B(W \to e\nu) = 2519 \pm 115\text{pb} \tag{9.3}$$

$$\sigma(p\overline{p} \to Z + X) \cdot B(Z \to ee) = 235 \pm 10\text{pb} \tag{9.4}$$

We have determined the ratio of the cross sections to be

$$\mathcal{R} = 10.43 \ \pm 0.27 \tag{9.5}$$

From the measured value of $\mathcal{R}$ we have indirectly determined the total width of the W boson and the W branching fraction to first generation leptons:

$$, _W = 2.169 \ \pm 0.070 \text{ GeV} \tag{9.6}$$

$$B(W \to e\nu) \ = 0.1044 \ \pm 0.0032 \tag{9.7}$$

This is the most precise measurement of , $_W$ to date, with an uncertainty roughly equal to that of all previous measurements combined. The W width and branching fraction are in good agreement with standard model predictions:

$$, _W = 2.094 \pm 0.006 \text{GeV} \tag{9.8}$$

$$B(W \to e\nu) \ = 0.108 \pm 0.002 \tag{9.9}$$

From the measured and predicted values of , $_W$ we calculate a 95% C.L. upper limit on the width of the W decaying to non-standard model final states:

$$, _W^{inv} < 0.213 \text{ GeV} \tag{9.10}$$

In the near future, the DØ measurement can be combined with the ongoing CDF measurement in order to reduce the uncertainty in , $_W$. The Tevatron, as well as the different experiments at Fermilab, are now preparing for Run 2, which will start near the end of 2000 and will have an integrated luminosity of roughly 2 fb^{-1}, or 2000 pb^{-1}. This will allow a more precise determination of , $_W$, since the increase in Z statistics will help reduce several of the systematic uncertainties, and clearly the statistical uncertainties will be greatly reduced as well. The largest source of systematic uncertainty in the determination of $\mathcal{R}$ and , $_W$ is the uncertainty on the QCD background fraction in the $W \to e\nu$ sample, and this is likely to be one of the dominant uncertainties in Run 2 as well. Theoretical uncertainties arising from NLO electroweak corrections to the cross sections are expected to be reduced significantly within the next year or two, and work is being done to try to reduce the uncertainties which arise from the parton distribution functions.

The fact that the cross section measurements exhibit no luminosity dependence gives this analysis a potentially useful application. Since the systematic, statistical and theoretical uncertainties are smaller than the luminosity uncertainty, one could consider for Run 2 normalizing the luminosity measurement to the W cross section (since the W will have higher statistics than the Z). This would amount to measuring all cross sections in units of $\sigma(W \to e\nu)$, and studies of this application are already in progress.

Appendix A

Rapidity and Pseudorapidity

In general, the partons involved in any given collision will carry different fractions of the hadron momentum, and therefore the center of mass of the partons involved in the hard scatter will have a net boost along the beam direction $\hat{z}$ in the laboratory frame.

Instead of polar angle θ, it is convenient in hadron colliders to measure distributions with respect to *rapidity*, because rapidity distributions are invariant under a Lorentz boost β along $\hat{z}$. Rapidity is defined as

$$y \equiv \frac{1}{2}\ln\left(\frac{E+p_z}{E-p_z}\right) = \ln\left(\frac{E+p_z}{m_T}\right) = \tanh^{-1}(p_z/E) \tag{A.1}$$

The first equality follows directly from the definition

$$m_T^2 \equiv E^2 - p_z^2 = (E+p_z)(E-p_z) \tag{A.2}$$

To see that the second equality in eq. A.1 holds, take tanh on both sides:

$$\tanh\left[\ln\left(\frac{E+p_z}{m_T}\right)\right] = p_z/E$$

and the left hand side is

$$\frac{e^{\ln()} - e^{-\ln()}}{e^{\ln()} + e^{-\ln()}} = \frac{\frac{E+p_z}{m_T} - \frac{m_T}{E+p_z}}{\frac{E+p_z}{m_T} + \frac{m_T}{E+p_z}} = \frac{(E+p_z)^2 - m_T^2}{(E+p_z)^2 + m_T^2}$$

$$= \frac{(E+p_z)[(E+p_z)-(E-p_z)]}{(E+p_z)[(E+p_z)+(E-p_z)]} = \frac{p_z}{E} \bullet$$

Under a boost β along the $\hat{z}$ direction, $y \to y' = y - \tanh^{-1}\beta$, and therefore $dy = dy'$. Proof:

$$\begin{pmatrix} E' \\ p_z' \end{pmatrix} = \begin{pmatrix} \gamma & -\gamma\beta \\ -\gamma\beta & \gamma \end{pmatrix} \begin{pmatrix} E \\ p_z \end{pmatrix} \Rightarrow \left\{ \begin{array}{l} E' = \gamma E - \gamma\beta p_z \\ p_z' = -\gamma\beta E + \gamma p_z \end{array} \right\} \tag{A.3}$$

and therefore

$$y' \equiv \frac{1}{2}\ln\left(\frac{E'+p_z'}{E'-p_z'}\right) = \frac{1}{2}\ln\left[\frac{\gamma\,(E-\beta p_z-\beta E+p_z)}{\gamma\,(E-\beta p_z+\beta E-p_z)}\right]$$

$$= \frac{1}{2}\ln\left[\frac{(E+p_z)(1-\beta)}{(E-p_z)(1+\beta)}\right] = \frac{1}{2}\ln\left(\frac{E+p_z}{E-p_z}\right) + \frac{1}{2}\ln\left(\frac{1-\beta}{1+\beta}\right)$$

$$= y - \frac{1}{2}\ln\left(\frac{1+\beta}{1-\beta}\right) = y - \tanh^{-1}\beta \bullet$$

where the last equality follows from eq. A.1 with the substitutions $E \to 1$ and $p_z \to \beta$. It follows that any rapidity distribution is invariant under such a boost: $dN/dy = dN/dy'$.

For $p^2 \gg m^2$, as is usually the case in high $\sqrt{s}$ collisions,

$$E^2 = p^2 \Rightarrow p_z = p\cos\theta = E\cos\theta \tag{A.4}$$

so it follows that

$$y = \frac{1}{2}\ln\left[\frac{E(1+\cos\theta)}{E(1-\cos\theta)}\right] = -\frac{1}{2}\ln\left(\frac{1-\cos\theta}{1+\cos\theta}\right) = -\frac{1}{2}\ln\left[\frac{1-\cos^2\theta}{(1+\cos\theta)^2}\right]$$

$$= -\ln\left(\frac{\sin\theta}{1+\cos\theta}\right) = -\ln\left[\tan\left(\frac{\theta}{2}\right)\right]$$

where the last equality follows straight forward from the substitution $\theta = 2x$:

$$\frac{\sin 2x}{1+\cos 2x} = \frac{2\sin x\cos x}{1+\cos^2 x - \sin^2 x} = \frac{2\sin x\cos x}{2\cos^2 x} = \tan x$$

Pseudorapidity η is defined as

$$\eta \equiv -\ln\left[\tan\left(\frac{\theta}{2}\right)\right] \tag{A.5}$$

and in the limit where the particle energy is much larger than its rest mass, it is equal to the rapidity, which is invariant under boosts in the beam direction.

Appendix B

Cancelation of Tracking Efficiency Correlations in $\mathcal{R}$

As discussed in Chapter 5, the W tracking efficiency assuming there are no correlations is given by

$$\epsilon_W^{trk} = \frac{2pp}{2pp + pf} \ , \tag{B.1}$$

where pp is the number of events in the $Z \to ee$ diagnostic sample in which both electrons pass the tracking requirement, and pf is the number of events in which only one electron passes the tracking requirement. This is simply the efficiency for the electron to pass the tracking cut, as required in the $W \to e\nu$ selection. If one takes the tracking efficiency correlations into account, the efficiency is given by the number of electrons which pass the tracking cut divided by the total number of diagnosis electrons:

$$\epsilon_W^{trk} = \frac{2pp + pf}{2(pp + pf + ff)} \ . \tag{B.2}$$

Define:

$$\epsilon \equiv \frac{2pp}{2pp + pf}$$
$$N \equiv pp + pf + ff$$

The ratio of "correlated" to "non-correlated" tracking efficiencies for W is then:

$$R^W = \frac{(2pp + pf)/2(pp + pf + ff)}{2pp/(2pp + pf)} = \frac{1}{\epsilon}\frac{1}{N}\frac{2pp + pf}{2} \tag{B.3}$$

For the Z, if one assumes there are no correlations, the tracking efficiency is given by

$$\epsilon_Z^{trk} = \epsilon^2 + 2\epsilon(1 - \epsilon) \ , \tag{B.4}$$

with ϵ as defined above. This is simply the efficiency for at least one of the electrons to pass the tracking cut, as required in the $Z \to ee$ selection. If correlations exist, the efficiency is given by the number of $Z \to ee$ events passing the tracking requirement divided by the total number of diagnostic events:

$$\epsilon_Z^{trk} = \frac{pp + pf}{pp + pf + ff} \ . \tag{B.5}$$

The ratio of "correlated" to "non-correlated" tracking efficiencies for Z is then:

$$R^Z = \frac{(pp + pf)/(pp + pf + ff)}{\epsilon^2 + 2\epsilon(1 - \epsilon)} = \frac{1}{\epsilon}\frac{1}{N}\frac{pp + pf}{2 - \epsilon} \ . \tag{B.6}$$

In order to show that $R^Z = R^W$, we just need to show that $\frac{2pp+pf}{2} = \frac{pp+pf}{2-\epsilon}$:

$$\frac{pp + pf}{2 - \epsilon} = \frac{pp + pf}{2 - \frac{2pp}{2pp+pf}} = \frac{pp + pf}{\frac{2(2pp+pf)-2pp}{2pp+pf}} = \frac{(pp + pf)(2pp + pf)}{2(pp + pf)} = \frac{2pp + pf}{2} \bullet \tag{B.7}$$

Appendix C

DØ Author List

B. Abbott,[45] M. Abolins,[42] V. Abramov,[18] B.S. Acharya,[11] I. Adam,[44] D.L. Adams,[54] M. Adams,[28] S. Ahn,[27] V. Akimov,[16] G.A. Alves,[2] N. Amos,[41] E.W. Anderson,[34] M.M. Baarmand,[47] V.V. Babintsev,[18] L. Babukhadia,[20] A. Baden,[38] B. Baldin,[27] S. Banerjee,[11] J. Bantly,[51] E. Barberis,[21] P. Baringer,[35] J.F. Bartlett,[27] A. Belyaev,[17] S.B. Beri,[9] I. Bertram,[19] V.A. Bezzubov,[18] P.C. Bhat,[27] V. Bhatnagar,[9] M. Bhattacharjee,[47] G. Blazey,[29] S. Blessing,[25] P. Bloom,[22] A. Boehnlein,[27] N.I. Bojko,[18] F. Borcherding,[27] C. Boswell,[24] A. Brandt,[27] R. Breedon,[22] G. Briskin,[51] R. Brock,[42] A. Bross,[27] D. Buchholz,[30] V.S. Burtovoi,[18] J.M. Butler,[39] W. Carvalho,[2] D. Casey,[42] Z. Casilum,[47] H. Castilla-Valdez,[14] D. Chakraborty,[47] S.V. Chekulaev,[18] W. Chen,[47] S. Choi,[13] S. Chopra,[25] B.C. Choudhary,[24] J.H. Christenson,[27] M. Chung,[28] D. Claes,[43] A.R. Clark,[21] W.G. Cobau,[38] J. Cochran,[24] L. Coney,[32] W.E. Cooper,[27] D. Coppage,[35] C. Cretsinger,[46] D. Cullen-Vidal,[51] M.A.C. Cummings,[29] D. Cutts,[51] O.I. Dahl,[21] K. Davis,[20] K. De,[52] K. Del Signore,[41] M. Demarteau,[27] D. Denisov,[27] S.P. Denisov,[18] H.T. Diehl,[27] M. Diesburg,[27] G. Di Loreto,[42] P. Draper,[52] Y. Ducros,[8] L.V. Dudko,[17] S.R. Dugad,[11] A. Dyshkant,[18] D. Edmunds,[42] J. Ellison,[24] V.D. Elvira,[47] R. Engelmann,[47] S. Eno,[38] G. Eppley,[54] P. Ermolov,[17] O.V. Eroshin,[18] H. Evans,[44] V.N. Evdokimov,[18]

T. Fahland,[23] M.K. Fatyga,[46] S. Feher,[27] D. Fein,[20] T. Ferbel,[46] H.E. Fisk,[27] Y. Fisyak,[48] E. Flattum,[27] G.E. Forden,[20] M. Fortner,[29] K.C. Frame,[42] S. Fuess,[27] E. Gallas,[27] A.N. Galyaev,[18] P. Gartung,[24] V. Gavrilov,[16] T.L. Geld,[42] R.J. Genik II,[42] K. Genser,[27] C.E. Gerber,[27] Y. Gershtein,[51] B. Gibbard,[48] B. Gobbi,[30] B. Gómez,[5] G. Gómez,[38] P.I. Goncharov,[18] J.L. González Solís,[14] H. Gordon,[48] L.T. Goss,[53] K. Gounder,[24] A. Goussiou,[47] N. Graf,[48] P.D. Grannis,[47] D.R. Green,[27] J.A. Green,[34] H. Greenlee,[27] S. Grinstein,[1] P. Grudberg,[21] S. Grünendahl,[27] G. Guglielmo,[50] J.A. Guida,[20] J.M. Guida,[51] A. Gupta,[11] S.N. Gurzhiev,[18] G. Gutierrez,[27] P. Gutierrez,[50] N.J. Hadley,[38] H. Haggerty,[27] S. Hagopian,[25] V. Hagopian,[25] K.S. Hahn,[46] R.E. Hall,[23] P. Hanlet,[40] S. Hansen,[27] J.M. Hauptman,[34] C. Hays,[44] C. Hebert,[35] D. Hedin,[29] A.P. Heinson,[24] U. Heintz,[39] R. Hernández-Montoya,[14] T. Heuring,[25] R. Hirosky,[28] J.D. Hobbs,[47] B. Hoeneisen,[6] J.S. Hoftun,[51] F. Hsieh,[41] Tong Hu,[31] A.S. Ito,[27] S.A. Jerger,[42] R. Jesik,[31] T. Joffe-Minor,[30] K. Johns,[20] M. Johnson,[27] A. Jonckheere,[27] M. Jones,[26] H. Jöstlein,[27] S.Y. Jun,[30] C.K. Jung,[47] S. Kahn,[48] D. Karmanov,[17] D. Karmgard,[25] R. Kehoe,[32] S.K. Kim,[13] B. Klima,[27] C. Klopfenstein,[22] B. Knuteson,[21] W. Ko,[22] J.M. Kohli,[9] D. Koltick,[33] A.V. Kostritskiy,[18] J. Kotcher,[48] A.V. Kotwal,[44] A.V. Kozelov,[18] E.A. Kozlovsky,[18] J. Krane,[34] M.R. Krishnaswamy,[11] S. Krzywdzinski,[27] M. Kubantsev,[36] S. Kuleshov,[16] Y. Kulik,[47] S. Kunori,[38] F. Landry,[42] G. Landsberg,[51] A. Leflat,[17] J. Li,[52] Q.Z. Li,[27] J.G.R. Lima,[3] D. Lincoln,[27] S.L. Linn,[25] J. Linnemann,[42] R. Lipton,[27] A. Lucotte,[47] L. Lueking,[27] A.K.A. Maciel,[29] R.J. Madaras,[21] R. Madden,[25] L. Magaña-Mendoza,[14] V. Manankov,[17] S. Mani,[22] H.S. Mao,[4] R. Markeloff,[29] T. Marshall,[31] M.I. Martin,[27] R.D. Martin,[28] K.M. Mauritz,[34] B. May,[30] A.A. Mayorov,[18] R. McCarthy,[47] J. McDonald,[25] T. McKibben,[28] J. McKinley,[42] T. McMahon,[49] H.L. Melanson,[27] M. Merkin,[17] K.W. Merritt,[27] C. Miao,[51] H. Miettinen,[54] A. Mincer,[45] C.S. Mishra,[27] N. Mokhov,[27] N.K. Mondal,[11] H.E. Montgomery,[27] M. Mostafa,[1]

H. da Motta,[2] C. Murphy,[28] F. Nang,[20] M. Narain,[39] V.S. Narasimham,[11] A. Narayanan,[20] H.A. Neal,[41] J.P. Negret,[5] P. Nemethy,[45] D. Norman,[53] L. Oesch,[41] V. Oguri,[3] N. Oshima,[27] D. Owen,[42] P. Padley,[54] A. Para,[27] N. Parashar,[40] Y.M. Park,[12] R. Partridge,[51] N. Parua,[7] M. Paterno,[46] B. Pawlik,[15] J. Perkins,[52] M. Peters,[26] R. Piegaia,[1] H. Piekarz,[25] Y. Pischalnikov,[33] B.G. Pope,[42] H.B. Prosper,[25] S. Protopopescu,[48] J. Qian,[41] P.Z. Quintas,[27] R. Raja,[27] S. Rajagopalan,[48] O. Ramirez,[28] N.W. Reay,[36] S. Reucroft,[40] M. Rijssenbeek,[47] T. Rockwell,[42] M. Roco,[27] P. Rubinov,[30] R. Ruchti,[32] J. Rutherfoord,[20] A. Sánchez-Hernández,[14] A. Santoro,[2] L. Sawyer,[37] R.D. Schamberger,[47] H. Schellman,[30] J. Sculli,[45] E. Shabalina,[17] C. Shaffer,[25] H.C. Shankar,[11] R.K. Shivpuri,[10] D. Shpakov,[47] M. Shupe,[20] R.A. Sidwell,[36] H. Singh,[24] J.B. Singh,[9] V. Sirotenko,[29] E. Smith,[50] R.P. Smith,[27] R. Snihur,[30] G.R. Snow,[43] J. Snow,[49] S. Snyder,[48] J. Solomon,[28] M. Sosebee,[52] N. Sotnikova,[17] M. Souza,[2] N.R. Stanton,[36] G. Steinbrück,[50] R.W. Stephens,[52] M.L. Stevenson,[21] F. Stichelbaut,[48] D. Stoker,[23] V. Stolin,[16] D.A. Stoyanova,[18] M. Strauss,[50] K. Streets,[45] M. Strovink,[21] A. Sznajder,[2] P. Tamburello,[38] J. Tarazi,[23] M. Tartaglia,[27] T.L.T. Thomas,[30] J. Thompson,[38] D. Toback,[38] T.G. Trippe,[21] P.M. Tuts,[44] V. Vaniev,[18] N. Varelas,[28] E.W. Varnes,[21] A.A. Volkov,[18] A.P. Vorobiev,[18] H.D. Wahl,[25] J. Warchol,[32] G. Watts,[51] M. Wayne,[32] H. Weerts,[42] A. White,[52] J.T. White,[53] J.A. Wightman,[34] S. Willis,[29] S.J. Wimpenny,[24] J.V.D. Wirjawan,[53] J. Womersley,[27] D.R. Wood,[40] R. Yamada,[27] P. Yamin,[48] T. Yasuda,[27] P. Yepes,[54] K. Yip,[27] C. Yoshikawa,[26] S. Youssef,[25] J. Yu,[27] Y. Yu,[13] Z. Zhou,[34] Z.H. Zhu,[46] M. Zielinski,[46] D. Zieminska,[31] A. Zieminski,[31] V. Zutshi,[46] E.G. Zverev,[17] and A. Zylberstejn[8]

(DØ Collaboration)

[1]Universidad de Buenos Aires, Buenos Aires, Argentina

[2]LAFEX, Centro Brasileiro de Pesquisas Físicas, Rio de Janeiro, Brazil

[3]Universidade do Estado do Rio de Janeiro, Rio de Janeiro, Brazil

[4]Institute of High Energy Physics, Beijing, People's Republic of China

[5]Universidad de los Andes, Bogotá, Colombia

[6]Universidad San Francisco de Quito, Quito, Ecuador

[7]Institut des Sciences Nucléaires, IN2P3-CNRS, Universite de Grenoble 1, Grenoble, France

[8]DAPNIA/Service de Physique des Particules, CEA, Saclay, France

[9]Panjab University, Chandigarh, India

[10]Delhi University, Delhi, India

[11]Tata Institute of Fundamental Research, Mumbai, India

[12]Kyungsung University, Pusan, Korea

[13]Seoul National University, Seoul, Korea

[14]CINVESTAV, Mexico City, Mexico

[15]Institute of Nuclear Physics, Kraków, Poland

[16]Institute for Theoretical and Experimental Physics, Moscow, Russia

[17]Moscow State University, Moscow, Russia

[18]Institute for High Energy Physics, Protvino, Russia

[19]Lancaster University, Lancaster, United Kingdom

[20]University of Arizona, Tucson, Arizona 85721

[21]Lawrence Berkeley National Laboratory and University of California, Berkeley, California 94720

[22]University of California, Davis, California 95616

[23]University of California, Irvine, California 92697

[24]University of California, Riverside, California 92521

[25]Florida State University, Tallahassee, Florida 32306

[26]University of Hawaii, Honolulu, Hawaii 96822

[27]Fermi National Accelerator Laboratory, Batavia, Illinois 60510

[28]University of Illinois at Chicago, Chicago, Illinois 60607

[29]Northern Illinois University, DeKalb, Illinois 60115

[30]Northwestern University, Evanston, Illinois 60208

[31]Indiana University, Bloomington, Indiana 47405

[32]University of Notre Dame, Notre Dame, Indiana 46556

[33]Purdue University, West Lafayette, Indiana 47907

[34]Iowa State University, Ames, Iowa 50011

[35]University of Kansas, Lawrence, Kansas 66045

[36]Kansas State University, Manhattan, Kansas 66506

[37]Louisiana Tech University, Ruston, Louisiana 71272

[38]University of Maryland, College Park, Maryland 20742

[39]Boston University, Boston, Massachusetts 02215

[40]Northeastern University, Boston, Massachusetts 02115

[41]University of Michigan, Ann Arbor, Michigan 48109

[42]Michigan State University, East Lansing, Michigan 48824

[43]University of Nebraska, Lincoln, Nebraska 68588

[44]Columbia University, New York, New York 10027

[45]New York University, New York, New York 10003

[46]University of Rochester, Rochester, New York 14627

[47]State University of New York, Stony Brook, New York 11794

[48]Brookhaven National Laboratory, Upton, New York 11973

[49]Langston University, Langston, Oklahoma 73050

[50]University of Oklahoma, Norman, Oklahoma 73019

[51]Brown University, Providence, Rhode Island 02912

[52]University of Texas, Arlington, Texas 76019

[53]Texas A&M University, College Station, Texas 77843

[54]Rice University, Houston, Texas 77005

Bibliography

[1] G. Arnison *et al.* (UA1 Collaboration), Phys. Lett. B **122**, 103 (1983); M. Banner *et al.* (UA2 Collaboration), Phys. Lett. B **122**, 476 (1983); P. Bagnaia *et al.* (UA2 Collaboration), Phys. Lett. B **129**, 130 (1983); G. Arnison *et al.* (UA1 Collaboration), Phys. Lett. B **129**, 273 (1983).

[2] S. Abachi *et al.* (DØ Collaboration), Phys. Rev. Lett. **75**, 1023 (1995); S. Abachi *et al.* (DØ Collaboration), Phys. Rev. Lett. **77**, 3303 (1996); S. Abachi *et al.* (DØ Collaboration), Phys. Rev. Lett. **77**, 3309 (1996); S. Abachi *et al.* (DØ Collaboration), Phys. Rev. Lett. **78**, 3634 (1997); B. Abbott *et al.* (DØ Collaboration), Phys. Rev. Lett. **79**, 1441 (1997); B. Abbott *et al.* (DØ Collaboration), Phys. Rev. Lett. **80**, 5498 (1998); F. Abe *et al.* (CDF Collaboration), Phys. Rev. Lett. **75** 11 (1995); F. Abe *et al.* (CDF Collaboration), Phys. Rev. Lett. **75** 1017 (1995); F. Abe *et al.* (CDF Collaboration), Phys. Rev. Lett. **74** 850 (1995); F. Abe *et al.* (CDF Collaboration), Phys. Rev. Lett. **74** 341 (1995); F. Abe *et al.* (CDF Collaboration), Phys. Rev. Lett. **74** 1936 (1995); P. Abreu *et al.* (DELPHI Collaboration), Phys. Lett. **B416**, 233 (1998); R. Barate *et al.* (ALEPH Collaboration), Phys. Lett. B **415**, 435 (1997); M. Acciarri *et al.* (L3 Collaboration), Phys. Lett. B **407** 419 (1997); R. Barate *et al.*

(ALEPH Collaboration), Phys. Lett. B **401**, 347 (1997); M. Acciarri *et al.* (L3 Collaboration), Phys. Lett. B **398**, 223 (1997); P. Abreu *et al.* (DELPHI Collaboration), Phys. Lett. B **397**, 158 (1997).

[3] C. Albajar *et al.* (UA1 Collaboration), Phys. Lett. B **253**, 503 (1991).

[4] J. Alitti *et al.* (UA2 Collaboration), Phys. Lett. B **276**, 365 (1992).

[5] F. Abe *et al.* (CDF Collaboration), Phys. Rev. D **52**, 2624 (1995).

[6] S. Abachi *et al.* (DØ Collaboration), Phys. Rev. Lett. **75**, 1034 (1995); B. Abbott *et al.* (DØ Collaboration), submitted to Phys. Rev. **D**, hep-ex/9901040.

[7] K. Ackerstaff *et al.* (OPAL Collaboration), Eur. Phys. J. **C2**, 395 (1998); M. Acciarri *et al.* (L3 Collaboration), Phys. Lett. B **413**, 176 (1997).

[8] J. Kalinowski and P.M. Zerwas, Phys. Lett. B **400**, 112 (1997).

[9] G. Kane, "Modern Elementary Particle Physics: the fundamental particles and forces?," Addison Wesley, 1993.

[10] V.D. Barger and R.J.N. Phillips, "Collider Physics" Addison Wesley, 1993.

[11] P.B. Arnold and M.H. Reno, Nucl. Phys. **B319**, 37 (1989).
Erratum, Nucl. Phys. **B330**, 284 (1990).

[12] G.A. Ladinsky and C.-P. Yuan, Phys. Rev. D **50**, 4239 (1994).

[13] J. Collins, D. Sopper, and G. Sterman, Nucl. Phys. **B250**, 199 (1985).

[14] I.M. Adam, Ph.D. thesis, Columbia University, 1997 (unpublished), `http://www-d0.fnal.gov/results/publications_talks/thesis/adam/ian_thesis_all.ps`.

[15] R. Hamberg, W.L. van Neerven and T. Matsuura, Nucl. Phys. **B359**, 343 (1991); W.L. van Neerven and E.B. Zijlstra, Nucl. Phys. **B382**, 11 (1992).

[16] P. Abreu *et al.* (DELPHI Collaboration), Nucl. Phys. **B418**, 403 (1994); M. Acciarri *et al.* (L3 Collaboration), Z. Phys. **C62**, 551 (1994); R. Akers *et al.* (OPAL Collaboration), Z. Phys. **C61**, 19 (1994); D. Buskulic *et al.* (ALEPH Collaboration), Z. Phys. **C62**, 539 (1994).

[17] F. Abe *et al.* (CDF Collaboration), Phys. Rev. Lett. **74**, 341 (1995).

[18] W.J. Thompson, "Introduction to Colliding Beams at Fermilab," DØ internal note 2367 (1994), unpublished.

[19] S. Abachi *et al.* (DØ Collaboration), Nucl. Instrum. Methods in Phys. Res. A **338**, 185 (1994).

[20] L.M. Lederman, Scientific American **264**(3) 48 (Mar. 1991).
H.T. Edwards, Ann. Rev. Nucl.Part. Sci. **35**,605 (1985)
F.T. Cole *et al.*, "Design Report Tevatron 1 Project," FNAL Internal Note (1984), unpublished.
F.T. Cole *et al.*, "A Report of the Design of the Fermi National Laboratory Superconducting Accelerator," FNAL Internal Note (1979), unpublished.

[21] A.R. Clark *et al.*, Nucl. Instr. Meth. **A261**, 420 (1987).

[22] A.R. Clark *et al.*, Nucl. Instr. Meth. **A279**, 243 (1989).

[23] A.R. Clark *et al.*, Nucl. Instr. Meth. **A315**, 193 (1992).

[24] D. Buchholz *et al.*, Nucl. Instr. Meth. **A257**, 556 (1987).

[25] J.F. Detœuf *et al.*, Nucl. Instr. Meth. **A265**, 157 (1988).

[26] J.F. Detœuf *et al.*, Nucl. Instr. Meth. **A279**, 310 (1989).

[27] T. Behnke, *The Central Drift Chamber for the DØ Detector: Design, Construction, and Test.* Ph.D. thesis, State University of New York at Stony Broook, Stony Brook, New York, 1989 (unpublished).

[28] D. Pizzuto, *DØ Central Tracking Performance Studies.* Ph.D. thesis, State University of New York at Stony Broook, Stony Brook, New York, 1991 (unpublished).

[29] S. Rajagopalan, *The dE/dx Capabilities of the DØ Tracking System.* Ph.D. thesis, Northwestern University, Evanston, Illinois, 1992 (unpublished).

[30] J. W. Bantly, *The DØ Forward Drift Chamber Performance and Physics Capability in the 1990 FNAL Testbeam Run.* Ph.D. thesis, Northwestern University, Evanston, Illinois, 1992 (unpublished).

[31] F. Sauli, `Principles of Operation of Multiwire Proportional and Drift Chambers` in T. Ferbel, editor, *Experimental Techniques in High Energy Physics.* Addison-Wesley (1987).

[32] C. Fabjan, `Calorimetry in High-Energy Physics` in T. Ferbel, editor, *Experimental Techniques in High Energy Physics.* Addison-Wesley (1987).

[33] C. Brown *et al.*, Nucl. Instr. Meth. **A279**, 121 (1989).

[34] J. Bantly *et al.*, IEEE Trans. Nucl. Sci. **NS-41**, 1274 (1994).

[35] M. Abolins *et al.*, IEEE Trans. Nucl. Sci. **NS-36**, 384 (1989).

[36] M. Abolins *et al.*, Nucl. Instr. Meth. **A289**, 543 (1990).

[37] J. Drinkard, "The DØ Level 1.5 Calorimeter Trigger," DØ Internal Note 2274 (1994), unpublished.

[38] D. Edmunds, S. Gross, and P. Laurens for the DØ Collaboration, "A DSP Based Calorimeter Trigger for the DØ Experiment", 1994 IEEE Nuclear Science Symposium Volume 2, pp. 819-823.

[39] D. Cutts *et al.*, IEEE Trans. Nucl. Sci. **NS-36**, 738 (1989).

[40] D. Cutts *et al.*, `Operation of the DØ Data Acquisition System` in *Proceedings of the Conference on Computing in High Energy Physics*, Annecy, France (1992).

[41] J. T. Linneman *et al.*, `The DØ Software Trigger` in *Proceedings of the Conference on Computing in High Energy Physics*, Annecy, France (1992).

[42] M. Abolins *et al.* (DØ Collaboration), Nucl. Instrum. Methods in Phys. Res. A **280**, 36 (1989); S. Abachi *et al.* (DØ Collaboration), Nucl. Instrum. Methods in Phys. Res A **324**, 53 (1993); H. Aihara *et al.*(DØ Collaboration), Nucl. Instrum Methods in Phys. Res. A **325**, 393 (1993).

[43] The LEP collaborations, the LEP Electroweak Working Group and the SLD Heavy Flavour Group, CERN-PPE/96-183 (unpublished).

[44] J. Tarazi, Ph.D. thesis, University of California at Irvine, 1997 (unpublished),

http://www-d0.fnal.gov/results/publications_talks/thesis/tarazi/thesis_final_2side.ps.

[45] R. Raja *et al.*, "Reconstruction and Analysis: Trcaking Packages, Calorimeter Packages," DØ Internal Note 1006 (1990), unpublished.

[46] R. Raja, "H-matrix Analysis for top → lepton + jets," DØ Internal Note 1192 (1992), unpublished.

[47] M. Narain, `Electron Identification in the DØ Detector`, in *Proceedings of the American Physical Society Division of Particles and Fields Conference*, Fermilab, Batavia, Illinois (1992).

[48] R. Brun and F. Carminati, CERN Program Library Long Writeup W5013, 1993 (unpublished).

[49] S. Glenn, *A Search for Self Interactions of Neutral Electroweak Gauge Bosons*. Ph.D. thesis, University of California at Davis, Davis, California, 1996 (unpublished).

[50] The bad runs are eliminated using the RUN_SELECT package within the DØUSER framework (both are part of the standard DØ software library). The package looks for the bad runs in

`D0$PHYSICS_UTIL$ROOT:[GENERAL]BAD_RUN.RCP`

with the `0FE` hexadecimal mask, which selects all problem runs except those restricted to the muon system only. The RCP file is dated 13–SEP–1996.

[51] E.M. Flattum, Ph.D. thesis, Michigan State University, 1996 (unpublished),

http://www-d0.fnal.gov/results/publications_talks/thesis/flattum/eric_thesis.ps.

[52] B. Abbott *et al.* (DØ Collaboration), Phys. Rev. D **58**, 092003 (1998).

[53] T. Sjöstrand, Comput. Phys. Commun. **82**, 74 (1994).

[54] J. Botts *et al.* (CTEQ Collaboration), Phys. Lett. B **304**, 159 (1993); H.L. Lai *et al.* (CTEQ Collaboration), Phys. Rev. D **51**, 4763 (1995); H.L. Lai *et al.* (CTEQ Collaboration), Phys. Rev. D **55**, 1280 (1997).

[55] F.A. Berends and R. Kleiss, Z. Phys. **C27**, 365 (1985).

[56] M. Bhattacharjee *et al.*, *Jet Energy Resolutions*, DØ Internal Note 2887 (1996), unpublished.

[57] F. Abe *et al.* (CDF Collaboration), Phys. Rev. Lett. **75**, 11 (1995) and Phys. Rev. D **52**, 4784 (1995).

[58] A.D. Martin, W.J. Stirling, R.G. Roberts, Phys. Lett. B **306**, 145 (1993).

[59] A.D. Martin, W.J. Stirling, R.G. Roberts, Phys. Lett. B **354**, 155 (1995).

[60] M. Gluck, E. Reya, A. Vogt, Z. Phys. **C53**, 127 (1992).

[61] A.D. Martin, W.J. Stirling, R.G. Roberts, Phys. Lett. **356B**, 89 (1995).

[62] U. Baur, S. Keller, and D. Wackeroth, FERMILAB-PUB-98-164-T, hep-ph/9807417; U. Baur, S. Keller, and W.K. Sakumoto, Phys. Rev. D **57**, 199 (1998).

[63] U. Baur, private communication.

[64] G. Marchesini *et al.* , Comput. Phys. Commun. **67**, 465 (1992), release 5.7. hep-ph/9607393

[65] W. Dharmaratna, R. Raja, and C. Stewart, *The DØ Shower Library – Version 2.0*, DØ Internal Note 1730 (1993), unpublished.

[66] P. Grudberg, *Measurement of the W and Z Boson Production Cross Sections in $p\overline{p}$ Collisions at $\sqrt{s}$ = 1.8 TeV with the DØ Detector*. Ph.D. thesis, University of California at Berkeley, Berkeley, California, 1997 (unpublished).

[67] W. Carvalho and T. Taylor, *Multiple Interaction Tool Study for Run 1*, DØ Internal Note 2798 (1995), unpublished.

[68] F. Abe *et al.* (CDF Collaboration), Phys. Rev. Lett. **78**, 2698 (1997).

[69] L. Alvero *et al.*, Phys. Rev. D **59**, 74022 (1999).

[70] S. Abachi *et al.* (DØ Collaboration), Phys. Rev. D **52**, 4877 (1995).

[71] F. Paige and S.D. Protopopescue, *Supercollider Physics*, edited by D. Soper (World Scientific, Singapore, 1987), p.41; H. Baer, F. Paige, S. Protopopescue and X. Tata, in *Proceedings of the Workshop on Physics at Current Accelerators* and Brookhaven National Laboratory report No. 38304, 1986 (unpublished).

[72] F. Abe *et al.* (CDF Collaboration), Phys. Rev. D **50**, 5550 (1994).

[73] M. Albrow, A. Beretvas, P. Giromini, L. Nodulman, FERMILAB-TM-2071, 1999 (unpublished).

[74] N. Amos *et al.* (E710 Collaboration), Phys. Rev. Lett. **68**, 2433 (1992).

[75] C. Avila *et al.* (E811 Collaboration), Phys. Lett. B **445**, 419 (1999).

[76] J. Bantly *et al.*, FERMILAB-TM-1995.

[77] C. Albajar *et al.* (UA1 Collaboration), Phys. Lett. B **198**, 271 (1987).

[78] J. Alitti *et al.* (UA2 Collaboration), Phys. Lett. B **276**, 365 (1992).

[79] W.T. Giele, E.W.N. Glover and D.A. Kosower, Nucl. Phys. **B403**, 2121 (1990).

[80] B. Abbott *et al.* (DØ Collaboration), Phys. Rev. Lett. **80**, 666 (1998).

[81] L. Montanet *et al.* (Particle Data Group), Phys. Rev. D **54**, 1 (1996).

[82] J.L. Rosner, M.P. Worah and T. Takeushi, Phys. Rev. D **49**, 1363 (1994).